TRANSPIRATION AS A MECHANISM FOR MECHANICAL AND ELECTRICAL ENERGY CONVERSION

by

Ruba Talal Borno

A dissertation submitted in partial fulfillment
of the requirements for the degree of
Doctor of Philosophy
(Electrical Engineering)
in the University of Michigan
2008

Doctoral Committee:

Assistant Professor Michel M. Maharbiz, Chair
Professor Yogesh B. Gianchandani
Associate Professor Katsuo Kurabayashi
Professor Khalil Najafi

To my mother, my father and my husband.

ACKNOWLEDGEMENTS

During my graduate research, I have had the opportunity to work and interact with many talented and inspiring individuals. My interactions with these people have been the most rewarding part of my time at Michigan. Each person has had an impact on my life by helping me conduct my research, pursue my goals, and enjoy my time outside of my graduate work. I would like to first acknowledge my advisor, Professor Michel Maharbiz. Dr. Maharbiz' enthusiasm for the research in his group was contagious and has inspired me to seek out challenging, if not, impossible endeavors out of curiosity, novelty, and science.

In addition to my faculty advisor, I would like to thank the members of my dissertation committee. Professors Gianchandani, Najafi, and Kurabayashi, who provided valuable guidance with regards to my thesis topic. I also thank Dr. Wise for valuable feedback during my preliminary thesis proposal and Dr. Richard Brown for his support and guidance.

Within the Maharbiz research group, I have had the pleasure of working with many talented people. I began mentoring Joe Steinmeyer years ago, but quickly watched him develop as a strong researcher and co-author. Joe played a valuable role in getting this technology developed. I would like to especially thank Tushar Bansal and Meng-Ping Chang for their sincere friendship. Brendan Casey deserves praise for his support and accommodation during the lab move. I have also enjoyed working with the rest of the group members: Gabriel Lavella, Jaehyun Park, Mike Pinelis, Hirotaka Sato, Taesung Kim, Prashant Padmanabhan, Whijae Roh, Joay Singhal and Abdelkader Srouji. I would also like to take this opportunity to thank Intel for financial support through the Intel Doctoral Fellowship, as well as to thank NSF for financial support of the research in this dissertation.

Outside of my research group, I have had some of the most useful, interesting, and sometimes controversial discussions with my office mates Mark Richardson, Emine Cagin, Scott Wright, Christine Eun, and Bhaskar Mitra. When speaking of lively discussions, I must also include Tzeno Galchev, with whom I have spent much time working on research

and business ideas, but always enjoyed his colorful commentary, sarcasm, and at times, insight. I must also thank my other friends at Michigan, including those the NSF ERC for WIMS. The interdisciplinary nature of our research has provided for many useful problem solving discussions, but has also given us a perspective on research and technology that is far from myopic. Without many of these people, graduate school would not have been as exciting or as educational: Gayatri Perlin, Allan Evans, Jae Yoong Cho, Andy Kuo, Kim Khalsa, Kiran Pandy, Awlok Josan, Niloufar Ghafouri, Hanseup Kim, Seow Yuen Yee, Andy Gross, Angelique Johnson, Razi Haque, Amar Basu, Rob Franklin, Neil Welch, Jay Mitchell, Rishiraj Das, Kabir Udeshi, and Burcu Ucok.

Thanks go to all staff members of the LNF, who greatly facilitated processing, especially Ed Tang, Terre Briggs, Katharine Beach, Ning Gulari, Greg Allion, and Brian VanDerElzen. I would also like to thank all of the WIMS staff members and EECS administrative assistants, especially Deb Swartz, Trasa Burkhardt, Laura Jarels, and Beth Stalnaker. I would also like to thank Dr. Tim Faley and Paul Kirsch at the Ross School of Business for their support.

Apart from everyone else, I owe my deepest gratitude to my family and to my husband. My parents, Reem and Talal Borno, have always inspired me to pursue many challenges and have encouraged me through them all. Their sacrifice and perseverance instilled a great sense of duty in me to always try my best. They inspired me to become an engineer like them and taught me the that I can always figure it out. Their continuous support has been instrumental as I have pursued my goals in life, especially in my education, and to them I am most grateful. My sisters, Lana, Hala, and Farah Borno have also been a source of inspiration as strong, intelligent, and independent women. I am proud of them.

My husband, Michael McCorquodale, deserves the most recognition. His unwavering support, guidance, and encouragement has been essential in my graduate career. After my advisor, Michael has given me the most insight about my research. More importantly, however, he is a continued source of inspiration to me. His perseverance in academia and business have served as an example to me and many others, and I truly admire him. More than anything, his relentless pursuit of excellence and nothing less motivates me to push myself to the limit.

TABLE OF CONTENTS

LIST OF TABLES

LIST OF FIGURES

CHAPTER I

INTRODUCTION

As the research community seeks to find ways to extract energy from the environment, the author looks to nature for inspiration. Through evolution, nature has engineered energy scavengers out of every living organism. As a result, biomimicry, or the copying of nature, has become an excellent way to find solutions to engineering problems that evolution has already optimized. Biomimetics encompasses the "studies and imitation of nature's methods, mechanisms and processes." The work presented in this thesis focuses on the full development of two types of energy conversion devices that seek to address the needs of remote sensor networks and mobile electronics using biomimetic and bioinspired devices. Specifically, transpiration in plants is mimicked to convert energy from evaporation.

The miniaturization of technology into the micro and nanoscale, along with the rapidly increasing decentralization of sensing and computation systems has created a need for energy-scavenging technologies [1]. Devices that scavenge power or perform work by utilizing energy already present in their environment are of interest to researchers in applications where such devices could power remote sensors and actuators. Applications are found in areas where hard-wired connections are not feasible or are too expensive, and where battery maintenance and replacements are costly. Potential sources of ambient energy include, but are not limited to, vibrations [2], wind [3], thermal gradients [4], pressure [5], and light [6]. The large numbers of varied ambient stimuli available in an environment have opened a wide field of possible energy scavenging mechanisms for scientists and engineers to explore. The current state-of-the-art electrical energy scavengers have demonstrated power output levels from the nano Watt up to the milli Watt range [7] and have been driven by the development of low-power CMOS digital circuit design [8]. However, despite improvements in power handling, architecture, and sensor design; the actual availability of suffi-

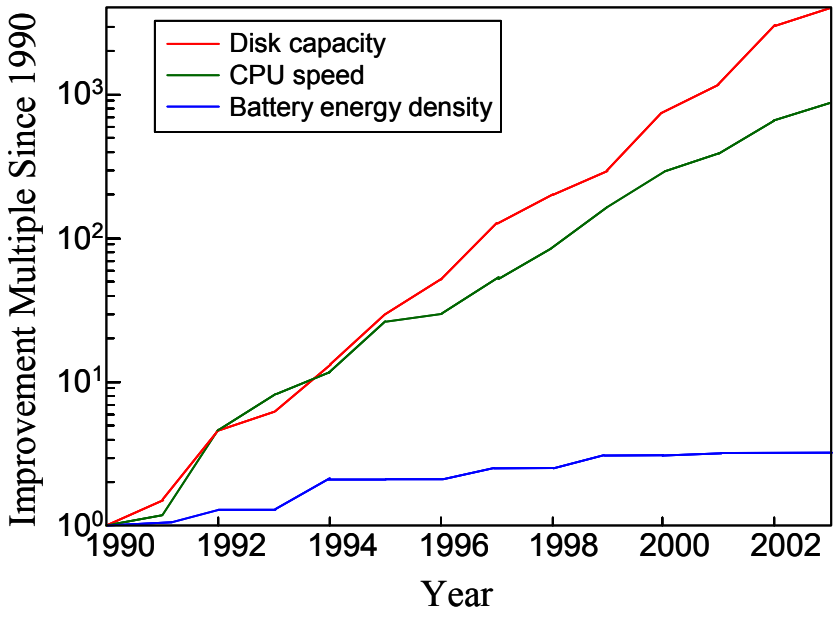

Figure 1.1 **The relative improvement in computing technology from 1990 to 2003. This plot provides a clear picture of how battery energy density has remained stagnant over the years as other computing technology has improved. Figure adapted from [6].**

cient and portable power supplies remains the most challenging technological barrier to the wide deployment of wireless sensors [9],[10]. Figure 1.1 shows the relative improvement in various computing technologies and compares them to the relative improvement in battery energy density [6]. It is obvious from this plot that as disk capacity and CPU speed have improved significantly, very little relative improvement is seen in batteries, which show meager growth rates of approximately 8% per year. This data presents one of the compelling arguments for the development of energy scavenging technologies.

1.1 Biomimicry

Nature provides innumerable examples of energy scavengers from simple unicellular organisms such as photosynthetic diatoms that scavenge energy from light to complex mammals such as humans that scavenge energy from the caloric content of food. The term biomimetics was coined in 1969 by Otto Schmitt [11],[12], and although engineering research is not yet capable of mimicking complex natural systems, biomimetics includes the use of various components of natural systems for specific applications. The research

presented here is inspired by and mimics components of transpiration in plants to scavenge mechanical energy for actuation and to generate electrical energy.

As early as 1975, the process of photosynthesis in was mimicked to convert light into electrical energy using chloroplast photoelectrochemical cells [13]. The motion of moth caterpillars was mimicked in linear actuators such as the INCHWORM® motors fabricated by Burleigh Instruments [14]. Biomimicry has a wide potential to provide commercializable products. For example, the wings of the Sternocara beetle of the Namib Desert have the potential to inspire water harvesting materials for arid climates due to their ability to collect water via the condensation of small droplets from the early-morning fog in their desert climate [15]. In fact, the water collection mechanism can be implanted in the devices presented in this thesis in order to condense water for use in actuation or power generation. The wings of the Sternocara beetle are covered with waxy hydrophobic bumps and non-waxy hydrophilic wells arranged in an alternating fashion, and can collect droplets as small as 1 - 40 μm in diameter from the desert wind. Without these microstructures, such small volumes of water could easily evaporate in the heat of the desert. Instead, water forms on the hydrophobic bumps, and is collected in the hydrophilic regions.

The hydrologic cycle, or the water cycle, describes the journey that water follows as it moves from above and below the surface of the Earth. This solar-powered cycle is continuous, and can be exploited at various phases to extract work. One of the earliest examples of using hydropower is the water wheel, which uses the runoff and water flow from the condensation and precipitation phase of the cycle. The Energy Harvest Eel (Eel) is a MEMS device that utilizes the same phase of the water cycle as the water wheel. The Eel device uses piezoelectric polymers which harvest electrical energy from water flow in rivers and oceans [16]. However, there are only a few examples [17]-[20] of researchers making micromachined devices which scavenge energy from evaporation - the other side of the water cycle. Even so, there are many environments favorable for transpiration; environments need only a humidity gradient to cause evaporation to occur. Evaporation is induced by changes in multiple parameters including temperature, relative humidity, pressure, and air flow. A change in any of those ambient conditions could be exploited by an evaporation harvesting technology. The continuous harvesting of energy would require

either a constantly replenished volume of water or a cyclical condensation and evaporation phases during operation.

Plants have evolved methods for extracting work from evaporation and the surface tension of water. Evapotranspiration is a term used to signify the combined plant and soil evaporating surfaces, where evaporation occurs at the soil-air interface, and transpiration occurs at the plant-air interface, namely leaves [21]. The cohesion-tension theory described the passive pumping of water from root to leaves via evaporation at microscale stomatal pores [21]-[24]. Trees can move water from the ground through their microvasculature networks, without metabolic pumps. Instead, plants utilize a negative pressure in the water that is contained under tension within their microvasculature networks. The ability of plants to extract work from evaporation is the inspiration behind all of the work in this thesis.

1.2 Thesis Organization

In this thesis, transpiration is researched as a mechanism for mechanical and electrical energy conversion. Two types of energy scavenging devices that were inspired by nature, and specifically by the transpiration mechanism in plants, are developed, studied, and tested. The first type of device consists of a new class of mechanical actuators that operate via the evaporation of water. The second type of device uses an evaporation driven flow to generate electrical power using a charge-pumping mechanism.

Chapter II begins with an overview of microactuation technologies that use surface tension as the driving force. Some of these technologies helped inspire as well as model the actuators developed as part of this thesis. This chapter then describes the biomimetic mechanical actuators that were developed for actuation using evaporation at room temperature. The work described in this chapter includes the design and fabrication of mechanical actuators, the mechanical and energy analysis to predict device actuation using device geometry and material properties, bottom up self-assembly using transpiration actuation, and presents a motivation to scale devices into the nano-regime and the use of this technology as a way to make “programmable materials”. Both micro and nano scale actuators were fabricated and tested. The transpiration driven actuators can be used in applications for the un-powered and controlled self-assembly of microcomponents powered only by environ-

mental humidity. The experimental work is coupled with the development of an accurate theoretical model, which has generalized applications in the study of nanomechanics and fluidics.

Chapter III presents an overview of energy harvesting technology including the state of the art. Subsequently, Chapter IV presents an overview of transpiration in plants, the mechanism, that is mimicked in the second main project of this thesis.

Chapter V presents the first system to use evaporation-driven flows of water in microchannels to convert the mechanical energy of the fluid into scalable electrical energy. The device here uses evaporation-induced flows within leaf-like microvasculature networks to drive the movement of gas bubbles through capacitor plates. This motion allows the charge pumping of an on-chip circuit, which can then be used to provide electrical power. A current measurement circuit was used to characterize the currents generated by bubble motion at various speeds. Multiple evaporators were designed and tested to enhance the rate of evaporation by maximizing the evaporative surface are to volume ratio. Further, the pressures in the system were studied and characterized, including electroosmotic pressure which is significant at the nano scale, but also has a contribution at the microscale used in this work. Lastly, a voltage output conversion circuit was designed, built and tested. Measurable voltage outputs were obtained from each water to air interface and empirical results showed good agreement with theory and simulation.

The transpiration based electrical energy conversion device developed in this thesis is differentiated from other energy scavenging devices because it utilizes the ubiquitous humidity gradient to provide energy in place of other ambient conditions currently exploited by the state of the art energy scavenging devices. This dissertation closes in Chapter VI with a summary of the thesis contributions and suggested future work based on the results presented.

CHAPTER II

TRANSPIRATION ACTUATION

This chapter presents the design, fabrication and characterization of large displacement, distributed-force polymer biomimetic actuators driven only by the surface tension of water. The devices were inspired by the hygroscopic spore dispersal mechanism in fern sporangia. The micro devices were fabricated through a single mask process using a commercial photo-patternable silicone polymer to mimic the mechanical characteristics of plant cellulose. An analytical model for predicting the microactuator behavior was developed using the principle of virtual work, and a variety of designs were simulated and compared to empirical data. Fabricated devices experienced tip deflections of more than 3.5 mm and angular rotations of more than 330^{o} due to the surface tension of water. The devices generated forces per unit length of 5.75 mN/m to 67.75 mN/m and were dependent on device geometry. This thesis also presents results which indicate that the transient water-driven deflections can be manipulated to generate devices that self-assemble into stable configurations. The developed theoretical model shows that the devices should scale well into the submicron regime. Nano-scale devices were fabricated; however, test environment limitations were encountered and are discussed in this thesis. Lastly, the actuation mechanism presented in this work may provide a robust method for embedding geometry-programmable and environment-scavenged force generation into common materials.

This chapter begins in Section 2.1 with a brief overview of microactuation technology. Section 2.2 presents information on the fern sporangium and how its actuation mechanism operates. Section 2.3 presents the device concept and operation. Section 2.4 presents the theoretical considerations and the developed analytical model to predict device behavior based on device geometry and material properties. This section also discusses the principle of virtual work and the calculation of the minimal energy to solve for equilibrium

states. Section 2.5 presents the device fabrication and Section 2.6 discusses testing process. Section 2.7 presents the empirical test results of the fabricated devices, and compares them to the analytical model; the significance of various geometric design parameters on the amount of actuation and angle of rotation are discussed. Section 2.8 presents an example of how the developed devices and transpiration actuation mechanism can be used for self-assembly applications. Section 2.9 presents an argument for scaling to the nano-regime, as well as device fabrication, experimental and analytical modeling results. Lastly, Section 2.10 presents an argument for implementing this actuation mechanism into materials.

2.1 Background on Microactuation Technology

Researchers have demonstrated an interest in the potential for extracting work from liquid surface tension for use in bottom-up self-assembly [25]-[27], batch assembly of microcomponents [28]-[31], and actuation [32],[33].

2.1.1 Surface Tension Driven Self-Assembly

The force exerted by a liquid, with a high coefficient of surface tension, on a solid surface at the liquid-solid interface can be used to physically move or deform the solid structure.

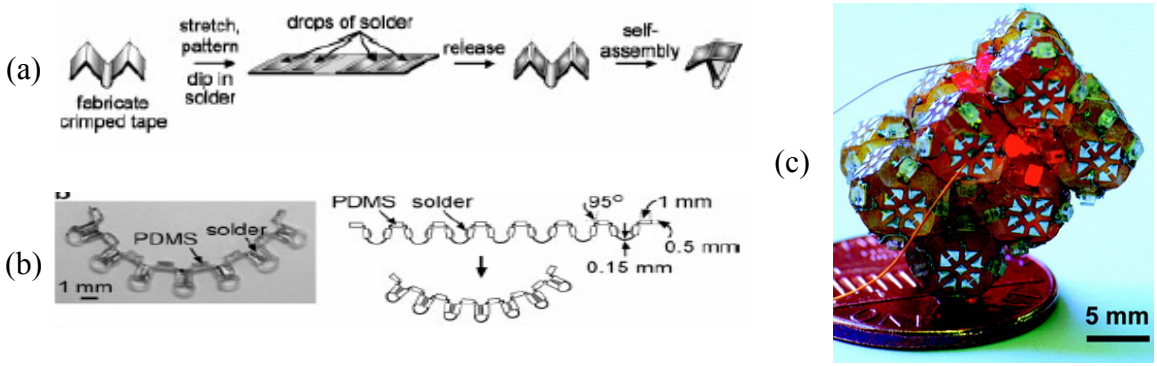

Figure 2.1 **The use of liquid solder to form self-assembled structures. (a) Illustration of fabrication process of PDMS-solder structures. (b) Photograph of quasi-3d structure. Figures (a) and (b) are from [34] (Figure 1 and Figure 3b). A photograph of the self-assembled electrical network in a three-dimensional structure containing six LEDs. Figure (c) is from [35] (Figure 3).**

Previously, the surface tension of liquid solder was used to assemble large devices for electrical networks and three-dimensional elastomer structures [34],[35]. In that work, metal solder pads were first patterned and then melted to rotate adjacent structures using the surface tension of the molten solder to create complex structures Figure 2.1. The same principle was utilized to establish electrical connections to light emitting diodes (LEDs) using the solder as the conductive material Figure 2.3(c).

2.1.2 Surface Tension Driven Actuation

In addition to the self-assembly described above, surface-tension has also been explored as a possible method to drive low-friction actuation [32]. In that work, a bistable liquid-solid micromechanical contact switch was made from a 5 - 20 μm diameter droplet that maintained its structural stability due to the surface tension of the liquid.

In addition to the use of liquid metals for actuation, the surface tension of water has been exploited to study the mechanical strength of lithographic polymers [36]. In that work, photo-defined test structures consisting of narrow, parallel beams were developed and released in water. As the channels between the test structures dried, water tension caused stiction in some devices as shown in Figure 2.2. The Young-Laplace equation governed the

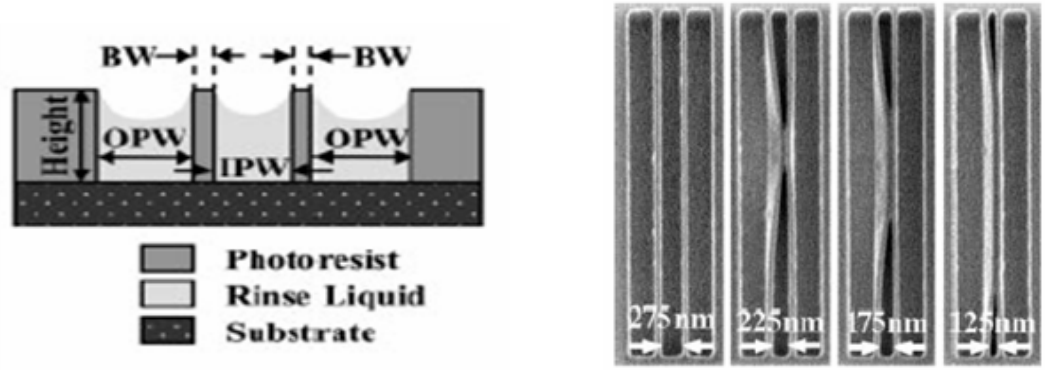

Figure 2.2 **The surface tension of water was used to determine the mechanical strength of nanoscale polymer structures. (a) Illustration of nanostructures made of photoresist with liquid meniscus. (b) SEM of deformed nanoscale structures. Structures with widths less than 275 nm collapsed due to stiction. Figures from [36].**

initial pressure difference between the test structures and was used to calculate the polymer strength.

2.2 Fern Sporangium

The ability to extract work from both environmental conditions and the surface tension of water is a hallmark of plant evolution [21]-[24]. The passive pumping of water from roots to leaves via evaporation at microscale stomatal pores is due to the cohesion-tension theory, also referred to as the cohesion theory, which explains that water in plant microvasculature is under tension generated at the leaves as water evaporates [24]. The cohesion-tension theory will be further discussed in Chapter IV. However, ferns also make use of water evaporation with specialized microstructures to obtain fast motion and high forces for spore dispersal [24]. As part of their reproductive processes, ferns grow specialized vessels called sporangia, like those shown in Figure 2.3, which house and disperse spores during certain times of the year. As they dry, these sub-millimeter scale sporangia open violently to release microscale spherical spores into the air. This mechanism is illustrated in Figure 2.4. Each sporangium is surrounded by a single layer of dead, water-filled cells called an annulus like pictured in Figure 2.3(b). Each cell is comprised of two rib-like structures filled with water. As the water inside the annulus cells dries, surface tension between the water and the cell wall gives rise to high forces causing a deflection along the outer edge of the

(a) (b)

Figure 2.3 **Fern sporangia (a) A micrograph of the back of a fern leaf showing fern sporangia clusters. Image is from [37]. Each sporangia cluster contains dozens of individual sporangium. (b) Each sporangium contains an annulus of water-filled cells that encases a collection of spores which it disperses when the sporangium is opened due to evaporation. Image is from [38].**

annulus. The combined deflection of each wall straightens the entire annulus structure and tears open the spore sac, as illustrated in Figure 2.4(b).

The discovery of the fern sporangium spore dispersal mechanism is credited to Ursprung and Renner who, in 1915, independently used the sporangium to try and measure the tensile strength of water [24],[39]. They placed sporangia in controlled test chambers in which the relative humidity was regulated by a concentrated solution. Using a microscope, they noted that the sporangia structures opened when enough water evaporated within each annulus cell to cause mechanical distortion of the entire annulus. However, they also noted that the sporangium snapped shut, to effectively throw the spores out into the air, at a solution osmotic potential of -35 MPa. Ziegenspeck, in 1928, and Haider, in 1954, both showed that the sporangium re-closed once enough water evaporated from each annulus cell (approximately 10 - 20 μm wide) to 'break' the water and form a vapor bubble inside the cell [24],[40],[41]. Interestingly, Ziegenspeck and Haider found that once a single annulus cell underwent cavitation, or generated a water vapor bubble, it promoted almost instantaneous cavitation of the rest of the annulus cells.

The issue of sporangium actuation was also investigated in the quest to understand the general theory behind the passive pumping of water in trees and plants [42]. However,

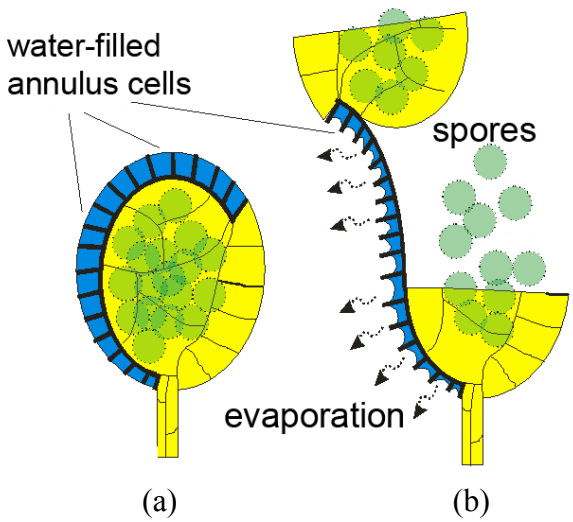

Figure 2.4 **Illustration of the actuation mechanism of fern sporangium: (a) before and (b) after evaporation induced opening of annulus to release spores (adapted from [24]).**

since the early 1950's, relatively few studies of fern sporangium mechanics have been undertaken [40]. As a whole, it should also be noted that few, if any, micro- and nano-mechanical platforms exist for testing water-pumping and actuation hypotheses for these natural structures.

2.3 Device Concept and Operation

The devices designed in this work mimic the geometries of fern sporangia, as show in Figure 2.5. Devices were designed to consist of a curved spine that straightened during device operation. The spine was also designed around the physics of a slender beam. Ribs extending from the spine create multiple individual cells with two sidewalls which can be filled with water. These ribs act as levers upon which forces due to the surface tension of water act to deform the spine, as shown in Figure 2.5(b)-(c).

Both the spine and ribs were made from a silicone polymer. In order to mimic the mechanical properties of plant cellulose, polydimethylsiloxane (PDMS) was used because of its comparable Young's modulus. Cellulose, the material that comprises plant cell walls, has a Young's modulus of 120 - 500 MPa [43]. The Young's modulus of the photopattern-able silicone employed in this work was 160 MPa, as reported by the manufacturer.

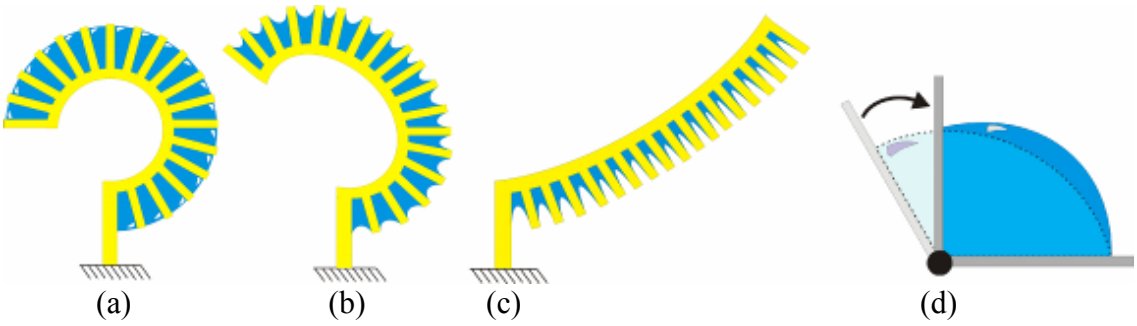

Figure 2.5 **Illustration of the actuation mechanism of microfabricated devices inspired by fern sporangium: (a) Water is placed between ribs to wet device. (b) Immediately after wetting, the surface tension of water pulls on the ribs at the meniscus edge. (c) As the water seeks to minimize its surface energy, the force due to surface tension pulls on the ribs as though they were levers and causes the spine to deform. (d) A similar example of energy minimization has been used to rotate hinges using molten solder as presented in [27] as Figure 3d. The device in (a) - (c) multiplies this energy minimization effect by incorporating multiple ribs to divide the volume of liquid.**

The behavior of these devices can be compared to previous work on melted solder-driven self-assembling plates. There has been much research on surface tension driven actuation utilizing solder at high temperatures [26],[27],[34],[35]. As illustrated in Figure 2.5(d), when the solder melts, the liquid minimizes its energy by reducing the interfacial surface area. The surface tension forces at the solder-plate interface cause the hinged plate to rotate as the liquid solder's surface energy is minimized. The microactuators in the work presented in this paper employ a distributed energy minimization mechanism by including multiple liquid volumes that seek to reduce their surface energies. As will be explained, this distribution of actuation is useful for achieving additional control such as the time response and for embedding force-generation profiles into the actuation with device geometry.

2.4 Theoretical Considerations and Model

This section shows the use of the principle of virtual work as the basis of an analytical model that predicts the mechanical energy scavenging device performance based on geometric parameters and material properties. First, the principle of virtual work is described, followed by an analysis of the various energy components in the presented system. Then, the strain energy due to deformation of the spine is derived, as well as the surface energy of the liquid between the device's ribs. The derived energy values are then used to find the minimum total potential energy.

2.4.1 Principle of Virtual Work

The task of predicting the exact nature of device deformations using force balance methods can be quite challenging for even the simple curved geometries presented in this work. Although it is becoming increasingly possible to use finite element models and commercial solvers to approach problems including surface-tension effects, large deformation analysis, and non-linear material properties, these simulations are typically computationally expensive if there are no obvious symmetries to exploit at the global level and the finite element model simulations do not always converge. In this light, energy methods based on the principle of virtual work are particularly useful and provide an efficient means of device modeling. Such methods have been used extensively to model MEMS devices [44]. The model

presented here provides an approximate solution to the maximum achievable device deformation based on geometric parameters and material properties.

In the present context, the principle of virtual work states that when a body in equilibrium experiences external forces that cause deformation, the energy added to the deformed body is solely due to those applied forces [44],[45]. In this analysis, all forces other than surface tension are neglected. The total potential energy of the microactuators presented here is the sum of the deformation energy of the device spine and the surface energy of the water columns between the ribs. The developed analytical model calculates the total energy of various resting states of the device when the ribs are completely filled with water and seeks to find the state of minimum potential energy. In the ideal case, there are no fabrication defects, the ribs are distributed evenly along the spine, each of the cells comprised of two ribs is completely filled with water, and the evaporation rate for each cell is the same at any given time. The model seeks to find the equilibrium state of the system. Transient response is not being modeled. The model is further based on the following statements:

- Devices are designed to have an initial stress free shape that is curved like a circle. A micrograph of an actual device is shown in Figure 2.6(a). The energy of the stress free curve is zero.

- The model assumes no shear forces and no out-of-plane distortion.

- The spine was designed to have uniform radius of curvature in its stress-free shape. The assumption of no shear implies that any deformed shape of the spine will also have uniform radius of curvature. An illustration of how the strain energy of the spine is calculated is shown in Figure 2.6(b). A constant arc length with an increasing radius of curvature, ρ, is used to calculated tip deflections, δ, using equation (2.1).

$$\delta = \sqrt{(x_i - x_0)^2 - (y_i - y_0)^2} \tag{2.1}$$

- Ribs are assumed to be rigid so that they do not store any deformation energy.

As the device deforms due to surface tension the strain energy in the spine increases. Equilibrium is reached when the total potential energy is at a minimum. The total system energy for a device experiencing various spine deformations, or curves, like those in Figure 2.6(b), is calculated and given in Figure 2.7(a). Each curve number corresponds to a different uniformly curved arc, ρ, for which both the strain energy of the spine and the surface energy of the water within the ribs was calculated and summed to find the total potential energy of the actuator. The curve with the lowest potential energy indicates the curve for the equilibrium state.

Simulated deformation curves are shown in Figure 2.7(b) for the point of equilibrium between the strain energy of the spine and the surface energy of the water for devices with varying spine thickness or 10, 20, and 30 μm and a rib length of 400 μm. As the spine thickness is decreased, equilibrium is reached at higher deflections.

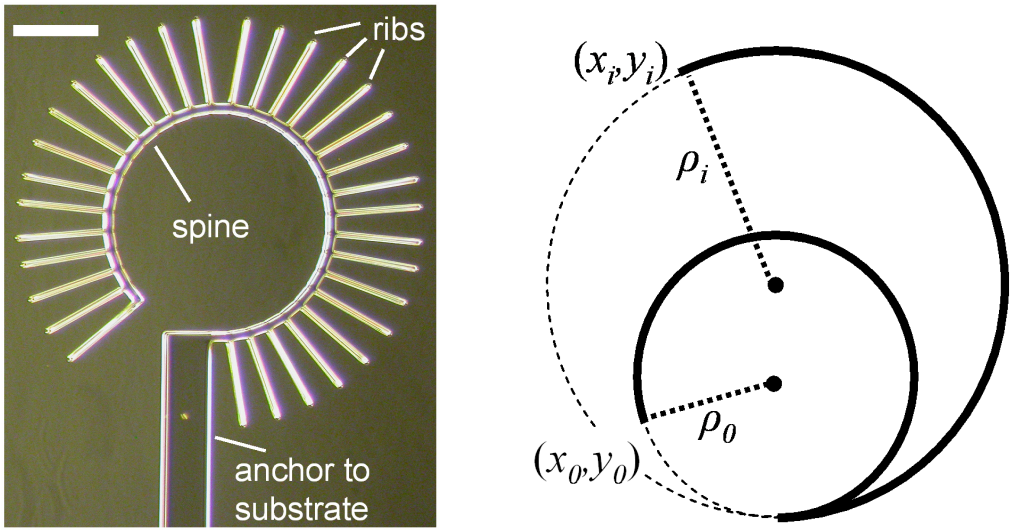

Figure 2.6 **Transpiration based microactuator: (a) A micrograph of a device in its initial rest state. The scale bar indicates 400 μm. (b) An illustration of how the strain energy of the spine is calculated, using a constant arc length with an increasing radius of curvature, ρ. Tip deflections, δ, are calculated using equation (2.1).**

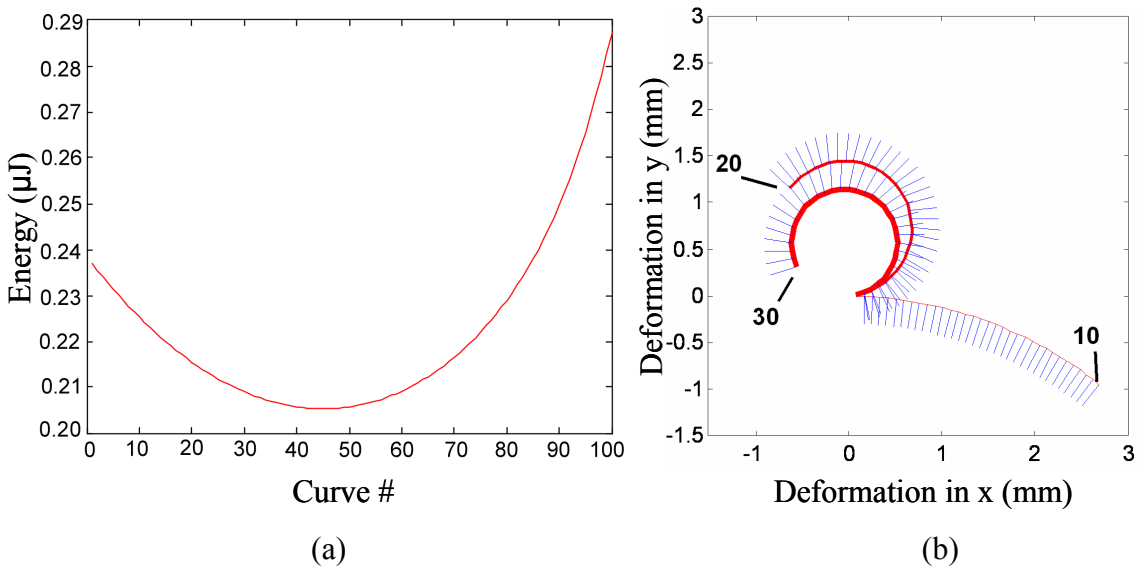

Figure 2.7 **System energy and deformation simulation results for microactuator. (a) Simulated deformation curves at the point of equilibrium between the strain energy of the spine and the surface energy of the water for devices with varying spine thicknesses (10, 20, and 30 μm) and a rib length of 400 μm. As the spine thickness is decreased, equilibrium is reached at higher deflections. (b) Simulated total system energy for a device experiencing various spine deformations represented simply as curves. Each curve number corresponds to a different uniformly curved arc for which both the strain energy of the spine and the surface energy of the water within the ribs was calculated and summed to find the total potential energy in the actuator. The modeled spine width was 10 μm with a Young's modulus of 60 MPa. The curve with the lowest potential energy indicates the curve for the equilibrium state.**

2.4.2 Strain Energy of Spine

The strain energy is defined as the integral of a scalar effort, modeled by stress, over a scalar displacement, modeled by strain [44]. The spine of the microactuator presented here can be modeled as a continuous curved beam. The strain energy density of the spine is modeled by $\tilde{W}$ in equation (2.2) where E is the Young's modulus and ε is the strain.

$$\tilde{W}(x,y,z) = \int_0^{\varepsilon(x,y,z)} E\varepsilon de = \frac{1}{2}E[\varepsilon(x,y,z)]^2 \qquad \textbf{(2.2)}$$

For large deformations in polymers, nonlinear expressions from neo-Hookean and Mooney-Rivlin models can be used and include additional non-linear terms to the axial

stress-strain relationship [46],[47]. However, the maximum strains of the geometries presented in this work do not exceed ~ 0.1 for spine thicknesses < 100 μm. Due to the small strains of the device geometries, a linear axial stress-strain relationship based on Hooke's Law, can be used [48],[49].

The strain energy is based on the physics of a straight cantilever. This is the opposite of the actual actuator geometry which is an initially curved spine Figure 2.6(a). Although there are cases in which an initially curved beam cannot be modeled using the altered equations for a straight beam, it is acceptable in this case since the calculated neutral axis radius of the straight spine is within 0.05% of the geometrically calculated curved spine value using spine thicknesses, h < 50 μm. Therefore, the energy present in an initially curved beam that is straightened during actuation is essentially equivalent to the strain energy in an initially straight beam that is then curved during actuation.

In order to calculate the energy stored in the beam, the expression must be integrated over the volume of the segment of the spine that is being analyzed. A uniform spine can be modeled by a number of small segments, each with an angle of deformation from the previous segment. The energy of segment can be found as the product of a constant and the square of the segment's angle. The total energy of the spine is the sum of all the segment energies. A sum of squares is at its minimum when all of the elements are equal. Thus, the energy of the spine would be at its minimum when all of the angles are equal, or equivalently, when the shape is in the form of a circular arc. The strain energy, W_{strain}, of a spine at deformed curve radius, ρ, radius of rest shape curve, ρ_0, Young's modulus of the spine material, E, length of spine, L, and rectangular cross-section of the spine defined by w and h, is given in equation (2.3) [50].

$$W_{strain} = \frac{Eh^3 wL}{24}\left(\frac{1}{\rho} - \frac{1}{\rho_0}\right)^2 \qquad \textbf{(2.3)}$$

As shown in Figure 2.8(a), w is defined as the depth of the device into the page and l is the in-plane thickness of the spine. The stress-free curvature, ρ_0, is given by equation (2.4), where $\theta_{initial}$ is the angle of the arc swept by the curved spine. The bending stiffness, EI, or the product of Young's modulus, E, and the moment of inertia of the spine, I, is given by equation (2.5), where h and w are as defined above.

$$\frac{1}{\rho_0} = \frac{\theta_{initial}}{L} \tag{2.4}$$

$$EI = \frac{Eh^3 w}{12} \tag{2.5}$$

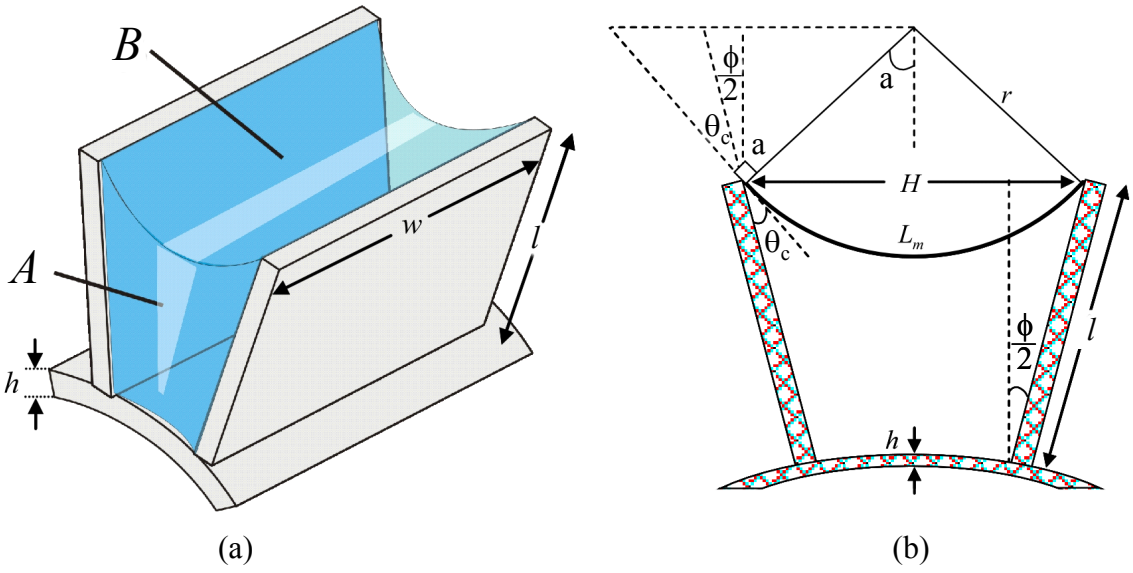

Figure 2.8 **Definition of geometric variables used in the calculation of strain energy and surface energy of the actuator. (a) The two components in the total surface energy of water: Area *A* indicates the side of the meniscus which depends on rib length, *l*, (*A* is multiplied by 2 to account for the front and back areas) and Area *B* indicates the area of the meniscus above the ribs which depends on the device depth, *w*. (b) Illustration of the variables used in the calculation of the length of the meniscus L_m: *r* is the radius of curvature of the meniscus between two ribs, *H* is the distance between the tip of the ribs, θ_c is the contact angle between water and rib, 2α is the angle sweeping the arc length of the meniscus, and ϕ is the angle between two ribs.**

2.4.3 Surface Energy of Water

As previously mentioned, the equilibrium state of the device deformation is when the total energy in the system, comprised of strain energy and surface energy, is at a minimum. The surface of the volume of water filling in the region between adjacent ribs is actually a complex three-dimensional shape. In the presented analysis, this surface has been approximated as set of trapezoids for the pair of side areas which touch both the adjacent ribs and the spine, as shown in Figure 2.8(a), Area *A*, and as a partial cylinder of appropriate radius for the top areas which touch just the adjacent ribs, as shown in Figure 2.8(a), Area *B*. The sum of these two regions provides an approximation of the surface area of the volume of water present between the ribs. The work done by the surface tension of water, $W_{surface}$, for a given spine deformation is expressed by equation (2.6) where γ_t is the surface tension of water, *A* is the area of the side meniscus on both sides of the device, *B* is the area of the top meniscus between the tips of a set of ribs, and *n* is the number of ribs.

$$W_{surface} = 2\left(\sum_{0}^{n}\gamma_t \cdot A\right) + \sum_{0}^{n}\gamma_t \cdot B \tag{2.6}$$

The area of the side meniscus, *A*, can be approximated by a trapezoid that depends on the length of the rib, *l*, as given by equation (2.7). The curvature of the surface due to the meniscus of the water is neglected for cases where the depth of the rib, *w*, is much greater than the distance between the tips of the ribs, *H*.

$$A = l\left(H - \tan\frac{\phi}{2}\right) \tag{2.7}$$

The length of the meniscus, L_m, within each cell from rib-tip to rib-tip can be solved using the water-to-rib contact angle, θ_c, and a geometric construction presented in equations (2.8)-(2.10), where *r* is the radius of curvature of the meniscus between two ribs, ϕ is the angle between two ribs, *H* is the distance between the tip of the ribs, and *w* is the depth of the ribs as defined in Figure 2.8(a). The partial cylinder used to approximate the top area, *B*, takes into account the menisci generated by the liquid-solid interface and is given by equation (2.11).

$$\alpha = \frac{\pi}{2} - \frac{\phi}{2} - \theta_c \tag{2.8}$$

$$r = \frac{H}{2\sin\alpha} \tag{2.9}$$

$$L_m = 2\alpha r \tag{2.10}$$

$$B = L_m w - 2(\alpha r^2 - r^2 \sin\alpha\cos\alpha) \tag{2.11}$$

The approximation for B subtracts the area that does not contain water due to the concave shape of the meniscus along the depth of the ribs, w, in Figure 2.8(a). The calculation for B also subtracts the area due to the concave meniscus at the tip of the ribs coming from the side of the volume of water. In equation (2.11) the unadjusted partial cylinder area is given in the first term, $L_m w$, and the subtracted areas due to the menisci are given in the second term, $2(\alpha r^2 - r^2\sin\alpha\cos\alpha)$. These approximations result in a value for the total surface area of the water contained within a set of ribs which takes into account the contact angle, θ_c, of water to the ribs.

2.5 Device Fabrication

The microactuators in this work were batch fabricated using the photopatternable silicone WL-5150 from Dow Corning in a single mask process. Figure 2.9 shows the process steps in the fabrication sequence. A passivation layer was deposited on a clean wafer using a Surface Technology Systems ICP-DRIE tool for 1 minute with 85 sccm of C_4F_8 at 800 W of power. This hydrophobic layer facilitates the removal of the silicone structures from the silicon substrate post fabrication. The photopatternable silicone was warmed to room temperature, and was then deposited and spun onto the passivated wafer at 300 rpm for a depth, or vertical thickness, of 80 μm on the substrate. The coated wafer was then soft baked on a hotplate at 110ºC for 2 minutes to remove carrier solvents. The patternable silicone layer was exposed to 1000 mJ/cm^2 of UV-light using a GCA Autostep 200 i-line stepper to activate polymerization. The exposed silicone layer was then baked on a hotplate for 2 minutes at 150ºC to achieve full polymerization of the exposed regions. Stoddard solvent, which

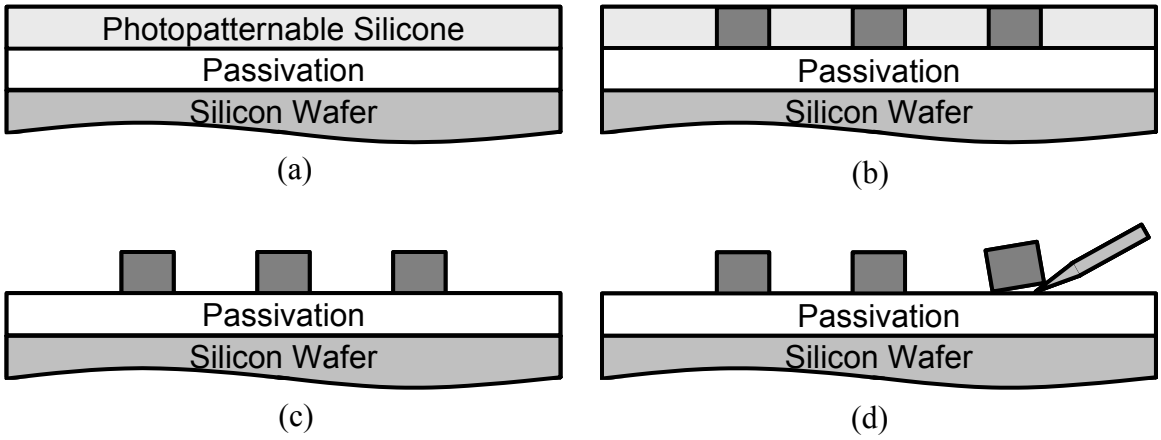

Figure 2.9 **Fabrication sequence of lithographically patterned polymer actuators: (a) A thin passivation layer is deposited on a bare wafer and photopatternable silicone is spun on top. (b) Negative photolithography is used to activate polymerization of the silicone. (c) The silicone is developed. (d) The patterned devices are removed from the wafer.**

was also obtained from Dow Corning, was used to remove the unexposed silicone during a 1-minute puddle development. Fresh developer was deposited onto the wafer with a pipette for 10 seconds as it was spun at 200 rpm. Isopropyl alcohol was then squirted onto the wafer while it as spun at 500 rpm to remove solvents and any undeveloped silicone. Subsequently, the wafer was spun dry for 30 seconds at 500 rpm. The final photopatterned silicone features were cured on a hotplate at 250ºC for 10 minutes. The microactuator devices were separated from their carrier wafers using a razor blade. Next, they were immersed in methanol and dried on a clean silicon wafer. Following this, the devices were lifted from the wafer and mounted at their base anchor for testing. Finally, a 50 W, 2-minute O_2 plasma treatment at 250 mTorr was used to make the structures hydrophilic prior to testing.

2.6 Device Testing

Following the O_2 plasma step, water was applied onto the hydrophilic surfaces using a needle and syringe. Evaporation took place at room temperature. Device actuation was observed and recorded using a Nikon Coolpix 5 Megapixel digital camera mounted on a compound microscope using 10 times magnification. In some cases, 10 μM fluorescein (Sigma-Aldrich Corporation) was dissolved in deionized water to help visualize the water and the meniscus.

2.7 Experimental Results

2.7.1 Device Performance Metrics

Device performance was quantified in two ways:

- Device tip deflection, which is measured as the distance that the entire device tip at the last rib moved from its initial position to the point of equilibrium; and
- Angular rotation, which measured the angle swept by the device tip from the starting position to the point of equilibrium.

In order to test the derived analytical model and understand scaling phenomena, a family of devices with parametrically varied geometries was fabricated and assembled. The varied parameters of rib length, rib spacing, spine thickness and device depth, enabled the investigation of the effect of linear scaling on the magnitude of total device tip deflection, angular rotation, as well as the geometry of deformation and geometry controlled time response to evaporation-driven actuation.

Typical as-drawn geometric parameters of the fabricated devices include: 300, 400, and 500 μm rib lengths, constant 75 μm rib spacing, 10, 20, and 30 μm spine thicknesses, and 80 μm device depth (the thickness of the spun photopatternable silicone). Using scanning electron microscopy (SEM) of rib cross-sections, the dimensions of actual fabricated device spine and rib thicknesses were found to be larger than design due to aspect ratio limitations of the photopatternable silicone as shown Figure 2.10. The additional thickness was incorporated into the analytical model for a direct comparison of the theoretical predictions with the experimental data. Multiple sets of identical devices were tested to ensure repeatability.

Figure 2.11 shows a time-lapsed typical device movement during actuation. Once wetted, devices quickly moved to their equilibrium position, as shown in Figure 2.11(b)-(c). As water evaporated, the devices began to relieve the strain in the spine. Devices returned to their undeformed state once dry.

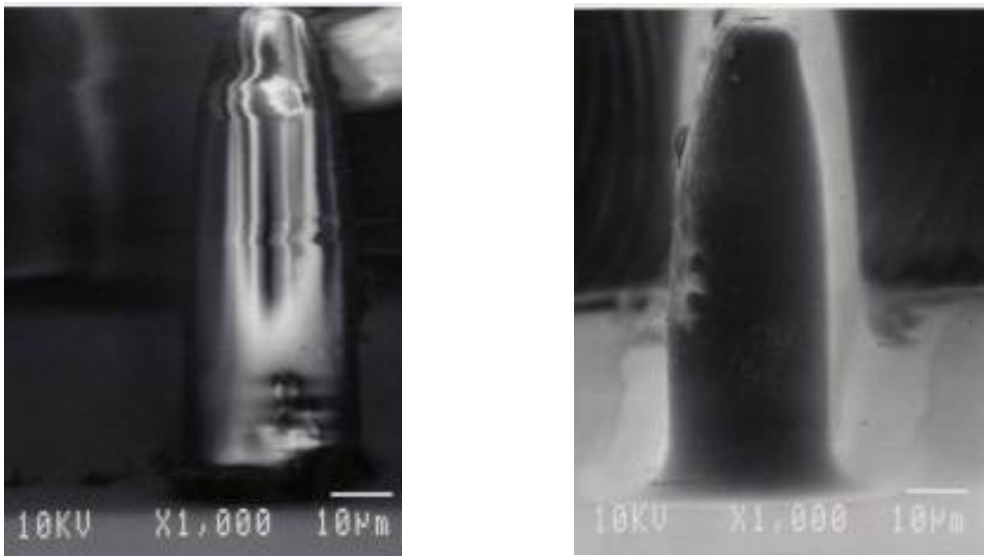

(a) (b)

Figure 2.10 **Scan Electron Microscope images of device features. (a) An SEM image indicating rib width. The polymer in this image has no metal alloy sputtered, thus contains significant charging from the electron beam. (b) The polymer in this SEM image has approximately 30 nm of Gold Palladium alloy sputtered to capture a clearer image without charging. Both images indicate that 10 µm ribs are in fact wider than designed. Scale bars indicate 10 µm.**

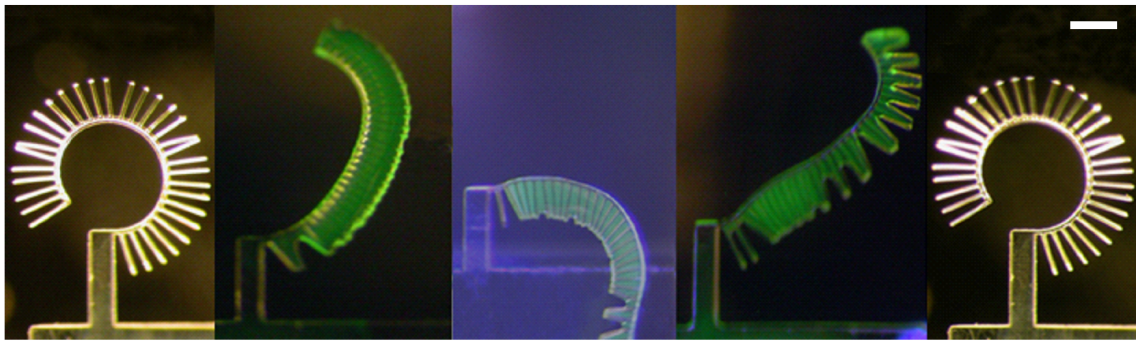

(a) (b) (c) (d) (e)

Figure 2.11 **Micrographs of an actuator device unfurling: (a) Completely dry device before filling. (b) Wetted device 0.5 seconds after filling. (c) Device at full deflection 2 seconds after filling. (d) Device drying at 30 seconds after filling. (e) The device returns to its original profile once water evaporates completely. 10 µM of fluorescein was added to the water to help visualize meniscus. Scale bar indicates 400 µm.**

2.7.2 Device Performance as Function of Spine Thickness

Devices with the smallest feature size of 10 μm spine thicknesses experienced resultant tip deflections in excess of 4 mm while unfurling 300°, as shown in Figure 2.12(a)-(b). Devices exhibited forces per unit length ranging from 5.75 mN/m for 10 μm spine thicknesses to 67.67 mN/m for 30 μm spine thicknesses. Decreasing the spine thickness predictably increased the deflection of the device, but also increased the spread of the measured data as the device became more sensitive to test environment conditions.

The data in Figure 2.12(a) show an increase in the standard deviation as the spine thickness is decreased. This is partly due to test environment limitations. Since the test environment of an optical microscope for image capture cannot be guaranteed to provide evenly distributed light, devices with narrower spine geometries expressed the variation much more noticeably than wider devices which did not deflect as much. The variation among a given spine thickness is rather constant relative to total angular rotation and displacement.

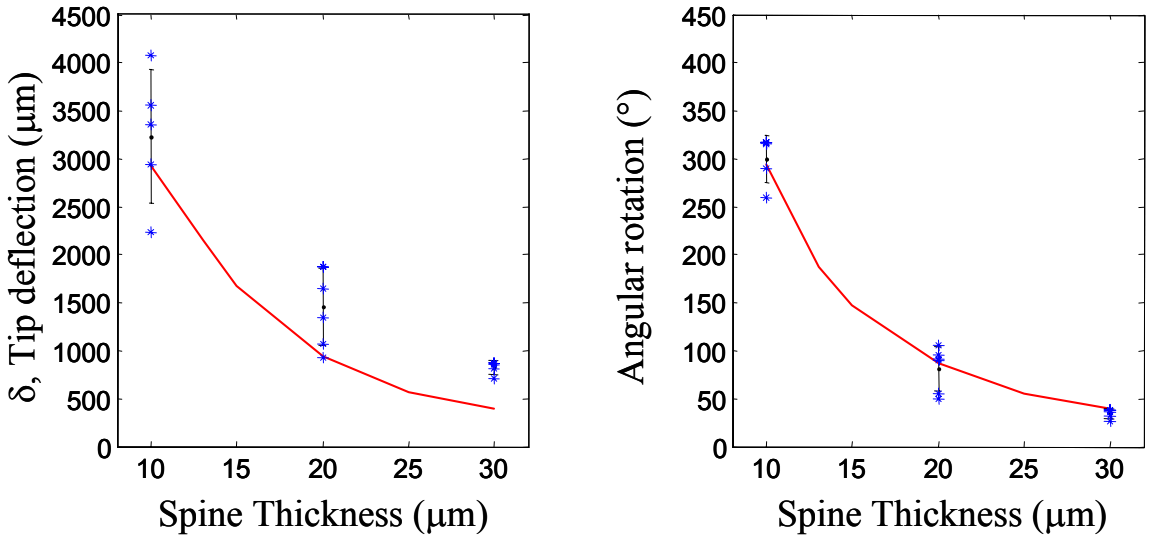

(a) (b)

Figure 2.12 Measurement and simulation results of device performance versus spine thickness. (a) Tip deflection, δ defined in equation (2.1), at the tip of device as a function of spine thickness (rib length = 400 μm). (b) Angle of rotation of as a function of spine thickness (rib length = 400 μm). The results of the simulation are given in red for a Young's Modulus value of 60 MPa.

2.7.3 Device Performance as a Function of Rib Length

Devices with varied rib lengths also exhibit variability due to the test environment, as can be seen from the standard deviation in Figure 2.13. Also, as the rib length was increased, the ribs touched and prevented further deformation Figure 2.13(c), which explains why the data seems to be at the same value even for the rib lengths tested. As seen in Figure 2.13(a), the results of the analytical model fit the empirical data at silicone modulus values of 50 - 70 MPa. This matches previous observations that the Young's modulus of PDMS can vary substantially depending on degrees of cross-linking, humidity, and surface treatments such as O_2 plasma treatments [51],[52].

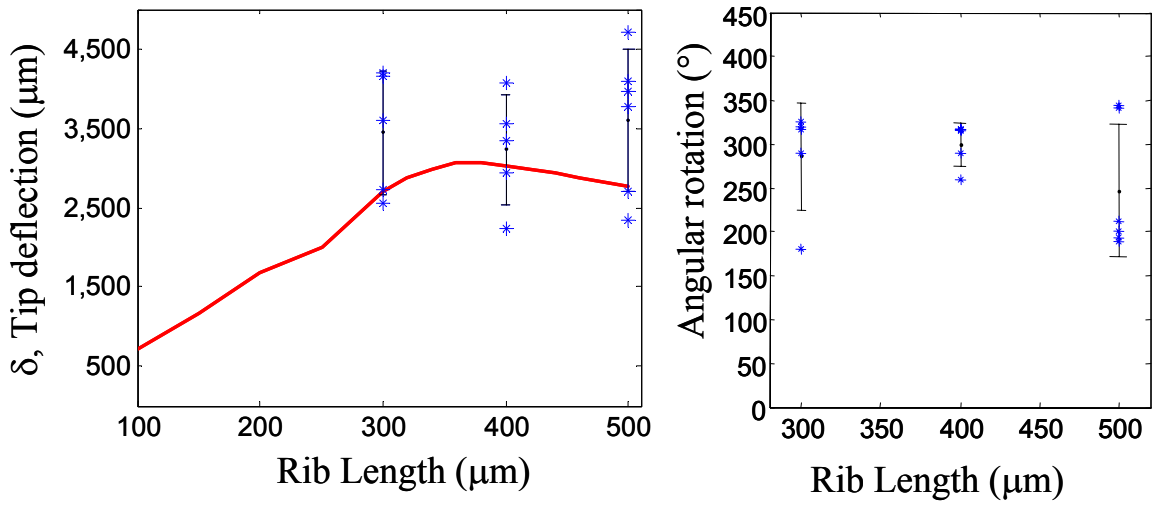

(a) (b)

Figure 2.13 Measurement and simulation results of device performance versus rib length. (a) Deflection, δ, at tip of device as a function of rib length (spine width = 10 μm). The simulation included 100 and 200 μms to show the decreasing deformation at short rib lengths. However, increased rib length does not seem to affect deformation since the space between ribs was held constant and devices could not deflect any further than a certain point. (b) Angle of rotation as a function of rib length (spine thickness = 10 μm). An angular rotation of 330° indicates a device actuated from the undeformed arc into a straight line. The results of the simulation are given in red for 60 MPa.

Table 2.1 A comparison of microactuators and their characteristics. Table adapted from [53] and transpiration based actuator characteristics added from this work.

Type of micro actuator	Displacement	Force/Torque	Driving Energy
Electromagnetic motor	Rotating	1 mNm	Electric current
Thrust type electromagnetic actuator	Length of solenoid	10 mN	Electric current
Electrostatic micro motor	Rotating	10 pNm	Electric voltage
Comb type electrostatic actuator	Length of comb	0.2 mN	Electric voltage
Stacked-type piezoelectric actuator	0.1% of length	5 kN/cm^2	Electric voltage
Bimorph-type piezoelectric actuator	1-5% of length	10 N	Electric voltage
Wired shape memory alloy actuator	3% of length	10 kN/cm	Heat
Polymer actuator	1-50% of volume	1 N	Heat, current
Transpiration-based actuator	Length of actuator	5.8 mN/m to 67.7 mN/m	Surface tension, evaporation

2.7.4 Comparison with Other Micro Actuator Technologies

The microactuators in this work can be compared to other actuators using the displacement, force or torque, and the driving energy of the actuation mechanism. A survey of microactuator technology can be found in [53]. Table 2.1 compares the transpiration based actuators with state of the art actuators using the parameters listed above.

2.7.5 Drying of Liquid Phase Meniscus as a Function of Device Geometry

In addition to the quantifiable differences in device performance as a function of rib length and spine thickness shown in Figure 2.12 and Figure 2.13, additional visual observations were made as a result of the varied geometric parameters. This information is not captured by the analytical model since the model seeks to find the point of equilibrium and not the transient response.

The drying of the liquid phase was found to exhibit a varied response to rib length. For shorter rib lengths of 300 μm, the meniscus was observed to dry from the rib tips towards the spine, as can be seen in Figure 2.14(a). At a certain time point, many devices underwent a breaking of symmetry due to varied light intensity in the test environment, as can be seen in Figure 2.14(b). However, it is interesting to note that devices in which the

meniscus dried toward the spine slowly returned to their starting position at a rate proportional to the evaporation of water.

For devices with longer rib lengths of 500 μm, the actuation is so extreme that the ribs are forced into contact, as captured by Figure 2.15(a)-(b). Note that, unlike the typical MEMS stiction of two cantilevers [54], the liquid is observed to dry towards the point contact at the tip of the ribs and away from the spine, as seen in Figure 2.15(c). Since the liquid dries towards the tips of the ribs, the device remained completely deformed at its point of equilibrium until all the liquid evaporated. At that point the ribs immediately separated and the microactuator snapped back to its starting position.

Both of the drying phenomena described above can be seen in different parts of the device in Figure 2.11 which had rib lengths of 400 μm. Variations in light intensity in the test environment are the most probable cause of uneven drying between cells of the same device as it returned to its starting position.

The takeaways from Figure 2.14 and Figure 2.15 indicate that the meniscus can be geometrically programmed to dry towards the spine using shorter rib lengths, or to dry towards the tip of the ribs, using longer rib lengths that touch at the tip during actuation. This also allows for control of the speed with which a device returns to its original position. Devices with shorter rib lengths returned to their original position in a gradual manner,

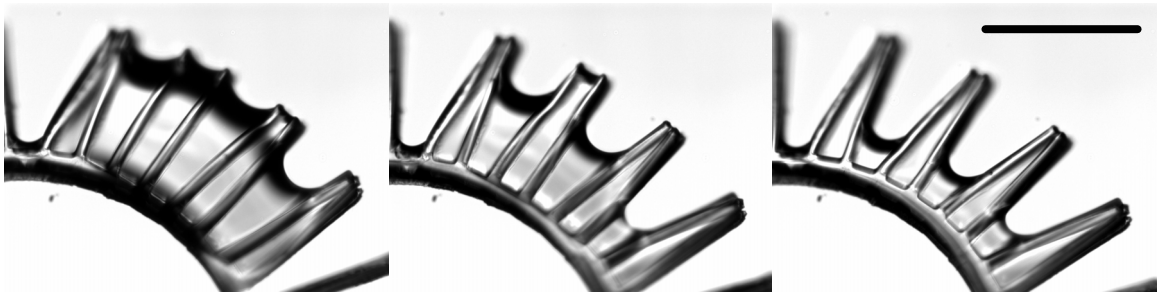

(a) (b) (c)

Figure 2.14 Observations of drying phenomena in between ribs due to uneven test environment: (a) Drying of liquid phase for device whose ribs are not forced into contact. (b) - (c) At a certain time point devices undergo a breaking of symmetry due to uneven test environments which cause the water within some cells to evaporate faster than in others (i.e. non-uniform light intensity). Images are two seconds apart. Scale bar indicates 300 μm.

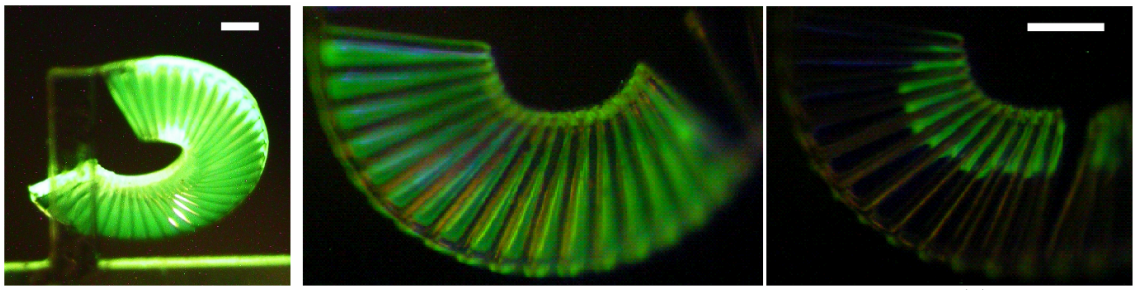

(a) (b) (c)

Figure 2.15 Geometric control of the way that the device returns to its original position: (a) A photograph of a device whose deflection is so extreme that the ribs are forced into contact. (b) Close-up of the device drying to show the liquid phase. The liquid is observed to dry towards the tip of the ribs. (c) Due to the direction of the receding meniscus during drying, the device remained completely deformed at its maximum possible actuated position until all the liquid evaporated. Scale bar indicates 250 µm.

---

while those with longer rib lengths snapped back to their original position when the last drop of liquid holding two rib tips together dried.

2.8 Bottom-Up Assembly: Generating Stable Shapes

All of the devices discussed so far returned to their original position after evaporation was complete. However, this transient mechanism of transpiration actuation can be used to generate stable self-assembled configurations. Figure 2.16 shows two simple ribbed actuators fabricated near each other. Independently, each of these devices functioned as described above, transiently deflecting and then returning to their initial configuration upon drying. When the devices were positioned properly, there was a point at which the total water surface energy was reduced by forming a continuous water surface across the ends of both devices, as shown in Figure 2.16(b). As this occurred, the devices came into contact at certain points and interlocked, as captured by the micrographs in Figure 2.16(b)-(e).

Once dry, the composite device stayed in its new configuration, as shown in Figure 2.16(e). This is due to the large areas which come into contact during actuation (i.e. ribs along their entire length), experience stiction, and thus cause the two actuators to stay together when dry. This shows that one can geometrically define devices such that during actuation, large surface areas come into contact and adhere due to stiction. For a single

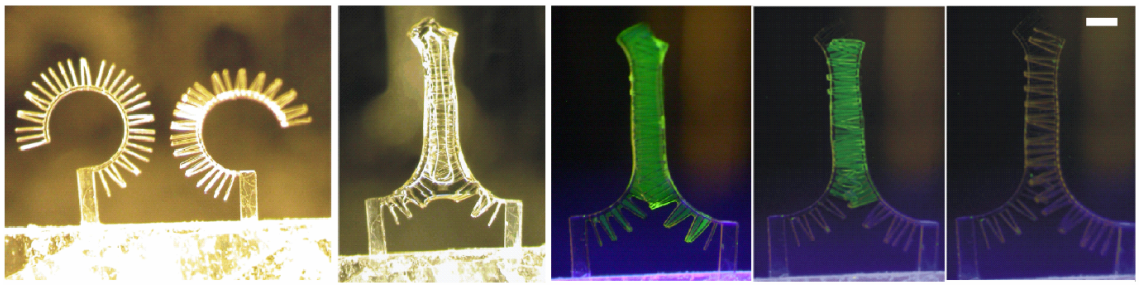

(a) (b) (c) (d) (e)

Figure 2.16 Two microactuators arranged so that the transient actuation due to evaporation leaves them in a different, stable configuration after they dry. (a) Two dry devices before adding water; (b) after adding water independently to each structure, the devices interlock into a new, stable configuration (c) - (e). Fluorescein dye was used to show how the liquid phase dries, leaving a stable configuration. Scale bar indicates 400 µm.

actuator, the only possible areas for stiction are the very small surface areas at the rib tips. That small area is not large enough to cause stiction for an independently actuating device. Therefore, single actuators are able to return to their original positions without experiencing stiction.

Additional devices were fabricated to show that a small number of ribs could move large slabs of polymerized silicone. A curved slab of silicone (0.5 x 0.25 mm^2) was moved 2.5 mm via the evaporation of water between fifteen ribs, as shown in Figure 2.17.

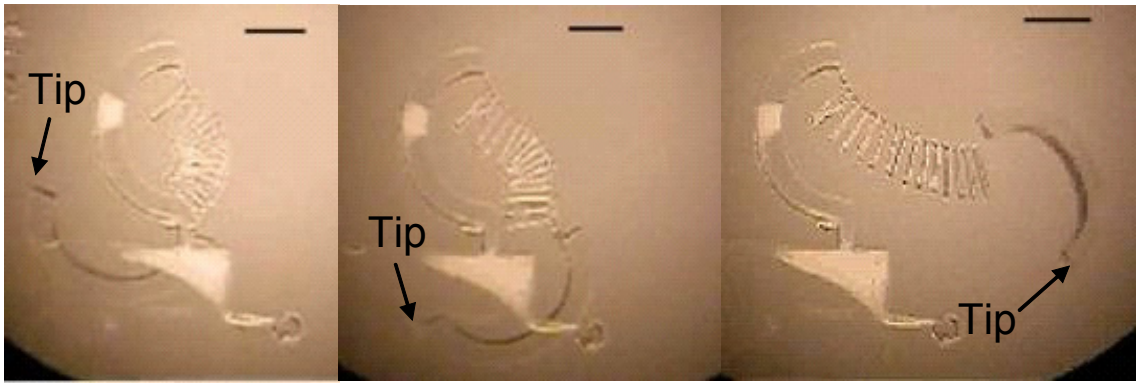

(a) (b) (c)

Figure 2.17 A microactuator designed to move a large slab of silicone using 15 ribs. Images are 2 seconds apart. Scale bar indicates 500 µm. (a) Tip at maximum deflection (b) Tip moves as water between ribs dries (c) Water has completely dried and tip has returned to its original position.

2.9 Transpiration Actuation in the Nanoscale Regime

In the developed transpiration actuation devices, the force due to surface tension was a dominant force at the microscale and allowed for large deflections in millimeter sized devices. Similarly, at the nanoscale, surface tension is also a dominant force and could be used for actuation. Simulation results from the developed analytical model for the micro-actuator indicate that deflection relative to the size of the device was size-invariant and that nano-scale structures would exhibit relative deformations as large as the micro-scale devices. Figure 2.18 shows predicted tip deflections and angular rotations for nano-scaled devices using the Young's modulus value of 3.75 GPa for e-beam lithography definable PMMA [55].

Poly(methyl methacrylate) (PMMA) was used to fabricate the nanoscale version of the actuators because it can be patterned using e-beam lithography and is compliant, with Young's modulus values from 2.75 to 3.75 GPa depending on the relative humidity [55]. Hexamethyldisilazane (HMDS) photoresist adhesion promoter was spun onto a clean silicon wafer at 2500 rpm for 60 seconds. A 600 nm layer of Nano 8.5% methacrylic acid (MAA) and methyl methacrylate (MMA) copolymer from Microlithography Chemical was spun at 2500 rpm for 60 seconds and baked in an oven at 180^{o}C for 15 minutes. A 100 nm

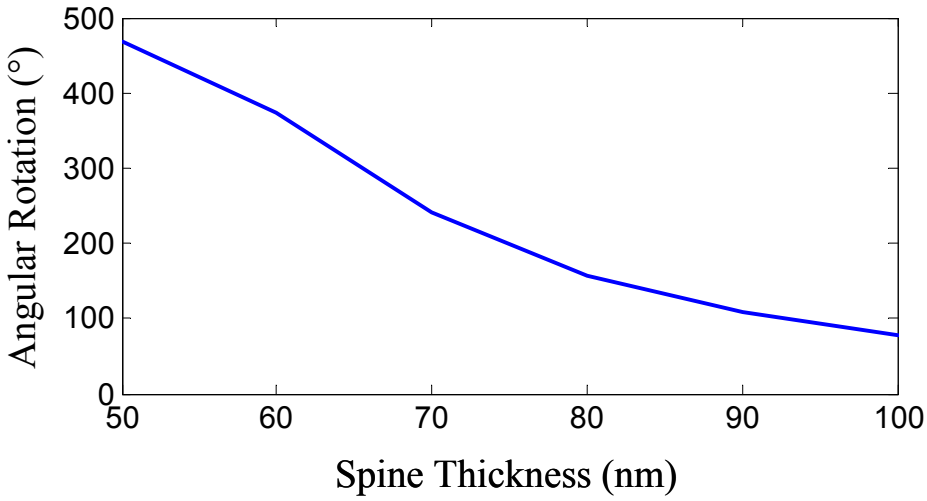

Figure 2.18 Simulation results of the angular rotation of nano-scaled devices with the sporangium inspired design using PMMA Young's modulus of 3.75 GPa. Theoretical predictions are shown as a function of spine widths from 50 to 100 nm.

layer of PMMA in 2% Anisole solution from Microchem was spun on and baked in an oven at 180^{o}C for 15 minutes. The PMMA and copolymer were patterned using a Raith-150 E-beam lithography system and developed in an Methyl isobutyl ketone (MIBK):IPA 1:3 solution for 60 seconds. The fabrication process flow is illustrated in Figure 2.19. The copolymer is three times more sensitive than PMMA to the e-beam and as a result, was overexposed to create a suspended PMMA structure on copolymer anchors, as shown in Figure 2.19(d).

Nano-scale devices with 80 nm features and 800 nm x 800 nm total area were fabricated with a single set of ribs and tested in a FEI Quanta 200 3D Focused Ion Beam Workstation and Environmental Scanning Electron Microscope. Scanning electron microscope images of completed devices are shown in Figure 2.20.

During testing, the chamber humidity of the FEI Quanta 200 was increased such that water nucleated between device ribs. Once a meniscus formed, chamber humidity was reduced to induce evaporation and actuation. Multiple ribs were necessary for actuation and as a result, the two-ribbed devices did not deflect substantially (< 10 nm).

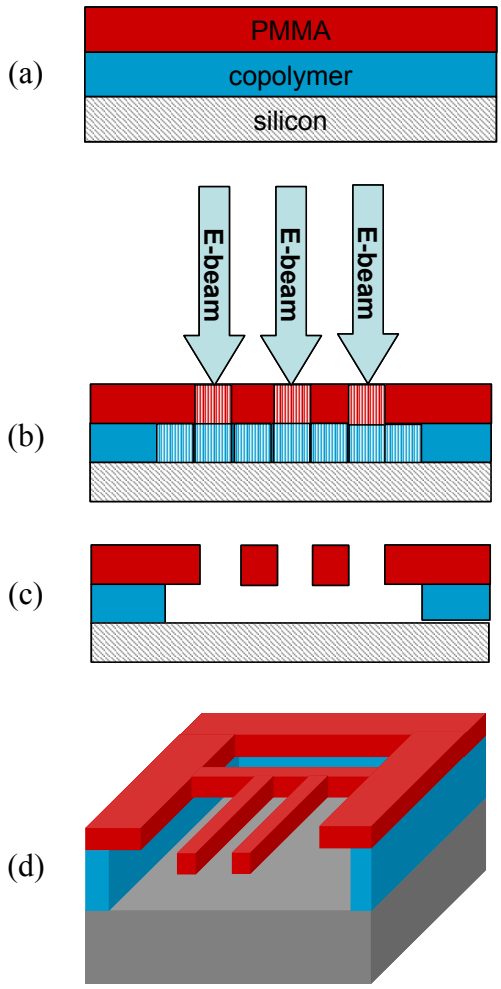

Figure 2.19 **Nano transpiration actuator device process flow. (a) A 600 nm layer of MAA-MMA copolymer was spun onto a wafer then soft-baked in an oven. A 100 nm layer of PMMA was spun on and baked also soft-baked. (b) PMMA and copolymer were patterned using an e-beam lithography tool. The copolymer is three times more sensitive to e-beam than PMMA, and was overexposed to generate an air gap (c) Polymers were developed in a 1:3 MIBK:IPA. (d) The over-exposed copolymer allowed for a suspended PMMA structure.**

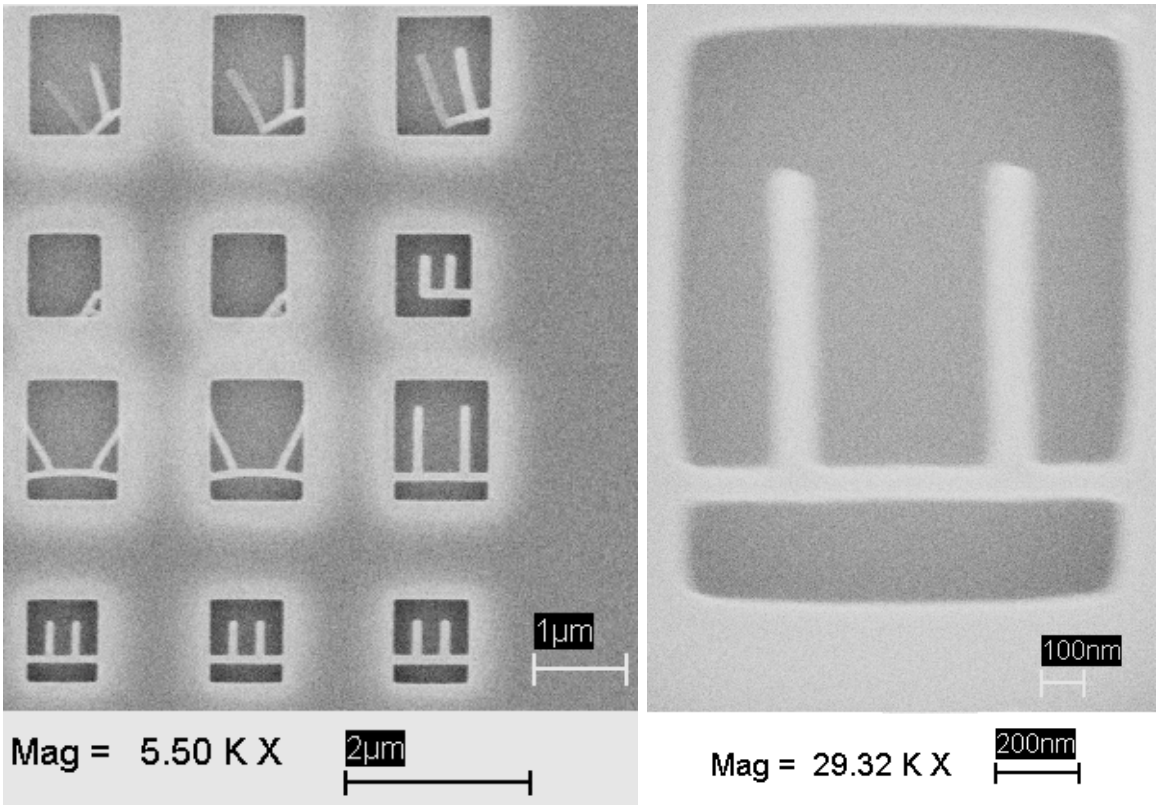

(a) (b)

Figure 2.20 A scanning electron microscope image of nanoscale transpiration actuators. (a) Multiple nanoscale devices shown magnified at 5,500X. Some devices experienced stiction during wet chemistry development. The devices that withstood development were tested. (b) A nanoscale device with an 80 nm spine width and 100 nm rib widths, shown magnified at approximately 30,000X magnification.

The three main challenges faced during testing of the nano actuators were that:

- The PMMA polymer distorted after long exposure to the scanning electron beam. A scanning electron image of a distorted polymer structure is shown in Figure 2.21.
- Images captured at high humidity in the E-SEM contained significant noise which made transient observation of device behavior impossible. The noise progression with humidity can be seen in Figure 2.22.
- Precise and fast control of the rate of change of the relative humidity in the chamber was not possible, thus, too much water would form and would pull the nano-scale devices down towards the substrate.

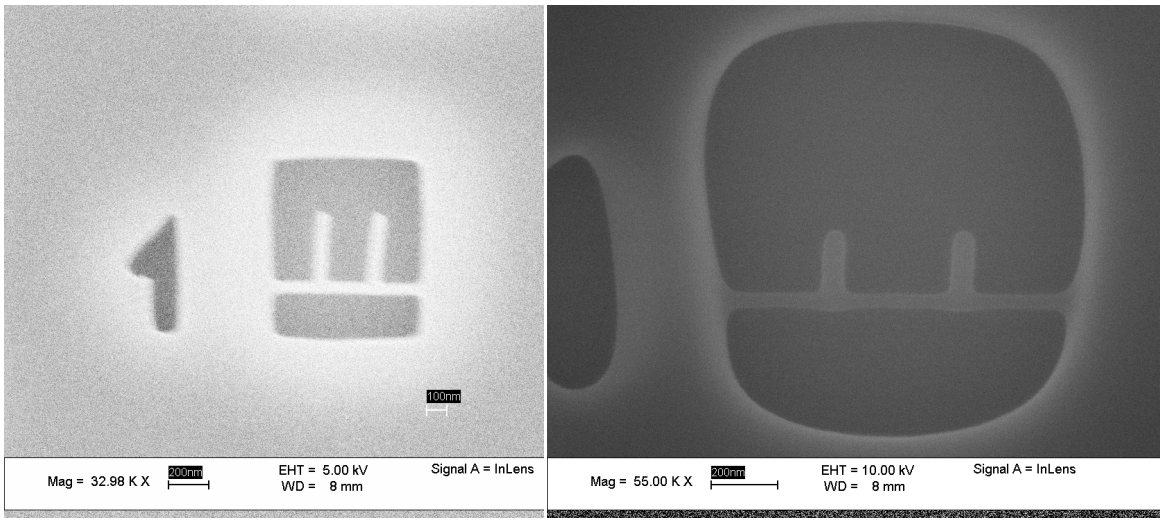

(a) (b)

Figure 2.21 **Electron micrographs of a distorted nanoscale polymer device. (a) Very short exposure of less than 5 minute at approximately 33,000X magnification. (b) After 5 minutes. Long exposure to the electron beam deformed the polymer at approximately 40,000X magnification.**

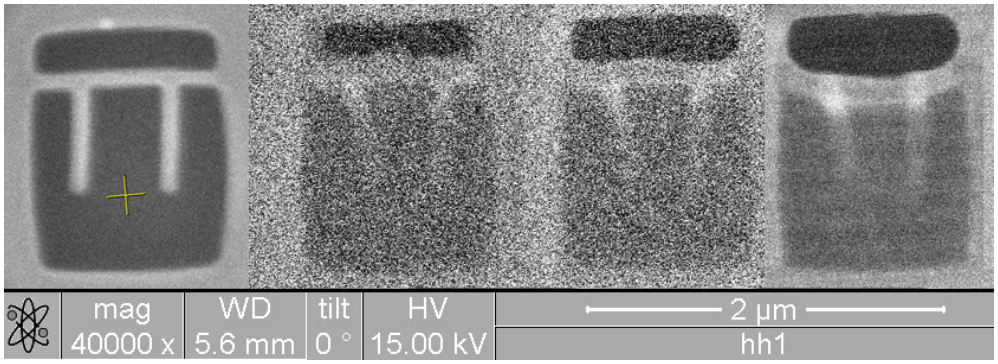

(a) (b) (c) (d)

Figure 2.22 **Multiple SEM images of controlled water condensation and drying in a nanopatterned device. Device ribs were 100 nm wide, 700 nm long, and spaced 300 nm apart. The bridge support beam was 80 nm wide. (a) Relative humidity of the E-SEM chamber was set to 12.5% and device was completely dry. (b) Humidity was increased to 85% within 1 minute. (c) and (d) Humidity was then set to 52%. A large water bubble formed underneath the structure and found it energetically favorable to pull the device support down due to surface tension forces. Further, in (d) it is possible that the electron beam in the SEM deformed the polymer after long imaging times. Note: Images captured at high humidity values contain noise and as a result, are less clear than images captures at low humidity. Devices magnified 40,000X for image.**

If the test environment and material challenges are overcome, the presented nano actuation scheme could be used in nanoscale self-assembly. Furthermore, the presented structures could contribute to the understanding of the tensile behavior of water at the nanoscale - a subject that has been and continues to be investigated [24].

2.10 Future of Transpiration Actuation: Materials

In an attempt to engineer moisture-actuated materials, macroscale sheets of silicone measuring 2 cm x 0.5 cm x 50 μm were embedded with parallel ribs similar to those in the individual actuators described previously in this chapter. A comparison between the sheets and the original actuators is shown in Figure 2.23.

Figure 2.24(a)-(b) shows one such sheet deflecting due to transpiration actuation; rib width and spacing in this sheet are constant (100 μm). Figure 2.24(c)-(d) shows a sheet of material where rib spacing decreased from top to bottom. The bottom tip, which contained denser ribs (and thus more force density) actuated more drastically. The devices in Figure 2.23 and Figure 2.24 were designed as proof-of-concept that transpiration actuation could be embedded in sheets of materials with pre-programmed force and deflection responses using a similar approach to one used for the independent sporangium-like actuators.

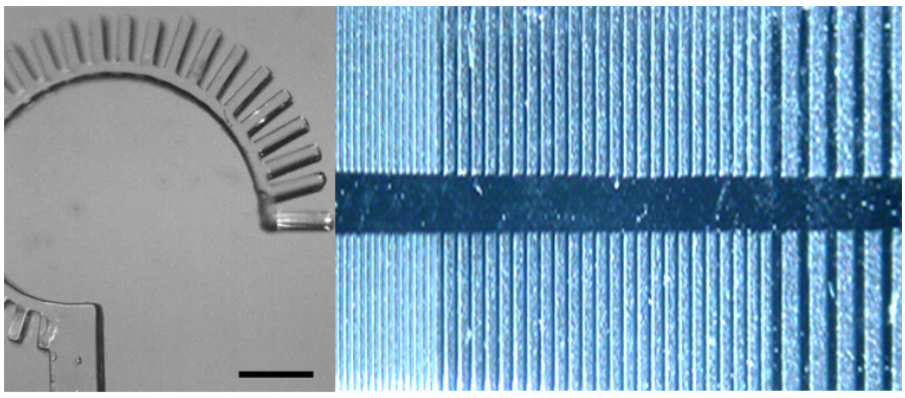

(a) (b)

Figure 2.23 Image comparison of original microactuators and micro actuating sheets. (a) Sporangium inspired device (b) Macroscale sheets with embedded channels for actuation. This sheet shows a width grating where the width of the side channels increases from left to right. The center channel was used to load the side channels with water. The scale bar indicates 250 μm for both images.

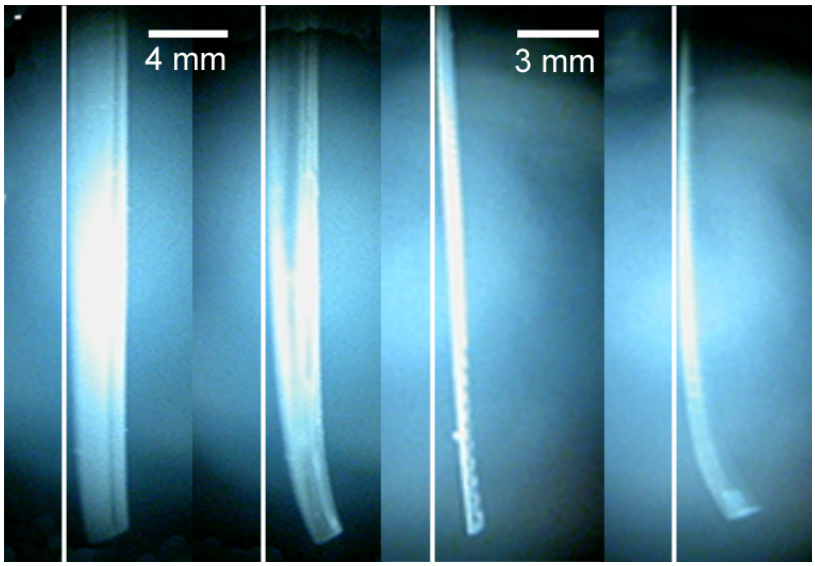

Figure 2.24 **Side-view of large actuating sheets before and after actuation. Deflection can be seen by comparing device to the straight line to the left of each actuator. (a) Before water loading. The side channels in this device are 100 µm wide (b) After water loading. (c) Before water loading. The side channels in this device have a width grating of increasing side channel widths from top to bottom. (d) After water loading. Note the difference in the scale bars between the first and second device.**

The concept of programmable force profiles gains added power when implemented in two dimensional materials. Figure 2.25 illustrates an example of how altering the direction and shape of microchannels would result in programmable patterns of deformation and force delivery.

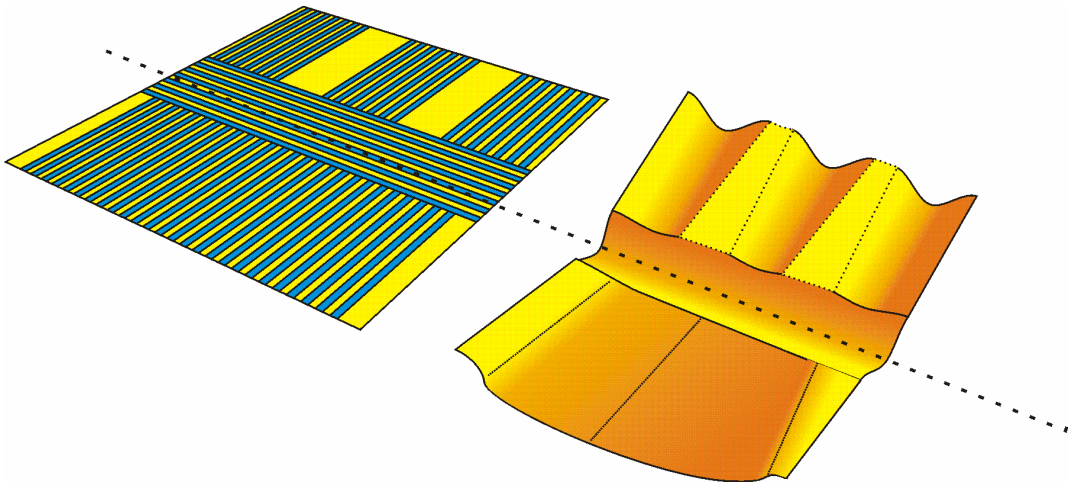

Figure 2.25 **An illustration that shows how a material can be programmed to deflect from evaporation within defined microchannels based on geometric parameters.**

2.11 Summary of Chapter Contributions

This section presented transpiration actuation devices which utilize the pulling force of the surface tension of water on patterned ribs to deform structures in predictable ways. This type of actuation method has been little studied as a micro or nanomechanical system. The structures presented in this thesis chapter have demonstrated large deformations due to surface tension. This method of actuation was also presented as a method of bottom-up self-assembly in which adjacent devices actuate and interlock into more complex and stable configurations. An analytical model based on the principle of virtual work was developed to predict actuator deflection and rotation. This analysis indicated that deflection relative to the size of the device was size invariant and that nanoscale structures would exhibit relative deformations and angular rotations as large as the microscale devices if the material's Young's modulus is scaled inversely with device spine thickness. Empirical observations showed that the deflection profiles of the actuators might be further tuned with environmental controls such as light or heat sources, and with more interesting geometries achieved by staggering or varying spine geometry or rib length throughout a single device. These variables could be used to change the speed, location, and direction of actuation. The presented actuation scheme provides a possible route towards embedding evaporation-induced actuation into common materials. This mechanism could be further explored to create two-dimensional, programmable sheets of material that deform as a function of humidity or to create nano-scaled actuators that operate as a function of humidity.

CHAPTER III

ENERGY SCAVENGING TECHNOLOGY

Advancements in semiconductor technology have reduced both the size and power consumption of electronic devices, and thus have enabled the development of portable and wireless devices for various applications such as sensing, data collection, data transmission, and mobile computing. As various components of electronic computing and sensing have experienced exponential performance gains, battery storage densities have experienced modest growth rates of 8% per year, as was shown in Figure 1.1 [6]. Large networks with many wireless sensor nodes generally require each node to be battery-operated as it is not practical to route physical wires to each individual node, especially across large areas. However, batteries do contain a finite amount of energy and eventually run out. Thus, alternative energies are needed to reduce sensor battery replacement, maintenance, and installation costs - which can comprise up to 80% of the cost of a wireless sensor.

This chapter will give an overview of the different types of energy scavenging technologies, the theory behind their operation, as well as examples of the state of the art devices in each area.

3.1 Overview of Electrical Energy Scavenging

A solar cell is a good example of a ubiquitous energy scavenging device. Solar cells, or photo voltaic cells, convert energy from the incident radiation of sunlight, or another source of light, into electrical energy. The first patent on a solar cell was submitted in 1946 by Russell Oh. In 1954, Bell Laboratories scientists used doped silicon to make solar cells. Despite

Table 3.1 Power and energy capabilities of primary power sources, including energy scavenging devices. Energy is defined as the storage capacity of the power source, while power is defined as the rate at which the energy is supplied. *Solar cells power measured in μW/cm^2. Adapted from [56].

Type	Power (μW/cm^3)	Energy (J/cm^3)	Sources
Stored	34 - 90 per year	1,080 - 2,880	Batteries
Stored	1.6 - 3.2 per year	50 - 100	Super Capacitors
Converted	1×10^6	3,500	Heat Engines and Fuel Cells
Scavenged	15,000*	N/A	Solar (full-sunlight)
	10		Solar (indoors)
	40 for $\Delta T = 5^oC$		Thermal Gradient
	330		Human Power
	380		Air Flow
	17		Pressure Variation
	375		Vibrations

the maturity of photo voltaic technology, solar cells exhibit 10 - 25% efficiency and also require incident radiation [9],[10] which is highest in full-sunlight - a limiting environmental condition. The achievable power density is drastically reduced when a solar cell is used indoors, as shown in Table 3.1. Table 3.1 also outlines several available sources of electrical power and energy, as well as their average corresponding volumetric power and energy densities.

Many of the scavenged power densities in Table 3.1 were realized with both MEMS and meso-scale energy scavenging technologies. These technologies are able to generate electrical power in multiple environments by harvesting kinetic energy in the form of vibrations, human input, or additional environmental stimuli such as temperature gradients, airflow, and the flow of liquid.

3.2 Kinetic Energy Harvesting

The majority of current research in energy scavenging technologies seeks to utilize ambient kinetic energy. There are three main transduction methods for converting kinetic energy into electrical: piezoelectric, electromagnetic or inductive, and electrostatic or capacitive. These methods generally take advantage of environmental vibrations. However, humans can also provide a kinetic energy input into energy scavenging systems. Some examples of

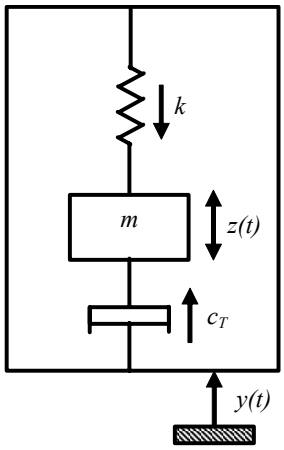

Figure 3.1 A spring-mass model of a linear inertial-based generator. Adapted from [6].

human-powered energy scavenging devices include piezoelectric shoe inserts which take advantage of the kinetic energy of the heel as it touches the ground during walking, and devices that take advantage of the force applied when pushing a button.

Vibrations occur in numerous environments ranging from bridges to buildings, industrial equipment to home appliances, and airplanes to the side of the road [7]. As a result, vibration scavenging has been widely, if not most, explored by micro electromechanical systems (MEMS) researchers. Typical vibration scavenging systems can be modeled as a spring mass system such as the one shown in Figure 3.1. A mass, m, is suspended form a spring with a stiffness coefficient of k. The damping coefficient is represented by c_T and includes parasitic losses as well as the energy extracted by the mechanical to electrical energy conversion mechanism. Typical vibration scavenging systems utilize a sinusoidal vibration represented by $y(t) = Y\sin(\omega t)$, where Y is the amplitude of the signal and ω represents the excitation frequency. The maximum energy can be harvested from such as system occurs if the excitation frequency, ω, is equal to the natural frequency, ω_n, of the spring-mass system where ω_n is given by equation (3.1). The energy transduction efficiency is drastically reduced at frequencies other than ω_n.

$$\omega_n = \sqrt{\frac{k}{m}} \tag{3.1}$$

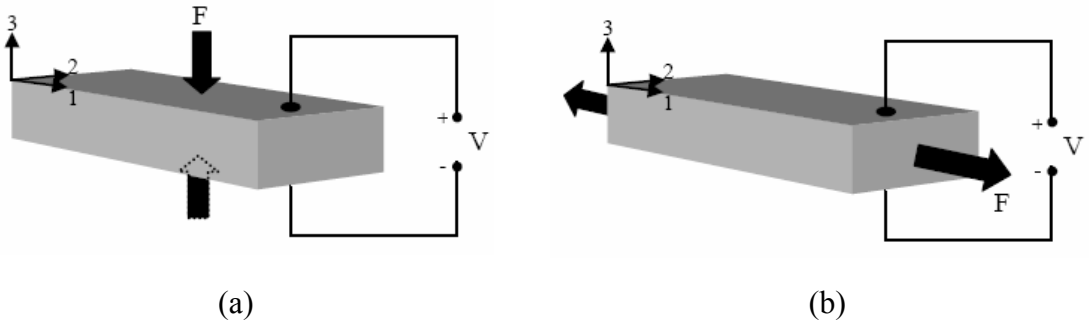

(a) (b)

Figure 3.2 Illustration of piezoelectric strains applied along the (a) longitudinal, or d_{33}, coefficient, and (b) transverse, or d_{31}, coefficient. Illustrations from Adapted from [10].

3.2.1 Piezoelectric Transduction

The piezoelectric effect was discovered in 1880 by Jacque and Pierre Curie. This method utilizes a compression or bending mechanical strain in an active material, which generates an electrical charge that is proportional to the mechanical strain. Conversely, piezoelectric materials exhibit mechanical strain in the presence on an electric field. The most commonly used piezoelectric materials include the piezo ceramic lead zirconate titanate (PZT), piezo polymer polyvinylidene fluoride (PVDF), thin film zinc oxide and single crystal quartz [7],[57]. Piezoelectric materials exhibit directional characteristics such that the mechanical and or electrical properties vary with the direction of the applied force and the orientation of the electrodes. Piezoelectric energy scavenging devices commonly employ one of two methods: (1) a compressive strain applied in a perpendicular orientation to electrodes along the longitudinal piezoelectric coefficient of the piezoelement, also known as the d_{33} coefficient, as shown in Figure 3.2(a), or (2) employ a transverse strain in a parallel orientation to electrodes along the transverse coefficient of the piezoelement, also referred to as the d_{31} coefficient, to change the length of the piezoelement, as shown in Figure 3.2(b).

The piezoelectric strain constant is a numerical way to define the piezoelectric activity of an active material by calculating the ratio of the strain developed in meters, to the applied field in volts. Conversely, the piezoelectric strain constant is also the ratio of the short circuit charge density in coulombs, to the applied stress in Newtons.

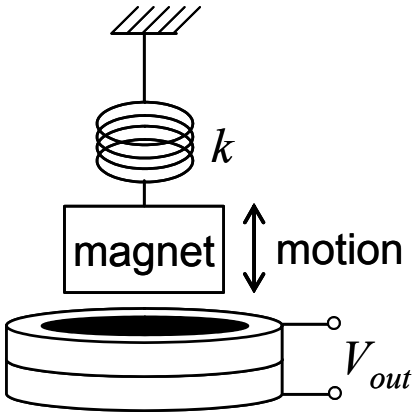

Figure 3.3 An illustration of an electromagnetic vibration energy harvester. Adapted from [57].

3.2.2 Electromagnetic Transduction

Electromagnetic or inductive conversion mechanisms take advantage of Faraday's Law, which states that any change in the magnetic environment of a coil of wire will cause a voltage, or electromotive force (*emf*), to be induced in the coil. The voltage is equal to the negative value of the product of the number of turns in a coil times the rate of change of the magnetic flux. This voltage can be dropped across a resistive load to obtain a current and is negative based on Lenz's Law, which states that the magnetic field of the generated current opposes the change in magnetic flux. The electromagnetic energy harvesting method utilizes Faraday's law by moving a coil through a stationary magnetic field or by moving a magnet through a stationary coil. The latter case is preferred so that the coil wires used to read V_{out} remain fixed while the magnet is attached to the end of a resonating cantilever structure with a spring constant k, as shown in Figure 3.3.

Electromagnetic transduction methods generally take advantage of vibration scavenging and result in small induced voltages. The induced voltages can be increased by increasing the number of turns in the coil, implementing a transformer to amplify the voltage; or increasing the intensity of the magnetic field or the area of the coil per equation (3.2).

$$emf = -N\frac{d\phi_B}{dt} \tag{3.2}$$

Electromotive force is a function of the number of turns in the coil, N, the change in change in the magnetic field, $d\Phi_B$ over time dt. Increasing the number of turns in the coil, using a transformer, or increasing the coil area results in an increase in device size, and thereby could reduce the total volumetric power density.

3.2.3 Electrostatic Transduction

The capacitive method, also known as the electrostatic method, utilizes a change in capacitance to either cause a voltage increase in a constant charge system, or a charge increase in a constant voltage system. The electrostatic energy scavenging method has been used to scavenge vibration energy from the environment and even from in vivo stimulus such as the vibrations of the ventricular wall [58].

The core unit of an electrostatic power generator is the variable capacitor. By fixing either the charge or the voltage, and then varying the capacitance, the unfixed element must alter itself to satisfy the basic equation (3.3) where Q is the charge in coulombs, C is the capacitance in Farads, and V is the voltage on the plates in volts. Although this method of transduction will be discussed in detail in Chapter V, a brief introduction is useful to explain other electrostatic transducer technology.

In a power generating mode, either the charge or voltage is held constant. The energy stored in the capacitor is given by equation (3.4). By substituting Q for CV in (3.4), the energy is also written as equation (3.5).

$$Q = CV \tag{3.3}$$

$$E = \frac{1}{2}CV^2 \tag{3.4}$$

$$E = \frac{1}{2}QV \tag{3.5}$$

A capacitance decrease forces the unfixed element of Q or V to increase. The lowering of the capacitance requires energy, and this energy is expressed in the increase in overall energy of the capacitor. In vibration scavenging devices, either the gap, d, between

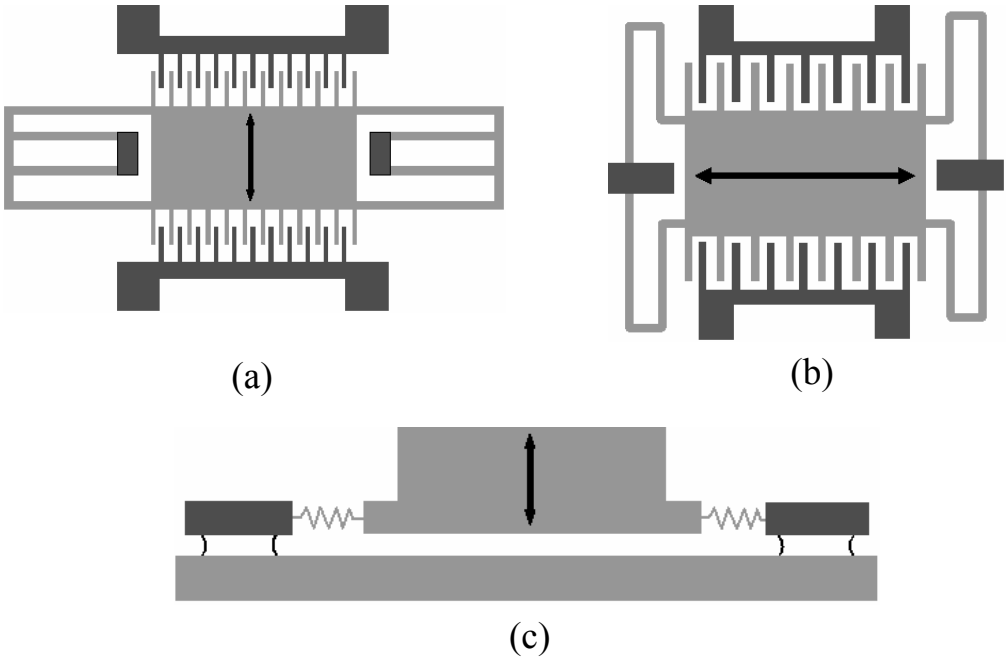

Figure 3.4 **Three types of electrostatic energy harvesting devices. (a) In-plane overlap varying electrostatic generator. Overlap area, *A*, is modified to change capacitance, *C*. (b) In-plane gap closing electrostatic generator. Electrode gap distance, *d*, is modified to change *C*. (c) Out-of-plane gap closing electrostatic generator. Gap distance, *d*, is modified to change *C*. Figures from [10].**

---

capacitor plates or the overlap area, A, of the plates is changed to modify the capacitance via equation (3.6), where ε_r is the relative dielectric permittivity of the insulating material between the plates.

$$C = \frac{\varepsilon_0 \varepsilon_r A}{d} \tag{3.6}$$

Roundy *et al* [59] classify three types of electrostatic generators that modify A or d from (3.6) during vibration. Schematics of these generators are shown in Figure 3.4. As an alternative, the work that is presented in this thesis introduces another type of electrostatic generator that relies on modifying ε_r of the insulation material between the plates, instead of geometric parameters [60].

In the constant charge implementation of electrostatic energy scavenging, the electrostatic force between the capacitor plates is given by equation (3.7) and then given as a function of voltage in equation (3.8), where all variables are as defined above. The energy

that is generated, ΔE, in the device for each change in capacitance, C, in the examples shown in Figure 3.4 is due to the work opposing the electrostatic force and is given by the expression in equation (3.9).

$$F = Q\frac{d}{\varepsilon_0 \varepsilon_r A} \tag{3.7}$$

$$F = \frac{\varepsilon_0 \varepsilon_r A V^2}{2d^2} \tag{3.8}$$

$$\Delta E = \frac{1}{2}C_f V_f^2 - \frac{1}{2}C_i V_i^2 \tag{3.9}$$

In the change in energy expression, C_f and V_f are the final values of capacitance and voltage at the some time and C_i and V_i are the initial capacitance and voltage values.

3.3 Other Energy Scavenging Technology

In addition to the use of ambient kinetic energy as the source for energy harvesting mechanism, developments have been made in devices that exploit other ambient conditions outside of movement via vibration or from the human body.

3.3.1 Radioisotope Generators

Radioactive sources have been combined with piezoelectric cantilevers to obtain energy scavenging devices that are able to achieve resonance in a cantilever without the requirement of an ambient vibration [61]. Duggirala *et al* [61] have obtained 16 μW of power from a silicon and a piezoelectric ceramic cantilever made of Lead Zirconate Titanate, or PZT, with 63Ni isotope. The radiated particles operate by electrostatically charging a conductive plate that is attached to the underside of a piezoelectric cantilever. The source of the particles is facing this plate. The electrostatic field between the plate and the source increases and causes the piezoelectric cantilever to become electrostatically attracted to the source of the radiated particles, thus, causing the cantilever to bend [7]. When the cantilever bends enough to make contact with the source, it dissipates the electric field, which eliminates the

electrostatic attraction between the plate and the source and causes the beam to be released quickly. The quick release of the beam causes it to vibrate at its natural frequency without an ambient vibration.

3.3.2 Thermoelectric Transduction

The principle of thermoelectric transduction takes advantage of a thermal gradient to generate electrical power. Thomas Seebeck is credited with discovering the Seebeck Effect, which sates that a thermal gradient between opposite ends of a conductive materials resulted in heat flow, which cause charge flow due to carrier diffusion. Thermoelectric generators consist of thermocouples, usually made of p-type and n-type semiconductors that are electrically connected in series and thermally connected in parallel. Stordeur and Stark designed a low power thermoelectric generator consisting of over 2000 thermocouples that required a temperature change of 20°C in order to extract 20 μW of power. The theoretical limit of this technology is found to be 60 μW at a $T = 20$°C and 4 V. The generated voltage, and consequently the generated power, is directly proportional to the temperature gradient and the Seebeck coefficient, which measures the voltage response due to a change in temperature, of the conductor used. As a consequence, thermoelectric generators face a limitation due to the limited availability of large ambient thermal gradients.

3.4 Comparison of Energy Scavenging Mechanisms and the State-of-the-Art

The need for energy scavenging technology has led many researchers and members of industry to attempt to find ways to make use of the ambient energy available in an environment to power remote devices. A summary of electrical energy scavenging methods, and their trade-offs is presented in Table 3.2. Because energy scavenging is not a one solution fits all field of research, compromises have to be made based on the application of the technology. For example, in areas that have full sunlight available, solar cells might be the best option. However, in areas that are closed off from incident light, other technologies need to be utilized, even though their power density may be significantly lower than that of solar cells. A comparison of the state-of-the-art in electrical energy scavenging devices is shown

Table 3.2 Advantages and disadvantages of typical electrical energy scavenging methods.

Technology	Advantages	Disadvantages
Solar	Most mature technology Uses CMOS High power density	Requires incident radiation (output power density plummets indoors) Low efficiency (10-25%)
Piezoelectric	Wide variety of materials Easy to micromachine High output voltage	Low electrical current Material fatigue Efficiency varies with material properties
Electromagnetic	Mature Wide variety of spring mass configurations Long life High output current for low input voltage	Fabrication is complex (magnets and coils difficult to micromachine) Requires high vibration frequency
Electrostatic	Utilizes well-known MEMS fabrication Scalable Energy density modified geometrically High output voltage High efficiency	Requires an initial voltage Parasitic components reduce efficiency
Radioactive	Long life	Use of radioactive materials has regulation and public acceptance limitations
Thermoelectric	Long life (material properties stay constant) No moving parts	Low efficiency Small thermal gradients occur naturally

in Figure 3.5 with the list of references used given in Table 3.3. Note that the power densities in Figure 3.5 are not normalized by the strength of the environmental stimuli. Some examples of the devices highlighted in the sections that follow.

3.4.1 Piezoelectric Generators

Roundy *et al* achieved 80 μW using a PZT cantilever with an attached cubic mass attached to the end [62]. The device was designed to resonate at 120 Hz. Sodano *et al* developed another cantilever system to obtain 11.9 μW [63]. Mide Technology Corporation has since commercialized a vibration energy scavenging device based on Sodano *et al's* work. In addition to the cantilever systems, interesting technology developed at MIT in 1998 utilized a stack of the piezoelectric material PVDF mounted in the heel of a shoe to extract 1300 μW of power from the bending movement during walking or running [64]. This work was improved upon by Shenck *et al* in 2001 to achieve 8400 μW from a PZT dimorph structure in the heel of a shoe [65].

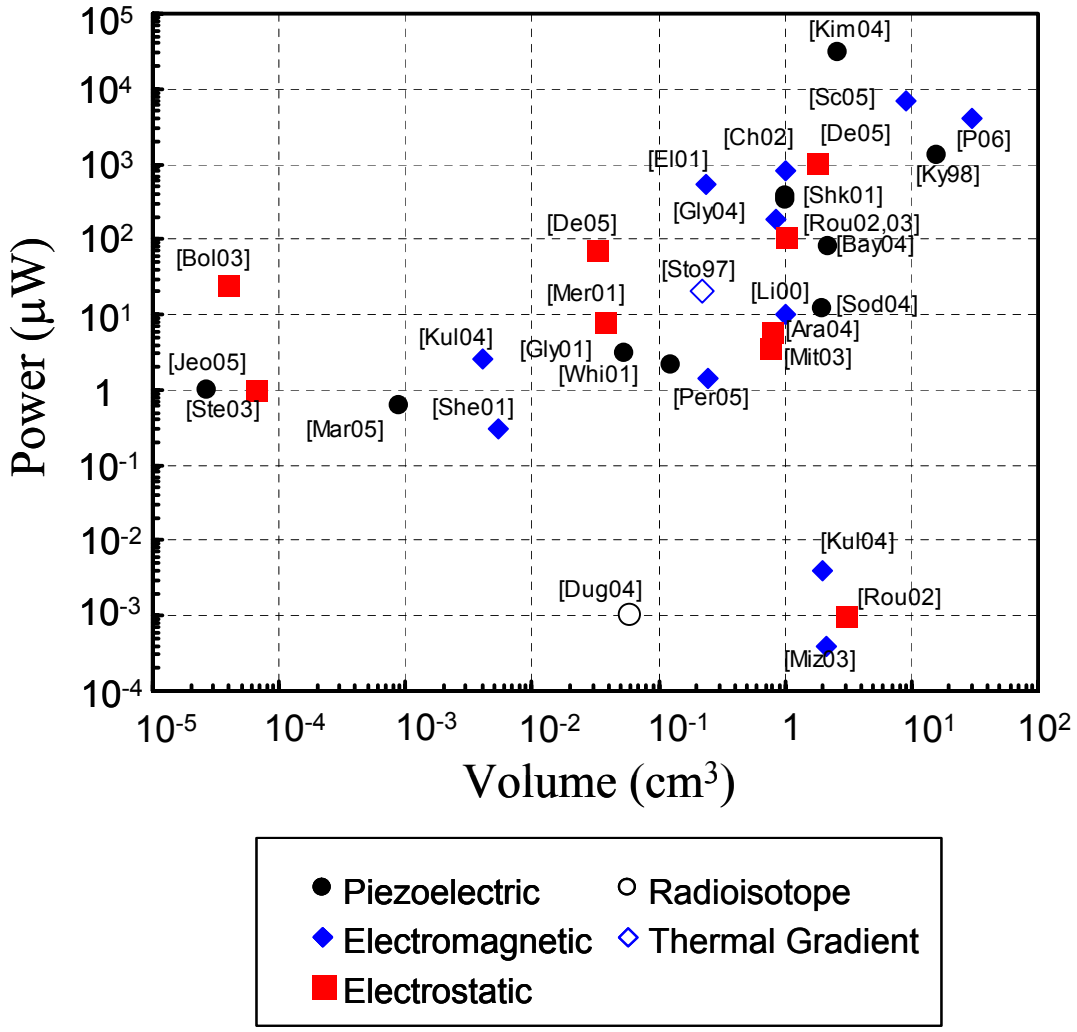

Figure 3.5 **A comparison of the power output versus the volumetric size of the state-of-the-art in energy scavenging technology. The volume of a given technology is usually listed in terms of 1 cubic centimeter. However, some technology power densities are given in terms of the specific device sizes. Note that these power densities are not normalized by the strength of the environmental stimuli. Refer to Table 3.3 for the reference number for each data point on this graph.**

Table 3.3 References used in the comparison plot in Figure 3.5 organized by type of energy scavenging mechanism (piezoelectric, electromagnetic, electrostatic, radioisotope, and thermal gradient).

Piezoelectric			**Electromagnetic**		
First Author	**Symbol**	**Reference**	**First Author**	**Symbol**	**Reference**
Kymissis	[Ky98]	[64]	Williams	[She01]	[66]
Roundy	[Rou03]	[62]	Mizuno	[Miz03]	[71]
Sodano	[Sod04]	[63]	Scherrer	[Sc05]	[72]
Bayrashev	[Bay04]	[73]	Ching	[Ch02]	[74]
Marzencki	[Mar05]	[75]	Perez-Rodriguez	[Per05]	[76]
Glynne-Jones	[Gly01]	[77]	Kulah	[Kul04]	[67]
Jeon	[Jeo05]	[78]	Glynne-Jones	[Gly04]	[79]
H. W. Kim	[Kim04]	[80]	El-Hami	[Elh01]	[81]
Shenck	[Shk01]	[65]	Li	[Li00]	[82]
			Perpertuum	[P06]	[68]
Electrostatic			**Radioisotope**		
First Author	**Symbol**	**Reference**	**First Author**	**Symbol**	**Reference**
Boland	[Bol03]	[83]	Duggirala	[Dug04]	[61]
Despesse	[De05]	[69]			
Arakawa	[Ara04]	[84]			
Roundy	[Rou03]	[10]	**Thermal Gradient**		
Mitcheson	[Mit03]	[70]	**First Author**	**Symbol**	**Reference**
Sterken	[Ste04]	[85]	Stordeur	[Sto97]	[4]
Meninger	[Mer01]	[93]			
Roundy	[Rou02]	[59]			

3.4.2 Electromagnetic Generators

Shearwood *et al* designed an electromagnetic transducer similar to the device shown in Figure 3.3 to generate 0.3 μW at an excitation frequency of 4.4 kHz [66]. The large frequencies required for electromagnetic transduction utilizing vibrations is seen as a limitation since most available vibrations are less than 100 Hz [67]. Kulah and Najafi sought to address the discrepancy between the high natural frequency of vibration energy scavenging devices and the available low frequencies in the environment. In 2004, they presented a frequency up-conversion electromagnetic transducer which used a low frequency as a stimulant to higher frequency resonance. A magnet was fabricated on a diaphragm above a

structure with coils [67]. The magnet on the diaphragm was excited at low frequencies and caused the coils to resonate at their natural frequency of 11 kHz using magnetic attraction. The calculated theoretical maximum of frequency up-conversion was listed as 2.5 μW, and is shown in Figure 3.5. However, the actual measured power density in a macroscale version of the proposed devices was 4 nW [67]. Electromagnetic generators have been commercialized by Perpetuum Limited, whose devices output 5 mW at acceleration values of 0.1 m s^{-2} [68].

3.4.3 Electrostatic Generators

Roundy's work in electrostatic generators utilized MEMS technology in configurations shown in Figure 3.4. Optimal power outputs of 100 $\mu W/cm^3$ are theoretically expected to occur in gap closing devices that utilize the smallest dielectric gaps [10]. Despesse *et al* presented an in-plane gap closing device that was designed to utilize vibrations at low frequencies to generate 1052 μW of power at 50 Hz [69]. Mitcheson *et al* developed a non-resonant electrostatic generator that consists of a silicon proof mass that moves only at the point of maximum acceleration in a vibration environment [70]. The three wafer device required a 100 V input to produce 3.7 μW of power. This device was capable of producing output voltages of 220 V; however, one limitation lies in the fact that the energy extraction circuitry must be able to handle such high voltages with low parasitic capacitance values.

CHAPTER IV

EVAPORATIVE-DRIVEN FLUID FLOW IN PLANTS

The transpiration actuation devices presented in Chapter II demonstrated that evaporation can be exploited to generate mechanical power. This thesis also explores the possible use of evaporation to generate electrical power. Many scenarios and environments exist where evaporation of water, and the corresponding formation of humidity gradients, allow for energy to be scavenged. Examples include the surface of the skin due to perspiration, near the surface of bodies of water, and the soil-air interface which is utilized to do work via transpiration by the vast majority of plants on earth. This thesis will explore the use of evaporation driven flow to generate electrical power in plant-like fluidic networks. Therefore, it is important to present an introduction to how plants use transpiration efficiently for their own purposes. This chapter will introduce the cohesion-tension mechanism used by plants to passively pump water through their vascular network, as well give an overview of the energy requirements of evaporation, and how plants maximize their hydraulic flow by obeying Murray's Law.

4.1 Transpiration in Plants and the Cohesion-Tension Theory

Vascular plants have evolved to take advantage of the process of transpiration in order to obtain an internal one-way fluidic transport network as well as cooling. Transpiration is evaporative-based pumping driven by some form of external energy source, which in the outdoors is almost exclusively solar energy. The process relies on the combined effects of both the evaporation of water from an air-water interface and the cohesive-adhesive properties of water. A plant's water requirements directly parallel the amount that is exchanged during transpiration. In fact, other water requirements for plant growth and photosynthesis pale in comparison to the ninety-five percent or more that is lost to transpiration through

the plant's leaves [86]. Water flow in plants is used to transport minerals throughout the plant, and the transpiration-driven flow of water from the roots to the leaves, provides a method of doing so at minimal energy cost [21].

The mechanism that drives the transpiration stream in plants is known as the cohesion-tension theory, or simply the cohesion theory, which explains that water in plant microvasculature is under tension generated at the leaves as water evaporates [22]. This driving force is a result of the automatic coupling between evaporation and the negative pressure achieved by capillary forces within plant vascular cell walls. The negative values of pressure indicate that the water in the plant system has a lower potential than the reference potential of water at sea level and standard temperature and pressure (zero bar) [97].

A plant minimizes its vascular maintenance costs by flowing water through high-conductance tubes of dead cells, known as xylem. Xylem is developed by programmed death of protoplast and a compression-resistant cell wall to avoid collapse by negative pressure within the capillaries [86]. Thus, the cost of transpiration is reduced to water-flow side-effects of the construction of the microvasculature networks, flow-induced water stress or negative apoplast pressure, and the layers of living tissues with hydrophilic cell walls that filter the water into the xylem from the soil [87]. As a result, plants allow transpiration to passively pump water through their microvasculature without expending much energy to actively pump the water themselves.

4.2 Energy and Rate of Evaporation

Simple calculations using accepted transpiration values show that the leaves of plants, aside from collecting energy for photosynthesis, collect several mW/cm^2 in the form of transpiration flow, a power density that would satisfy the power requirements of wireless sensor networks and is on the same magnitude as that of solar cells. Keep in mind, however, that the total volume of non-leaf plant mass is also required to collect and transport the evaporated water.

Modern microfabrication techniques allow for the production of microchannels of appropriate size to allow capillary action to become one of the dominant forces and to approach the scale at which the process of transpiration in plants can take place [92]. How-

ever, transpiration is a process with inherent losses. The movement of water in the micro-channels of a transpiration-based energy conversion system can do work. However, in order to produce flow, water molecules must be removed from a leaf-like evaporating area. Therefore, energy is used in order to evaporate each molecule of water.

4.2.1 Energy to Evaporate Water

In order to derive the energy required to evaporate a given weight of water, E_w, two actions must be taken into account. First, the given volume of water must be heated to 100°C, and then the latent heat of vaporization, $\Delta_v H$, must be applied to the volume of water. This can easily be calculated using equation (4.1), where c is the specific heat of water and is equal to 4.186 J, $\Delta_v H$ is the latent heat of vaporization of water and is equal to 2261 J/g, and T_w is the temperature of the volume of water to evaporate, 100 indicates the temperature in degrees Celsius to which the water has to be brought, and g_w is the weight of the water in grams. It is obvious from equation (4.1) that the energy required to evaporate a given amount of water can be reduced by increasing the operating temperature.

$$E_w = g_w[(100 - T_w)c + \Delta_v H] \tag{4.1}$$

4.2.2 Rate of Evaporation

The attempt to quantify the rate of evaporation of a fluid is the topic of much research [94],[95]. The most accurate descriptions of evaporation and condensation at a fluid surface are based on quantum theory. However, one theory has predicted accurate flow rates and is given by equation (4.2) [96],

$$Q_{evap} = 4RD_w(n_w - n_0) \tag{4.2}$$

where Q_{evap} is the rate of total evaporation, R is the radius of the water surface, D_w is the diffusion coefficient of water in air which is approximately 0.25 cm^2/s, n_w is the is the water vapor density at the surface of the water, and n_0 is the water vapor density of the back-ground environment [23].

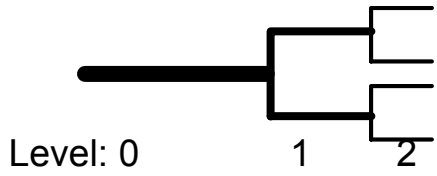

Figure 4.1 **An illustration of an example of a vascular network that obeys Murray's law. Level 0 represents the parent vessel. It should be noted that the vascular network need not be, and is often not, symmetric like the illustration above. In plants, there could be as many as 15 Level 2 channels. Further, there can be *N* number of levels, or bifurcations.**

4.3 Murray's Law for Optimal Vascular Networks

Plants have evolved a geometric model to maximize the hydraulic conductance to their networks. Plants maximize the hydraulic conductance per unit area of their microvasculature to obtain:

- minimal tissue investment for water transport
- longer path length for water transport and thus, larger plants
- less dynamic water stress
- potentially higher CO_2 diffusion rates since higher rates of transpiration can be tolerated without excessive stress [87].

Murray's Law defines the geometric algorithm that plant xylem networks obey in order to minimize hydraulic resistance and obtain maximum flow rates [87],[88], which states that the cube of the radius of a parent vessel equals the sum of the cubes of the radii of the daughters and is represented by equation (4.3).

$$r_0^{\,3} = r_1^{\,3} + r_2^{\,3} \tag{4.3}$$

For a symmetric bifurcation where the parent vessel is split into two equal radius channels, then it follows that equation (4.4) applies for two levels of bifurcation. Murray's Law is recursive and must hold no matter how many levels of bifurcation exist. An example of two levels of bifurcation is shown in Figure 4.1. Further, it must hold that the flow in the

parent channel is equal to the sum of the flow in the daughter channels, as given by equation (4.5) for two bifurcating levels.

$$r_0^{\,3} = 2r_1^{\,3} + 4r_2^{\,3} \tag{4.4}$$

$$f_0 = f_1 + f_2 \tag{4.5}$$

The fact that plants obey Murray's Law was not published until 2003 [88]. However, it was known for decades before that vasculature in mammals, specifically blood vessels, also obeys Murray's Law [90]. If this law is obeyed, an optimal relationship exists between the vessel radius and volumetric flow, average linear velocity of flow, velocity profile, vessel-wall shear stress, Reynolds number, and pressure gradient in individual vessels [90]. The Reynolds number, *Re*, is a dimensionless number that represents the ratio of inertial forces to viscous forces. A low Reynolds number indicates laminar flow, where viscous forces are dominant. A high Reynolds number indicates turbulent flow, where inertial forces are dominant and produce flow fluctuations. At the microscale, flow is generally laminar, which means that a pressure driven liquid flow can easily be modeled using linear elements like resistors, current sources for flow, and voltage sources for pressure [89]. By following Murray's Law, plants are able to maximize the surface area exposed to the air for transpiration.

CHAPTER V

TRANSPIRATION FOR ELECTRICAL ENERGY CONVERSION

An introduction and motivation for electrical energy scavenging was presented in Chapter IV along with a comparison of the various energy harvesting mechanisms. Chapter V will describe the modeling, design, and testing of a transpiration based energy conversion mechanism that can be used to harvest electrical power from evaporation. First, the electrostatic transduction model will be discussed in Section 5.1. In Section 5.2, a device overview will describe the transpiration based energy conversion mechanism. The fluidic lumped element model and device fabrication will be detailed in Section 5.3 and Section 5.4, respectively. The fluidic test results of the devices will be presented in Section 5.5. The largest section of this chapter, Section 5.6, will cover the electrical parameter models and results including an explanation of the voltage output conversion circuit that was implemented to measure an accumulation of output voltage on a storage capacitor. A theoretical upper bound for the power that can be scavenged from this technology is calculated in Section 5.7. The chapter ends with a summary of contributions.

5.1 Electrostatic Transduction Model

The capacitive method, also known as the electrostatic method, utilizes a change in capacitance to either cause a voltage increase in a constant charge system, or a charge increase in a constant voltage system. Capacitance, C, is given by (5.1), where ε_0 is the dielectric permittivity of free space and $\varepsilon_0 = 8.8541\times10^{-12}$ F/m, ε_r is the relative dielectric permittivity of the material between the capacitor plates, A is the product of the width, w, and length,

l, of the capacitor plates, and d is the distance between the plates. Thus, a change in capacitance can be achieved by modifying any of the geometric parameters of the capacitor such as w, l, and d, or by modifying the relative dielectric permittivity, ε_r, of the material between the capacitor electrodes.

$$C = \frac{\varepsilon_0 \varepsilon_r A}{d} \tag{5.1}$$

The electrostatic energy conversion method presented in this work utilizes a change in ε_r of the material between capacitor plates, by changing the actual material between the plates, to pump energy into a storage capacitor. The devices in this work maintain fixed capacitance geometries such as gap distance, d, and overlap area, A, but modify the dielectric permittivity by flowing an alternating set of two fluids with two different dielectric constants between fixed plates; thus, changing capacitance in the transition from one fluid to the other. This is in contrast with the capacitive method used by vibration harvesting devices, where the capacitor geometry is modified to change the capacitance.

There are two possible configurations of electrostatic scavenging devices: constant voltage or constant charge. The change in capacitance will force the non-constrained term to change in order to maintain the equality in equation (5.2) where Q is electrical charge, C is capacitance, and V is voltage. The stored energy of a capacitor, E, is expressed by equation (5.3).

$$Q = CV \tag{5.2}$$

$$E = \frac{1}{2} CV^2 \tag{5.3}$$

The general equation for power generation is shown in equation (5.4), where ΔE represents the gained energy, which is the difference between the final energy, E_f, and the initial energy, E_i.

$$\Delta E = E_f - E_i \tag{5.4}$$

The constant voltage and constant charge models are discussed in detail below.

5.1.1 Constant Voltage

The constant voltage implementation requires that the capacitance increase in order to harvest energy from the capacitance change. Following equation (5.4), the general equation for energy gained in the voltage constrained method, ΔE_{CV}, is show in equation (5.5), where the initial and final charges found on the capacitor are represented by Q_i and Q_f, respectively, and V is the voltage held constant over the capacitive change.

$$\Delta E_{CV} = \frac{1}{2} V(Q_f - Q_i) \tag{5.5}$$

By using equation (5.2) and noting that the variable capacitor can have a maximum value of C_{max} and minimum value of C_{min}, then the energy gained using the constant voltage model can be represented by equation (5.6).

$$\Delta E_{CV} = \frac{1}{2} V^2(C_{max} - C_{min}) \tag{5.6}$$

The maximum voltage that can be placed across a set of capacitor plates, V_{peak}, depends on gap distance, d, and the dielectric breakdown voltage, V_{BR}, of the insulation material between the capacitor plates. Since the distance between the plates is fixed in the devices presented in this work, V_{peak} is dependent on the product of the breakdown voltage of the dielectric and the thickness of the insulation material between the capacitor plates.

5.1.2 Constant Charge

The constant charge implementation requires that the capacitance decrease from the initial value in order to harvest energy from the capacitance change. Following equation (5.4), the general equation for energy gained in the charge constrained method, ΔE_{CC}, is show in equation (5.7), where the initial and final voltages found on the capacitor are represented by V_i and V_f, respectively, and Q is the charge that is conserved as the capacitance is changed.

$$\Delta E_{CC} = \frac{1}{2} Q(V_f - V_i) \tag{5.7}$$

By using equation (5.2) and noting that the variable capacitor can have a maximum value of C_{max} and minimum value of C_{min}, then the energy gained using the constant charge model can be represented by equation (5.8).

$$\Delta E_{CC} = \frac{1}{2}(C_{max} - C_{min})V_{max}V_{min} \tag{5.8}$$

In order to maintain the equality in equation (5.2), the maximum voltage, V_{max}, occurs when the capacitor is at its minimum capacitance, C_{min}, and the minimum voltage, V_{min}, occurs when the capacitor is at its maximum value, C_{max}.

5.1.3 Discussion of Model Selection

Both of the types of electrostatic converters discussed above require a separate voltage source to charge up the variable capacitor to an initial voltage. The voltage constrained method can result in a greater ΔE, which can easily be seen by replacing V in (5.6) with V_{max} and comparing the result with equation (5.8). However, the constant voltage method requires an additional voltage source to maintain a constant voltage, V_{max}, across the variable capacitor throughout the conversion process. For this reason, the constant charge implementation was selected. The voltage output conversion circuit will be discussed in detail in Section 5.6.6.

5.2 Device Overview

The energy conversion device in this chapter uses an evaporation-driven flow of two alternating fluids with different dielectrics to change the capacitance of a capacitor that consists of electrodes placed on the top and bottom of the fluidic channel. A flow diagram explaining the energy conversion mechanism is shown in Figure 5.1.

A plant-like microfluidic network is used to maximize the flow rate due to evaporation, Q_{evap}. Evaporation can be the result of changes multiple environmental conditions, specifically changes in: (1) percent relative humidity, RH%, (2) temperature, T, (3) pressure, p, (4) volume of gas in the environment, V_{gas}, (5) density of gas, ρ_{gas}, and (6) flow rate of gas, Q_{gas}. Therefore, an evaporation driven flow can occur as a result of a change in

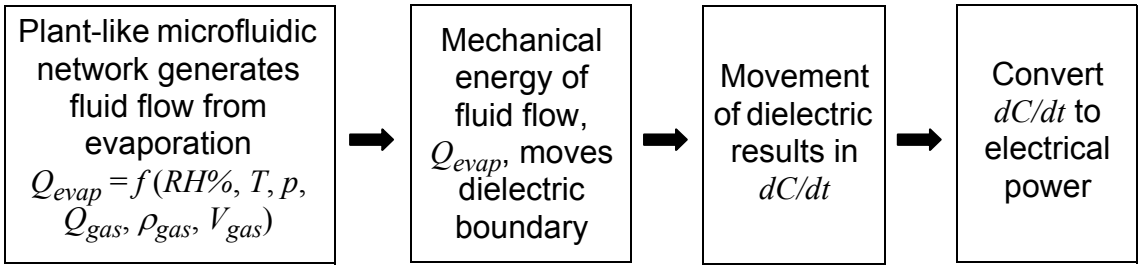

Figure 5.1 A flow chart explaining the transpiration mechanism to convert mechanical energy to electrical power.

one of the six parameters listed above. The mechanical energy of Q_{evap} moves a dielectric boundary to change the dielectric material between capacitive electrodes. The change in the dielectric material results in a change in capacitance over the period of time it takes for the boundary to traverse the capacitor electrode length, *dC/dt*. The change in capacitance is then converted to electrical power with a conversion circuit.

An illustration of the energy conversion device is shown in Figure 5.2(a) along with various micrograph insets of each device component Figure 5.2(b)-(d). The device consists of a parent channel that then branches out mimicking plant microvasculature and following Murray's Law to optimize hydraulic conductance as shown in Figure 5.2(c). Fixed capacitor plates are placed on the top and bottom of the channel and fluid is moved between them. As a bubble traverses between the electrodes Figure 5.2(b), it causes the capacitance to decrease. The voltage output conversion circuitry is shown in Figure 5.2(d) and will be discussed in detail in Section 5.6.6. However, the conversion circuit uses diodes to conduct during capacitance decrease (at the leading bubble edge), and block current during capacitance increase (at the trailing bubble edge). The flow of the fluid is driven by evaporation, much like in plants, and as a result, is passive.

In addition to the microvasculature network shown in Figure 5.2(c), porous materials were also used as evaporators by placing them at the channel outlet in lieu of the etched glass bifurcating design, as shown in Figure 5.3. The material properties of each evaporator used in testing the device is given in Table 5.1. The etched glass bifurcating design consisted of glass on three sides of the rectangular channel and parylene on the final side.

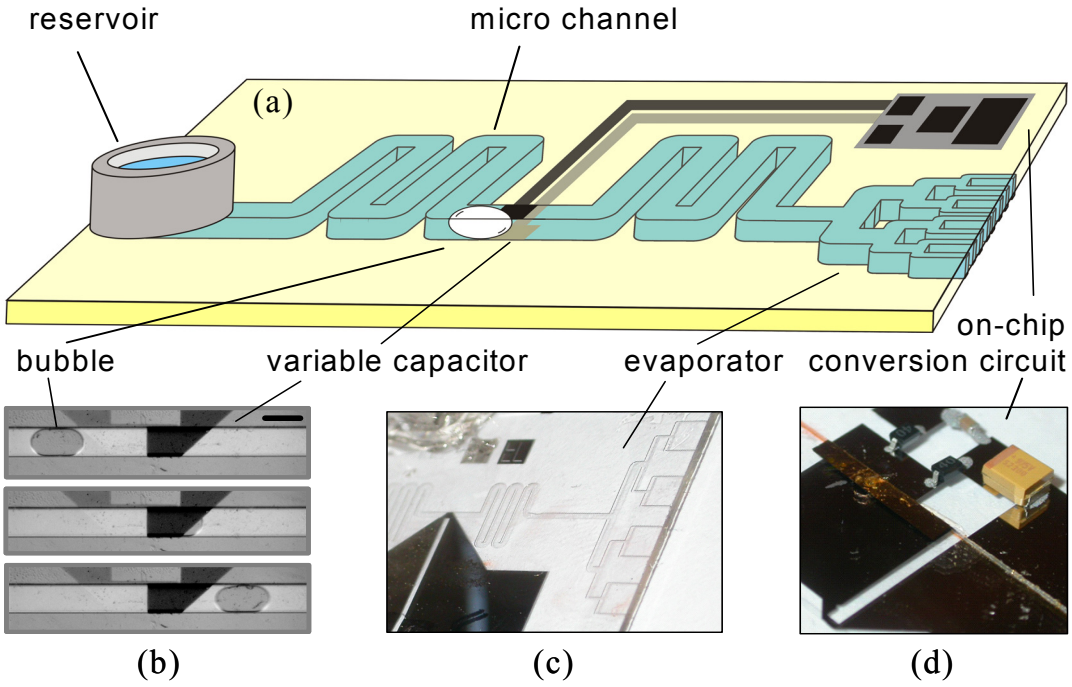

Figure 5.2 **An overview schematic of the transpiration for electrical energy conversion device with close-up insets: (a) overview illustration showing water reservoir and meandering micro channel to allow for a long bubble train, (b) bubble transiting between capacitor plates (scale bar = 500 µm), (c) evaporator branching network, (d) surface mount conversion circuit.**

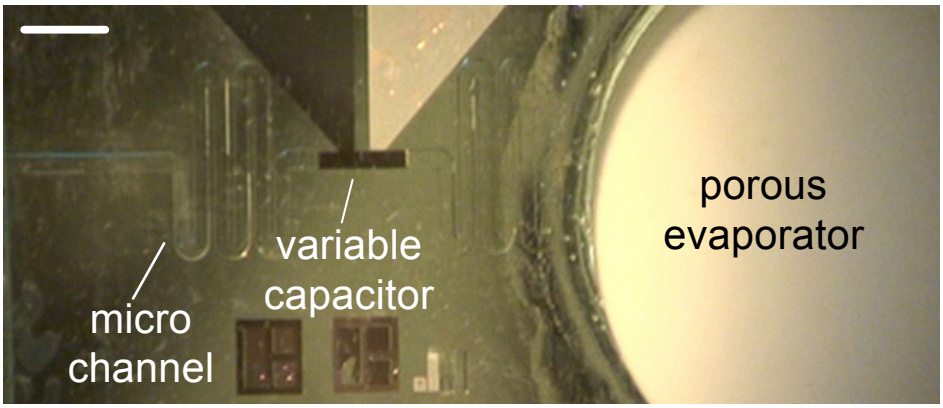

Figure 5.3 **Micrograph of transpiration based energy conversion device with a porous ceramic evaporator at the channel outlet (scale bar = 3 mm).**

Table 5.1 Properties of each evaporator material used in device testing.

Evaporator	Pore Diameter (μm)	Void Volume %	Evaporative Surface Area (m^2)	Manufacturer
3/4 Glass Channels 1/4 Parylene C	75	90	5.40×10^{-5}	Glass from Plan Optik AG Parylene C from SCS Coatings
High Fired Alumina	6	50	3.17×10^{-4}	Soil Moisture Equipment Corp.
High Fired Alumina	2.5	45	3.17×10^{-4}	Soil Moisture Equipment Corp.
Silica 99.99%	0.2	31	1.10×10^{-4}	Advanced Glass and Ceramics
Silica 99%	0.004	31	1.10×10^{-4}	Advanced Glass and Ceramics

5.3 Fluidic Model

In order to optimize channel dimensions for maximum hydraulic conductance, some fundamental fluid mechanics analysis must be carried out. The Reynolds number, *Re*, is a dimensionless number that represents the ratio of inertial forces to viscous forces. A low Reynolds number, indicates that viscous forces are dominant and that flow can be characterized as laminar. In equation (5.9), U is the average fluid velocity, D_h is the hydraulic diameter defined by equation (5.10), ρ is the fluid density, and η is the dynamic viscosity of the fluid in the channel. In equation (5.10), A and P are the cross-sectional area and cross-sectional perimeter, respectively.

$$Re = \frac{UD_h\rho}{\eta} \tag{5.9}$$

$$D_h = \frac{4A}{P} \tag{5.10}$$

At low Reynolds numbers of less than 2000, a pressure driven liquid flow can be modeled using linear elements such as resistors, current sources and voltage sources. Table 5.2 provides a summary of the lumped model analogy between linear elements of laminar fluidic flow to electrical elements. The hydraulic, or fluidic, resistance, R_{hyd}, can be determined by equation (5.11), where l is channel length, w is channel width, and h is channel height. If the channel width is much greater than the channel height, then equation (5.11) can be simplified to equation (5.12).

Table 5.2 Lumped model analogy between linear electrical to fluidic elements.

Fluidic Parameter, Symbol (Units)	Electrical Parameter, Symbol (Units)
Volumetric Flow Rate, Q_{flow} (m^3/s)	Current, I (A)
Pressure, p (Pa)	Voltage, V (V)
Hydraulic Resistance, R_{hyd} (Pa s/m^3)	Resistance, R (Ω)
Volume, V (m^3)	Charge, $Q_{electrical}$ (C)

$$R_{hyd} = 12\eta l\left\{h^3 w - \frac{192}{\pi^5}h^4 \sum_{m=0}^{\infty}(2m+1)^{-5}\tanh\left[\frac{(2m+1)\pi w}{2h}\right]\right\} \quad \textbf{(5.11)}$$

$$R_{hyd} = \frac{12\eta l}{h^3(w-0.6h)} \quad \textbf{(5.12)}$$

Using the analogy presented in Table 5.2 and Ohm's Law, the pressure drop, p, across a fluidic channel can be written as a function of the volumetric flow rate, Q_{flow}, and the hydraulic resistance, R_{hyd}, as shown in equation (5.13). The total hydraulic resistance of the fluidic channel, R_{total}, is the sum of the hydraulic resistance of the water and the hydraulic resistance of the air bubble that are in the fluidic channel shown in Figure 5.2(a), and is given by equation (5.14), where η_{air} is the dynamic viscosity of air, η_{water} is the dynamic viscosity of water, and l_{bubble} is the length of the air bubble. At room temperature, $\eta_{air} = 1.85\times10^{-5}$ Pa s and $\eta_{water} = 1\times10^{-3}$ Pa s.

$$p = Q_{flow}R_{hyd} \quad \textbf{(5.13)}$$

$$R_{total} = \frac{12[\eta_{air}l_{bubble} + \eta_{water}(l - l_{bubble})]}{h^3(w-0.6h)} \quad \textbf{(5.14)}$$

The hydraulic resistance for the porous materials, R_{porous}, is given by equation (5.15), where l_p is the length of the porous material, η is the dynamic viscosity of the fluid in the material, a is the pore radius, ψ is the porosity, and τ is the tortuosity. Tortuosity, τ, is an indicator of the curvature of the pores. For the materials used in this device, τ is assumed to be 1, which means that the pores consist of straight lines within the material.

$$R_{porous} = \frac{8\eta l_p \tau}{a^2 \psi w l_p} \quad \textbf{(5.15)}$$

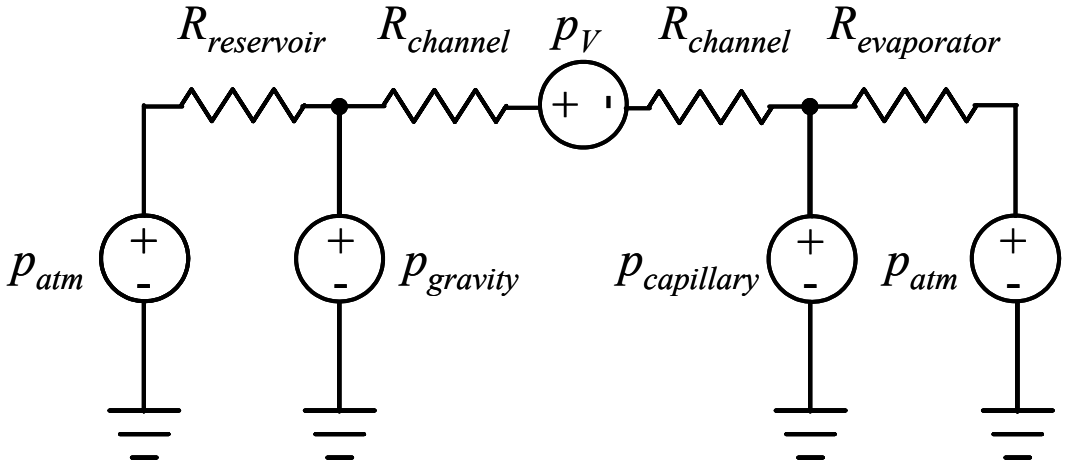

Figure 5.4 **A lumped model representation of the fluidic network of the transpiration based energy converter. The four sources of pressure shown are atmospheric (p_{atm}), gravitational ($p_{gravity}$), capillary ($p_{capillary}$), and electroosmotic pressure (p_V) due to the non-zero voltage, V_{in}, on the capacitor plates. At the microscale, the evaporative pressure drop is dominated by the $p_{capillary}$ (i.e. $p_{capillary} >> p_{atm}$ and $p_{gravity}$). It is known that p_V is also less than $p_{capillary}$ at channel radius values greater than 1 μm.**

Like in plants, the water movement due to evaporation in the transpiration based devices in this work is attributed due to a difference in the chemical potential of the water as opposed to an applied pressure since evaporation results in a passive flow of water [97]. This potential drop is dominated by the capillary pressure, $p_{capillary}$, due to the surface tension of the water menisci at the pores of the evaporator. The contributions to the water potential from atmospheric vapor, p_{atm}, and gravity at the reservoir, $p_{gravity}$, are much smaller than $p_{capillary}$. Thus, the net liquid flow is from the reservoir to the evaporator. The existence of a non-zero voltage on the capacitor plates generates an electroosmotic pressure, p_V, with the fluid flow at the water-air interface when a bubble enters between the capacitor electrodes, and counter to the fluid flow at the air-water interface when a bubble exits the capacitor electrodes. This phenomenon will be discussed and tested in Section 5.6.2. However, based on previous literature [98], it is known that pressure driven flow dominates electroosmotic flow for channels with radius values greater than 1 μm.

5.4 Device Fabrication

The devices in this work were microfabricated on two glass wafers that were bonded to each other with a polymer. Glass channels were used in order to best mimic the hydrophilic

properties of plant xylem. Microfabrication was used in order to achieve the same scale as plants such that capillary pressure dominates. The fabrication process is illustration in Figure 5.5.

Microchannels were patterned and etched isotropically using 1400 mL of Hydrofluoric acid, 600 mL of Nitric acid, and 2000 mL of DI H_2O to achieve 45 - 75 µm channel depths in glass wafers as shown in Figure 5.6. The glass wafers were purchased from Plan Optik AG. Capacitor plates were patterned on the bottom of the channels in wafer 1 shown in Figure 5.5 using an evaporated layer of titanium and platinum (300 Å Ti/ 1000 Å Pt). Similar Ti/Pt pads were patterned on wafer 2 shown on the right of Figure 5.5. That wafer was then diced and a layer of chrome and gold (200 Å Cr/ 2000 Å Au) was sputtered around the edge to create an electrical contact to the capacitor electrodes on the back side of the wafer. Then, wafer 2 was coated in 1.2 µm of Parylene C by SCS Coatings (Indianapolis, IN, USA) while the electrical contact on the back was protected and not coated with Parylene C. Holes were manually drilled into wafer 2 using a drill press for fluidic inter-

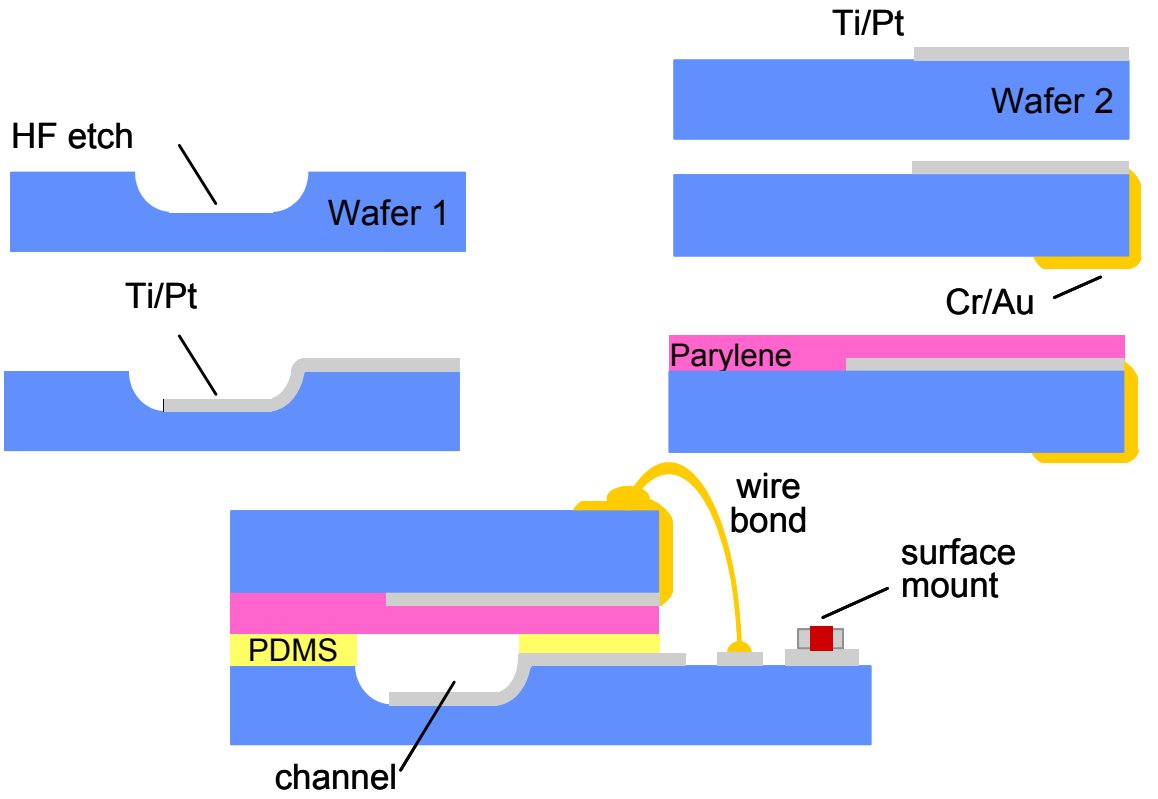

Figure 5.5 **An illustration of the fabrication process of the transpiration based energy conversion devices.**

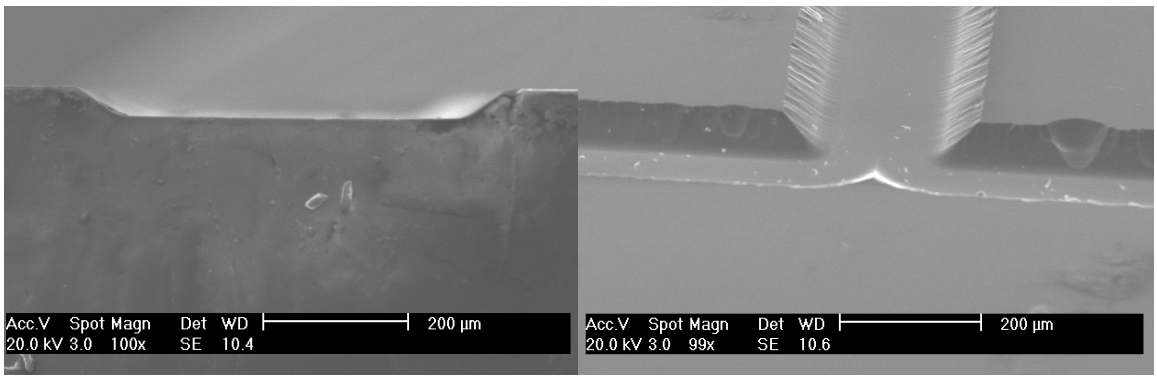

Figure 5.6 Electron micrographs of etched channels in glass wafers.

connection to reservoir (not shown). Using a stamping process, wafer 1 was coated with 3 µm of a 1:1 mixture of Sylgard 184 PDMS from Dow Corning (Midland, MI, USA) and 99.9% toluene on the areas surrounding the channel such that there was no PDMS in the channel. Both wafers were exposed to O_2 plasma (100 W, 150 mTorr, 1 min), aligned and bonded. The PDMS was cured overnight in an oven at 85 ^{o}C. Fluidic interconnects were attached. Surface mount components of the circuit were assembled soldered onto the Ti/Pt pads on wafer 1. Finally, the electrical contact of wafer 2 was wire-bonded to a pad on wafer 1.

The devices that used a porous material as the evaporator followed the same process outlined in Figure 5.5, with an additional step of gluing the porous material to the channel outlet using epoxy.

5.5 Evaporation-Driven Flow Fluidic Parameter Test Results

The fluidic performance of the transpiration based energy conversion device was characterized to best select which evaporator resulted in the fasted passive flow rate. Bubbles were loaded into the meandering channel and then evaporation driven flow was recorded using a Sony Handycam attached to a microscope with a 30 frame per second frame rate. The porous materials had to be pre-wetted with 1-2 mL of DI H_2O prior to testing. The percent relative humidity an the light source was recorded during every test. The relative humidity ranged from 27 - 45%. The light source focused on the device emitted a light intensity of 0.01 lx and was used to help focus the video image.

5.5.1 Volumetric Flow Rate

The volumetric flow rate was measured in liters per minute and then normalized to the evaporative surface area (m^2) given in Table 5.1. The evaporative surface area was different for each evaporator pore diameter due to either fabrication limitations, as was the case for the 75 μm pore diameter, or due to limitations of the geometries available from the manufacturer, as was the case for the 4 nm, 200 nm, 2.5 μm, and 6 μm pore diameters. As shown in Figure 5.7, the highest average volumetric flow rate was obtained by the evaporator with 6 μm pore diameters and the lowest was obtained by the evaporator with 4 nm pore diameters. The maximum measured volumetric flow rate for each pore diameter is also shown on the plot.

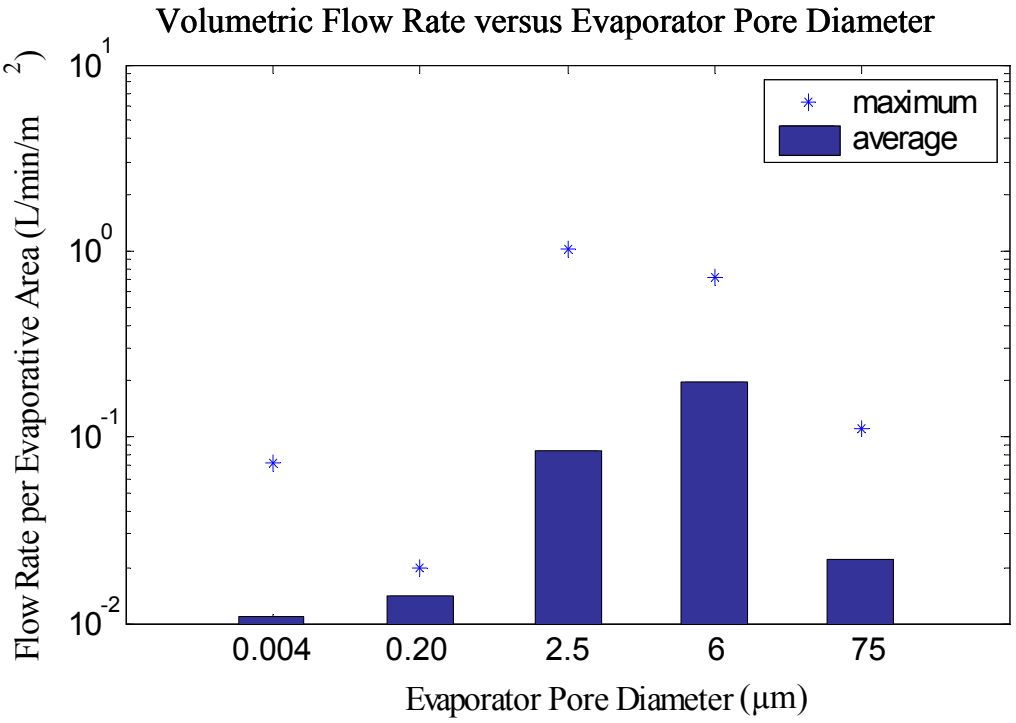

Figure 5.7 **The average and maximum evaporation-driven volumetric flow rate normalized by the evaporative surface area for each evaporator pore diameter. Devices with pore diameters of 4 nm and 200 nm had an area of 1.1×10^{-4} m^2, pore diameters of 2.5 μm and 6 μm had an area of 3.17×10^{-4} m^2, pore diameters of 75 μm had an area of 5.4×10^{-5} m^2. The devices with pore diameters of 75 μm were part of the branching network that obeyed Murray's Law and was etched in glass. Channel height = 45 μm and channel width = 500 μm.**

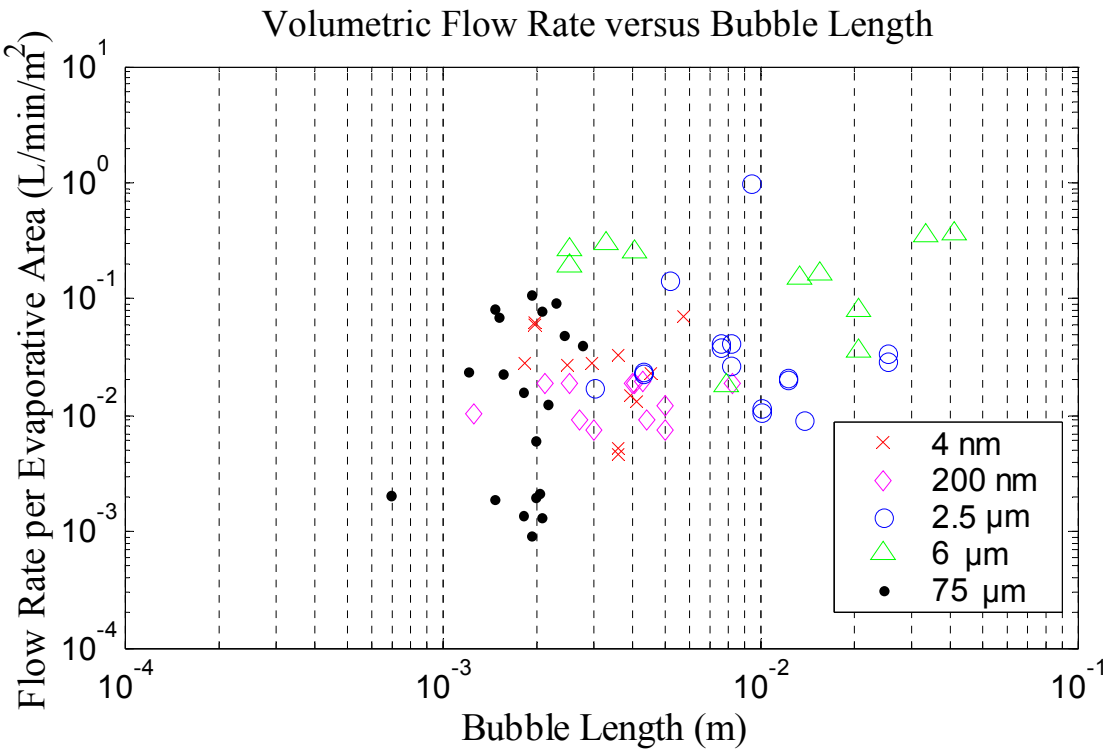

Figure 5.8 **The measured volumetric flow rate normalized by the evaporative surface area versus the bubble length for each evaporator pore diameter. The bubble length appears to have**

The volumetric flow rate was measured as a function of bubble length, as shown in Figure 5.8. Although the data shows variability, the length of the bubble was measured to have a negligible effect on the flow rate due to the fact that no trend was observed showing a dependence of flow rate on increasing bubble length. The variability, however, is attributed to the fact that evaporation is caused by variations in multiple environmental conditions such as changes in temperature, relative humidity, air flow, air volume, pressure, and air density. During testing, both temperature and relative humidity were recorded. Testing for a given evaporator was conducted in a time period such that relative humidity and temperature did not vary more than 10%. The main takeaway is that the bubbles used during device testing did not cause blockage of the porous materials or the branching network.

5.5.2 Velocity

The volumetric flow rate measured the rate at which a quantity of water evaporated. However, for the devices in this work, the velocity with which the fluid in the channel traversed

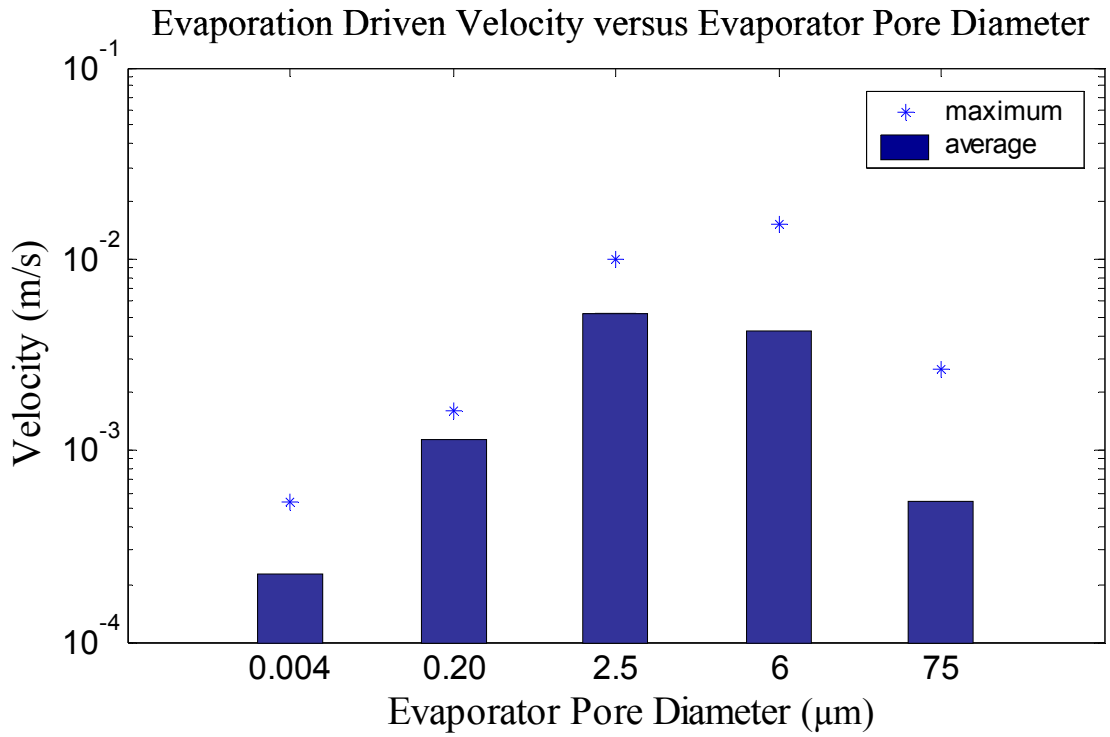

Figure 5.9 **The average and maximum evaporation-driven velocity for each evaporator pore diameter tested: 4 nm, 200 nm, 2.5 μm, 6 μm, and 75 μm. Channel height, h = 45 μm and channel width, w = 500 μm. Note that these measurements are not normalized by evaporative surface area to allow for comparison with the capacitor changes of individual devices.**

between the capacitor electrodes is a more important indicator of device performance due to the dependence of the output power on dC/dt. The faster that the bubbles are able to move, the faster they change the capacitance, and thus, the faster that energy is obtained over time, or the higher the power output. The velocity measurements are not normalized by evaporative surface area. The velocity versus the evaporative pore diameter is shown in Figure 5.9. The evaporators with 2.5 μm and 6 μm pore diameters exhibited the fastest velocities. The evaporator with the 6 μm diameter pores was selected for testing the electrical parameter tests because it exhibited the fastest flow velocity with a maximum value of 1.5×10^{-2} m/s and on average exhibited flow velocities of 4×10^{-3} m/s.

5.6 Electrical Parameter Models and Results

Following the fluidic parameter tests, devices were assembled such that the evaporator with 6 μm pore diameters was glued to the main channel outlet and the pores enhanced the rate

of evaporation. The main channel width was 500 μm and the height was 45 μm. The capacitor electrodes were 500 μm wide, to match the channel, and 3 mm long. For additional characterization, some devices were assembled with Upchurch fluidic connectors instead of a reservoir and the flow rate of the fluid was controlled by a syringe pump. This allowed for a comparison of the electrical results achieved with evaporation driven flow and faster flow rates set on the syringe pump.

5.6.1 Change in Capacitance

The capacitance of variable capacitor, C_{var}, was changed when an air bubble traversed between the electrodes, modifying the dielectric permittivity of the capacitor from that of water, to that of air, as shown in Figure 5.10(a) and (b). The change in capacitance was measured using an Hewlett Packard 4428A LCR meter with a measurement frequency of 1 MHz. At lower frequencies, noise distorted the signal. At 1 MHz, the change in capacitance, ΔC_{var}, was consistently measured to range from 8 - 10 pF for devices with electrode width = 500 μm, electrode length = 3 mm, channel height = 45 μm, and a 1.2 μm layer of parylene for insulation on one of the electrodes.

It is known that the measured change in capacitance has a dependence on measurement frequency, as shown in Figure 5.11(a), due to the fact that the relative dielectric permittivity of water varies nonlinearly with frequency, as shown in Figure 5.11(b). At lower measurement frequencies ($f < 100$ Hz), the relative dielectric permittivity of water has been measured to be approximately 6×10^5. In the previous section, the maximum evaporation driven fluidic velocity was measured to be 1.5×10^{-2} m/s, thus, the frequency with which the bubbles can traverse through the capacitor electrodes ($l = 3$ mm) is approximately 5 Hz and well into the low frequency and high relative dielectric permittivity of water regime.

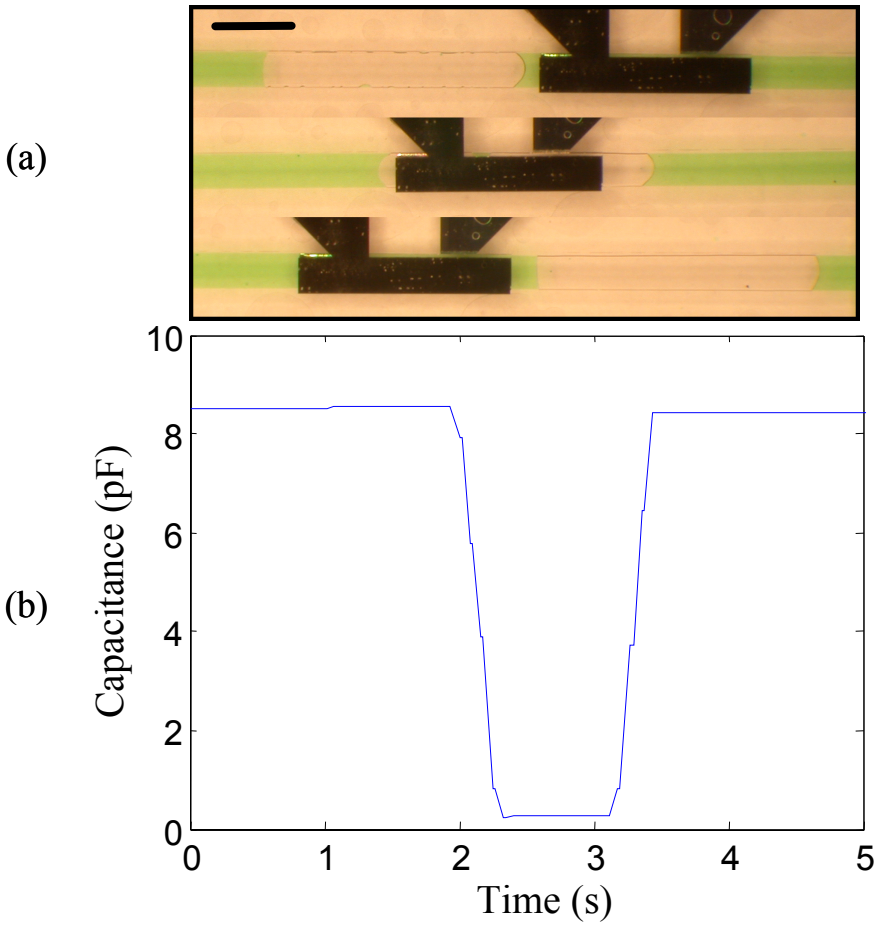

Figure 5.10 **Capacitance, C_{var}, versus Time. (a) A representative sequence of images showing a bubble moving between the capacitor plates. Food coloring was added to water for better visualization (Scale bar = 1 mm). (b) The capacitance for one bubble measured with an HP 4428A LCR meter at 1 MHz. ΔC_{var} from water to air as the bubble traversed the electrodes is 8.27 pF for channel height = 45 µm and parylene thickness of 1.2 µm. Parylene was used as a dielectric insulator to prevent electrolysis. Capacitance changes ranged from 8 – 10 pF for these devices.**

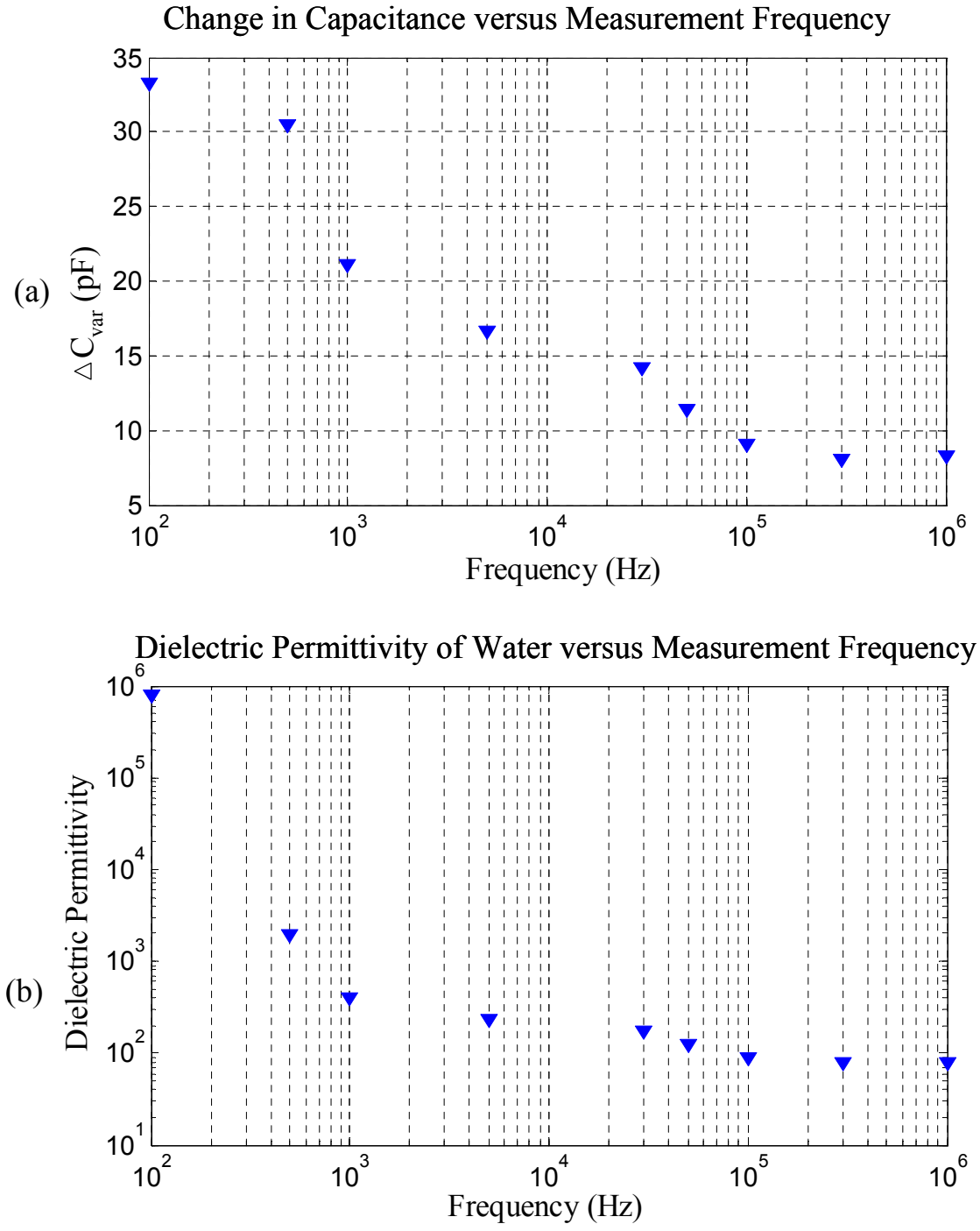

Figure 5.11 **Measured change in capacitance, ΔC_{var}, and relative dielectric permittivity of water increase as measurement frequency decreases (a) The measured change in capacitance, as the interface sweeps from water to air, versus measurement frequency. (b) The dielectric constant of water versus frequency using the measured change in capacitance.**

5.6.2 Electroosmotic Effect

On the microscale, secondary effects can contribute to the pressure in the transpiration based energy conversion system. As shown in Figure 5.4, one of the sources of pressure that should be considered as microfluidic devices are scaled down is electroosmotic pressure, p_V. This is pressure due to the non-zero voltage applied to the capacitor electrodes.

The electroosmotic pressure is calculated from the energy in capacitor with width, w, length, l, and gap distance, h, which corresponds to the channel height. This effect is important as the dielectric material between the capacitive electrodes is changed from water to air, and then air to water. For sake of generality, p_V is derived for a change between any two materials, material 1 and material 2, and is then calculated for the specific materials in this work.

The potential energy, U, of the capacitor shown in Figure 5.12 is given by equation (5.16) where w is the capacitor width, l is the capacitor length, h is the gap distance, ε_1 is the relative permittivity of material 1, ε_2 is the relative permittivity of material 1, ε_0 is the dielectric permittivity of free space, and x is the portion of the capacitor length taken up by material 2. The force, F_V, due to the voltage, V_{in}, on the capacitor, is calculated in equation (5.17). The pressure due to that voltage, p_V, is then found by taking the force over the cross-section area of the channel, as shown in equation (5.18).

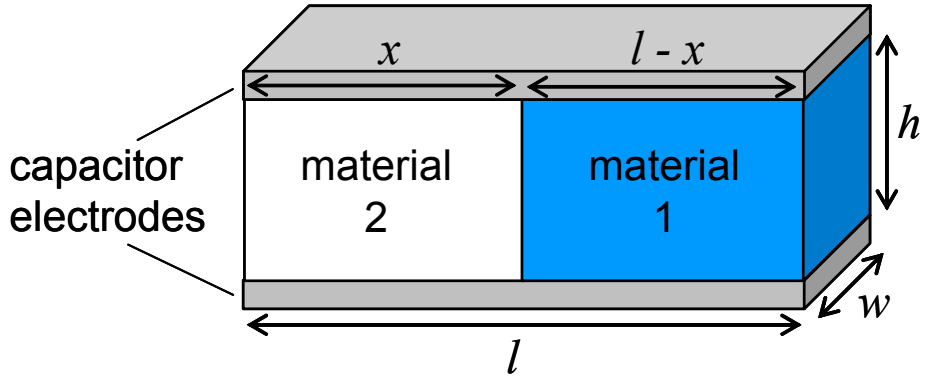

Figure 5.12 Illustration of a capacitor with two different materials, 1 and 2, as dielectrics. The capacitor area is the capacitor length, *l*, times the width, *w*. The gap distance between the capacitor electrodes corresponds with the channel height, *h*.

$$U = \frac{wV^2}{2h}\varepsilon_0(\varepsilon_2 x + \varepsilon_1(l-x)) \tag{5.16}$$

$$F = \frac{wV^2}{2h}\varepsilon_0(\varepsilon_2 - \varepsilon_1) \tag{5.17}$$

$$p_V = \frac{V^2}{2h^2}\varepsilon_0(\varepsilon_2 - \varepsilon_1) \tag{5.18}$$

From the derivation above, the theoretical pressure due to the voltage on the capacitor plates ranges from 0.17 Pa for V_{in} = 1 V up to approximately 70Pa for V_{in} = 20 V. The pressure is negative, or with the capillary pressure, when material 1 is water and material 2 is air (i.e. bubble entering capacitor). This pressure is positive, or against the negative capillary pressure, when material 1 is air and material 2 is water (i.e. bubble is exiting the capacitor). Based on this derivation, a bubble should theoretically enter the capacitor plates faster than it exits. This is a favorable effect because the energy conversion mechanism presented in this work relies on a fast *dC/dt* when going from water to air. It is important however, to compare p_V with the capillary pressure that is causing the evaporation driven flow. For the transpiration based energy conversion devices to work, the capillary pressure must be the dominant pressure. A quick calculation will show that for all of the evaporator geometries explored, the capillary pressure is in fact much greater than the electroosmotic pressure. For the evaporator with 6 μm pore diameters, the capillary pressure is at least 240X greater than p_V at V_{in} = 20 V. This agrees with previous literature [98], where it was shown that electroosmotic flow is not dominant at channel radii > 1 μm. The main channel in this work has a height of 45 μm.

The effect of the electroosmotic pressure was also experimentally tested by measuring the time it took for a bubble to enter the capacitor plates, fall time, and the amount of time it took for a bubble to exit the capacitor plates, rise time, as a function of the applied V_{in}. In order to isolate the voltage as the variable affecting fall and rise time, a syringe pump was used to ensure that the data was unaffected by variations in temperature, relative humidity and other factors that affect evaporative-driven flow. The experimental data confirm the theoretical assumption that the rise time will be greater than the fall time.

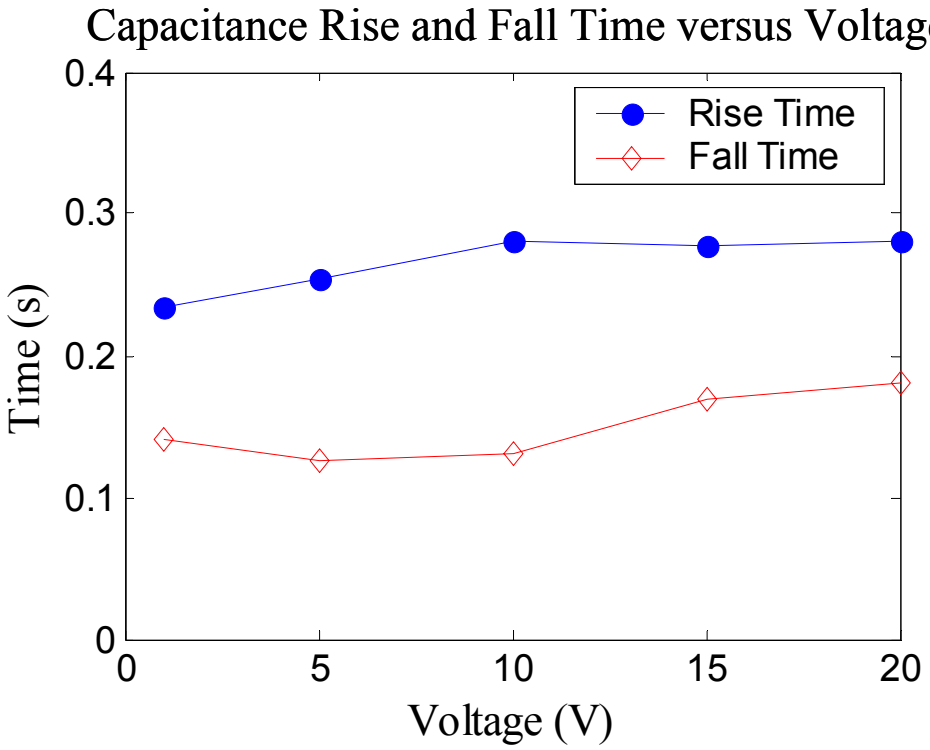

Figure 5.13 **Experimental study of the effect the non-zero voltage, V_{in}, on the flow rate. The effect of V_{in} was tested by measuring the time it took for the bubble to enter the capacitor plates as the dielectric was changed from water to air (Fall Time) and by measuring the time it took for the bubble to exit the capacitor plates as the dielectric was changed back from air to water (Rise Time). The capacitor dimensions are as follows: l = 3 mm, w = 500 µm, and h = 45 µm).**

Based on the measurements shown in Figure 5.13 and by using equation (5.13), the measured pressure drop across the capacitor due to V_{in} ranges from 110 Pa to 232 Pa.

5.6.3 Current and Charge Modeling

A way to predict the potential energy harvesting application of this device is to measure the current, and thus charge, that can be generated from each water to air interface. One way to do this is to use a charge redistribution circuit like the one shown in Figure 5.14. In this circuit, a storage capacitor, C_{store}, is placed in parallel with the variable capacitor, C_{var}, and both capacitors are pre charged to a voltage, V_{in}. The voltage is applied when $C_{var} = C_{max}$, or when there is only water between the capacitor electrodes, then C_{var} is changed as bub-

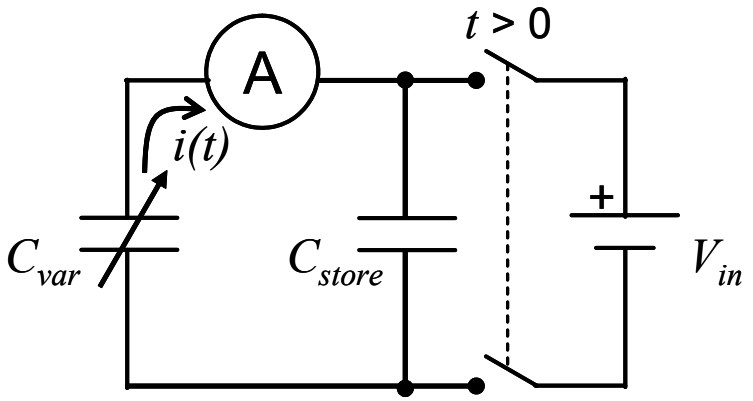

Figure 5.14 Charge redistribution circuit used to measure current and charge from each dielectric interface. The storage capacitor, C_{store}, and the variable capacitor in the transpiration based device, C_{var}, are pre charged with V_{in}. C_{var} is procreated when water is between the electrodes so that it equals its maximum value, C_{max}. The voltage source is disconnected at $t = 0$ s and then current is measured as bubbles traverse between the electrodes.

bles traverse between the electrodes. With each bubble entrance, charge, Q, should go from C_{var} to C_{store}. With each bubble exit, Q should go from C_{store} to C_{var}.

To measure the charge, a low impedance ammeter is used to monitor the current between C_{var} and C_{store}. The important parameters to measure are the peak current, average current, and the time that the current is non-zero at each dielectric interface. The charge, Q, is calculated by dividing the average current with the time in which it occurred. The peak current is used to predict the instantaneous power that can be obtained with each interface. From equations (5.19) to (5.21), and as expected, the current, $i(t)$, and charge, Q, from each change in capacitance as a bubble traverses between the electrodes is not a function of voltage, v, but only a function of the rate of change of capacitance, dC/dt, and the magnitude of the change in capacitance, ΔC_{var}.

$$i(t) = v\frac{dC}{dt} \tag{5.19}$$

$$dC = \frac{dQ}{dv} \tag{5.20}$$

$$i(t) = \frac{dQ}{dt} \tag{5.21}$$

The charge redistribution circuit was simulated for various ΔC_{var} values to show its effect on the peak current and charge that can be transferred with each water to air dielectric interface. The current at the ammeter is shown in Figure 5.15(a). It is positive as the dielectric in C_{var} is changed from C_{max} to C_{min} and Q is transferred to C_{store}, and it is negative as C_{var} is changed back from C_{min} to C_{max} and Q is returned to C_{var} from C_{store}. The duration of the change, Δt, of ΔC_{var}, from which $dC/dt = \Delta C_{var}/\Delta t$ was calculated, used in the simulations was the same as that measured from the evaporative flow rate of the evaporator with 6 μm pore diameters. The peak current and amount of charge increase with ΔC_{var}, as shown in Figure 5.15(b) and (c), respectively.

The charge redistribution circuit was simulated for various voltages, as shown in Figure 5.16 using the measured velocities for each evaporator and a calculated velocity for flow rates provided by a syringe pump. The velocities simulated were for the evaporators with pore diameters of 4 nm, 200 nm, 2.5 μm, and 6 μm. Also, syringe pump volumetric flow rates were also simulated for the values of 5 μL/min, 20 μL/min, 50 μL/min, and 100 μL/min. The peak current is shown in Figure 5.16(a) and the predicted charge transferred at each water to air interface is shown in Figure 5.16(b). The ΔC_{var} used in these simulations was 30 pF, which is close to the measured ΔC_{var} at low frequencies shown in Figure 5.11(a), although that value is on the low end of what is actually expected from each interface. It is obvious from these simulation results and as expected from equations (5.19) to (5.21), that the effect of voltage is only seen in the instantaneous power plot in Figure 5.16(c). The more important information that can be obtained from Figure 5.16 is the effect of the flow rate on the current, charge, and power that can be obtained from each water to air interface. Obviously, as the flow rate increases, so does the current, charge, and power. Further, one can see from these plots that the best evaporation-driven flow results should be obtained from the evaporator with 6 μm pore diameters.

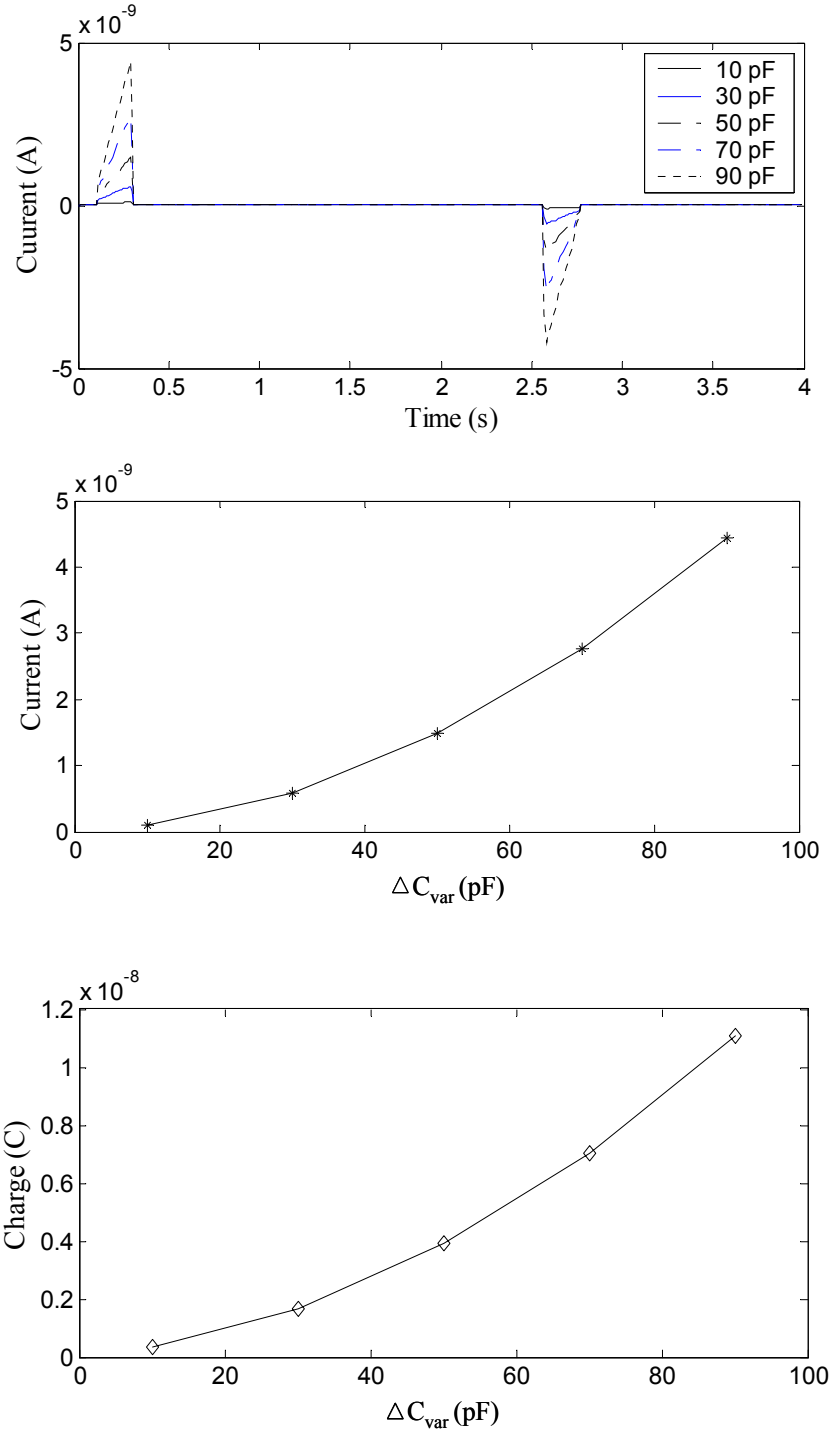

Figure 5.15 **Simulation results showing effect of an increased ΔC_{var} on device performance. (a) Current versus time for various changes in capacitance. (b) The peak current value versus the change in capacitance. (c) The charge transferred versus the change in capacitances. The duration of the change, Δt, of ΔC_{var}, from which $dC/dt = \Delta C_{var}/\Delta t$ was calculated, used in the simulations was the same as that measured from the evaporative flow rate of the evaporator with 6 µm pore diameters.**

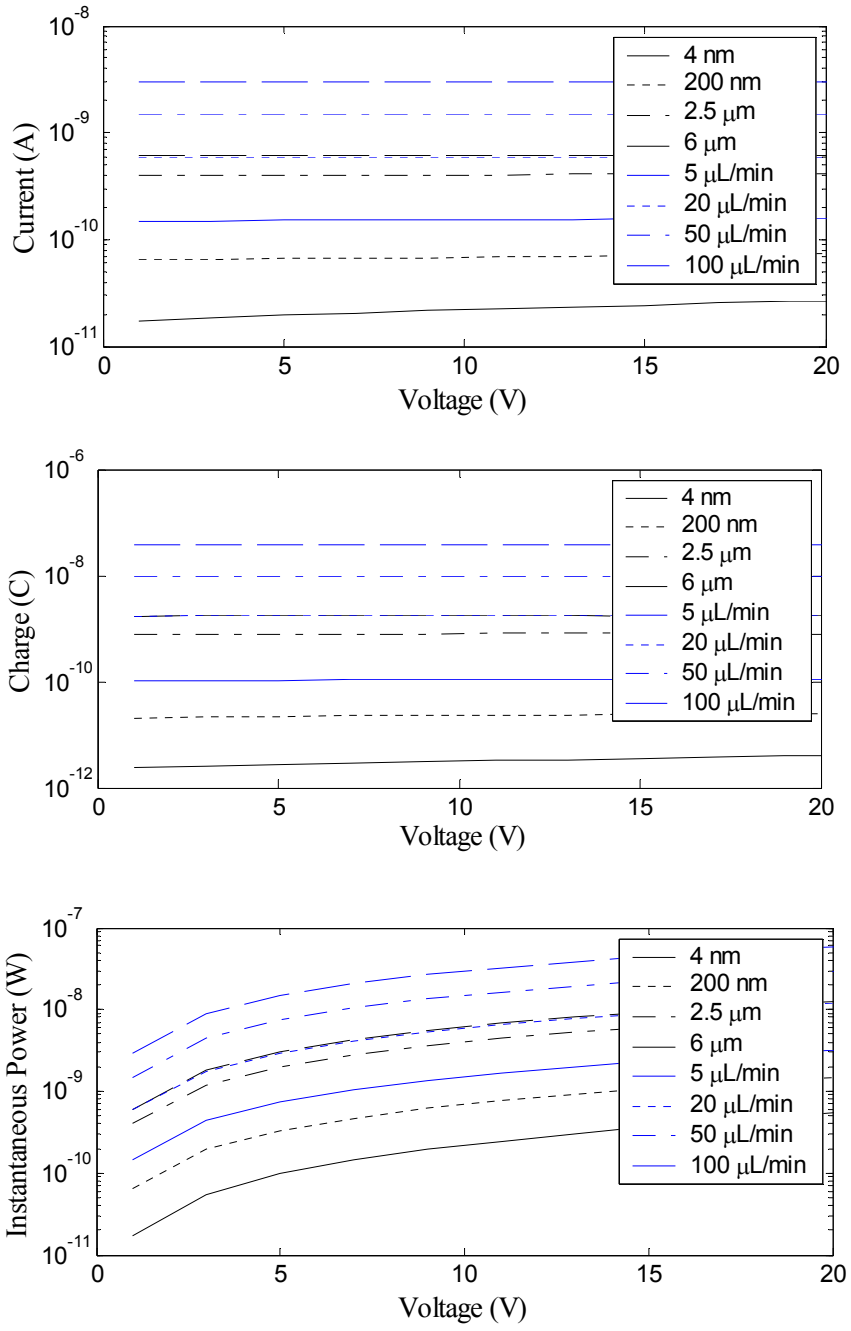

Figure 5.16 **Simulation results for (a) peak current, (b) charge, and (c) instantaneous power, versus voltage, V_{in}, using measured evaporation driven flow rates for each evaporator pore size and various syringe pump driven flow rates. Note that the lines in (c) do not appear linear even though $P = IV$ because of the semi log axes. The theoretical instantaneous power achieved by the flow rate from the evaporator with the 6 μm pore diameter ranges from 0.6 nW to 10 nW per water to air interface, depending on V_{in}.**

5.6.4 Current and Charge Test Results

The test set up used to measure the current and charge is shown in Figure 5.17. The results for the measured peak current, charge, and instantaneous power are shown in Figure 5.18(a), (b), and (c), respectively. The actual measurements were conducted for three different flow parameters. In the first, the transpiration based device was configured as shown in Figure 5.3 with the 6 μm pore diameter evaporator disk at the channel outlet. Bubbles were then evaporatively pulled between the capacitor electrodes, and the current was measured between C_{var} and C_{store}.

In the second and third flow parameters, the device was connected to a syringe pump at the inlet and the outlet was simply open with no evaporator. The syringe pump was used to compare the measured peak current, charge, and instantaneous power with the simulation predicted values from Figure 5.16 without the variability of relative humidity, temperature, and other factors that create inconsistency in evaporation-driven flow. This is to better quantify the loss in the charge redistribution test set-up.

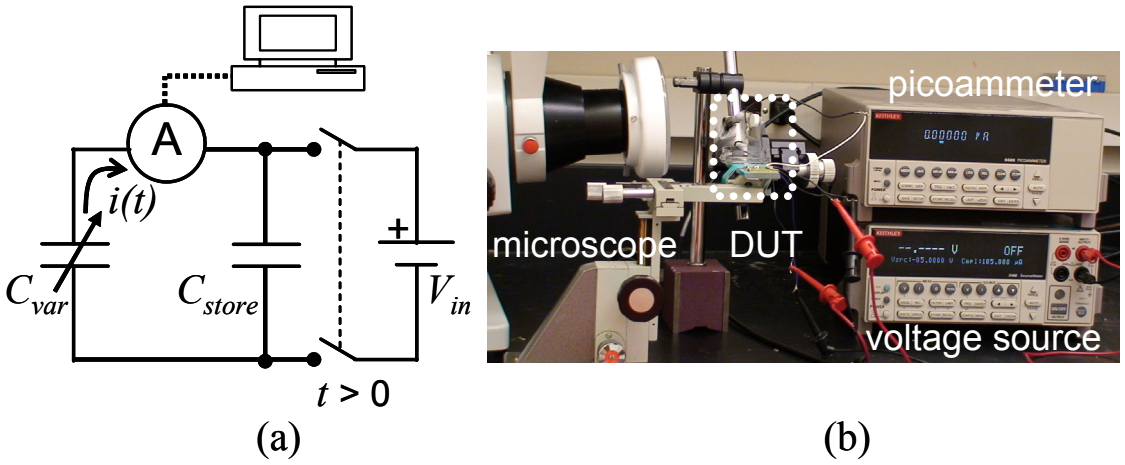

Figure 5.17 Charge redistribution circuit and test set up. (a) The storage capacitor, C_{store}, and the variable capacitor, C_{var}, are pre charged with V_{in} with a Keithley 2400 voltage source. This is done with no bubble between the electrodes so that C_{var} is at its maximum value. (b) The test set-up highlights the microscope with a camera that was used to record bubble motion and synchronize with the output of the Keithley 6485 picoammeter via a GPIB cable.

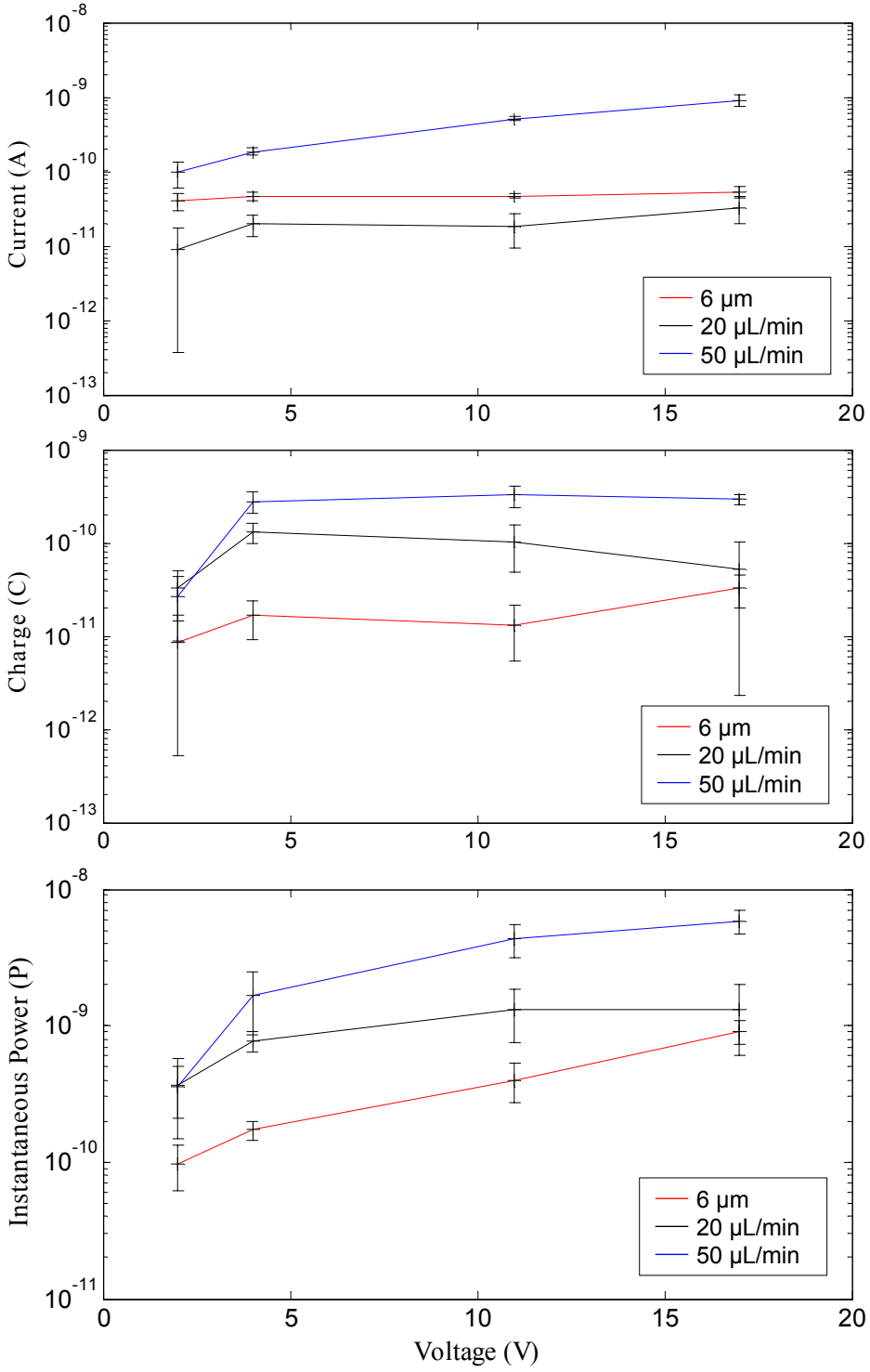

Figure 5.18 Measured results for (a) peak current, (b) charge, and (c) peak power, versus voltage. Three sources of fluid flow were used: (1) the evaporator with 6 µm pore diameters, (2) a syringe pump providing 20 µL/min flow rate, and (3) a syringe pump providing a 50 µL/min flow rate. Compare these data to the theoretical values shown in Figure 5.16.

The peak current obtained with the evaporation driven flow was on the order of 4×10^{-11} A, as shown in Figure 5.18, which is approximately an order of magnitude less than that predicted by simulation. This difference could be due to multiple effects. For example, leakage in the storage capacitor, as well as resistive loss through the interconnect wire and test cables. Further, the picoammeter sample rate is approximately 8 samples/sec. Therefore, if a peak current was reached at a time when the picoammeter was not sampling, then that data point could be missed. That sampling rate could also be the reason for the large standard deviation values shown in Figure 5.18.

In order to roughly quantify the loss from the test set-up, we can compare the syringe pump driven flow measured performance to that which was predicted by the simulation. The peak current for 50 μL/min flow was measured to be between 1×10^{-10} - 1×10^{-9} A and was predicted to be 1.5×10^{-9} A. The peak current for 20 μL/min flow was measured to be between 1×10^{-11} - 3×10^{-11}A and was predicted to be 0.6×10^{-10} A. The charge transferred using the 50 μL/min flow was measured to be between 3×10^{-11} - 3×10^{-10} C and was predicted to be 1×10^{-8} C. The charge transferred using the 20 μL/min flow was measured to be between 3×10^{-11} - 1×10^{-10} C and was predicted to be 1×10^{-9} C. From these comparisons, it is obvious that this method of measurement is lossy.

It is interesting to note the peak current values achieved by the evaporation driven flow were larger than those achieved with the 20 μL/min flow rate set by the syringe pump. However, in Figure 5.18(b), we can see that the charge transferred by the evaporation driven flow was less than that transferred by the syringe pump set at 20 μL/min. This is because the syringe pump provided a higher average current during the dielectric transition from water to air, but the evaporator achieved a higher peak current value in a shorter period of time. The actual charge transferred between C_{var} and C_{store} using the evaporation driven flow rate was measured to be on the order of 1×10^{-11} C, which is two orders of magnitude less than what was predicted by the simulation. In Figure 5.18(c), the measured instantaneous power is approximately an order of magnitude less than that predicted by the simulation since the instantaneous power is derived from the product of the peak current and the voltage.

The standard deviation lines show that there is a great deal of variability. Thus, the difference in performance between the evaporation driven flow and the syringe pump driven flow set to 20 μL/min, is not as easy to observe as the difference between either of those two and that of the syringe pump driven flow when set to 50 μL/min.

5.6.5 Scalability by Adding Capacitors

The feasibility of scaling on this technology must be demonstrated in order to project the theoretical limits of this mechanism of energy conversion. Thus, two variable capacitor devices were connected in parallel, as shown in Figure 5.19, and then placed in the same charge redistribution circuit used to measure current and charge. Both of the variable capacitors were connected to syringe pumps, and the ammeter readings were recovered versus time.

As can be seen in Figure 5.20, connecting multiple variable capacitors in parallel provides two benefits. The first being the increased refresh rate. At $t = 1$ s and $t = 1.5$ s, two positive spikes are shown indicating that a bubble entered C_{var1} at $t = 1$ s, and another entered C_{var2} at $t = 1.5$ s. Thus, instead of requiring very high flow rates, each device could spike at different times and simulate a faster flow rate. The second benefit is the additive effect. If the bubbles in both C_{var1} and C_{var2} enter between the capacitor electrodes at the same time, then the current measured would be double that of one bubble in one device. This can be seen at $t = 4$ s, where the peak current is approximately 2×10^{-9} A.

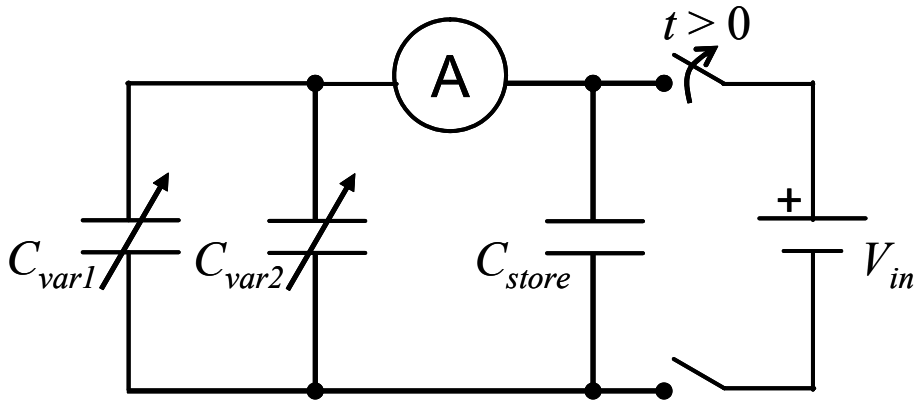

Figure 5.19 Schematic showing two variable capacitors were placed in parallel, C_{var1} and C_{var2}, and connected to C_{store} in the charge redistribution circuit. This was used to demonstrate the scalability by adding the output of multiple devices together.

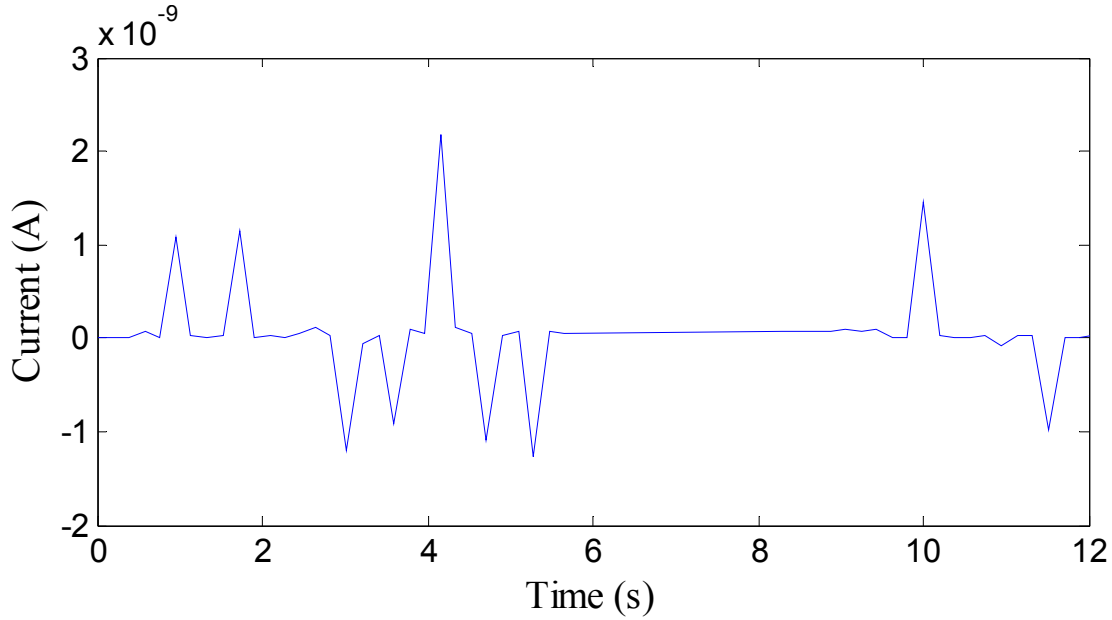

Figure 5.20 Current versus time showing scalability of energy conversion. Each device was connected to a syringe pump with PTFE tubing that was loaded with bubbles. The flow rate used was 100 µL/min. The data shows some points where bubbles were not synchronized, providing a peak current of approximately 1 nA, as well as points where bubbles went through C_{var1} and C_{var2} at the exact same time providing a higher current spike of approximately 2 nA. In addition to the additive property, connecting multiple variable capacitors together allows for a higher refresh rate, which is beneficial when implemented in the voltage output circuit.

5.6.6 Voltage Output Conversion Circuit Explanation

The true application of the presented transpiration based energy conversion mechanism is as an energy scavenging supply. Thus, a full conversion circuit that is capable of transducing the mechanical energy in the evaporation-driven fluid into electrical power is necessary. This circuit, as with any other, will include some inherent losses. However, if the change in capacitance, or ΔC_{var}, can be made large enough, or if the change can occur more quickly to maximize dC/dt, then the energy harvested from this mechanism can overcome the leakage in the circuit and potentially allow for the harvesting and storage of additional energy. The current state of the art energy harvesting mechanisms and devices were discussed in Chapter III. Similar voltage output conversion circuits used in the transpiration based work here have been used in vibration energy harvesting devices [58], although a slight modification is presented here in order to measure the output voltage with respect to

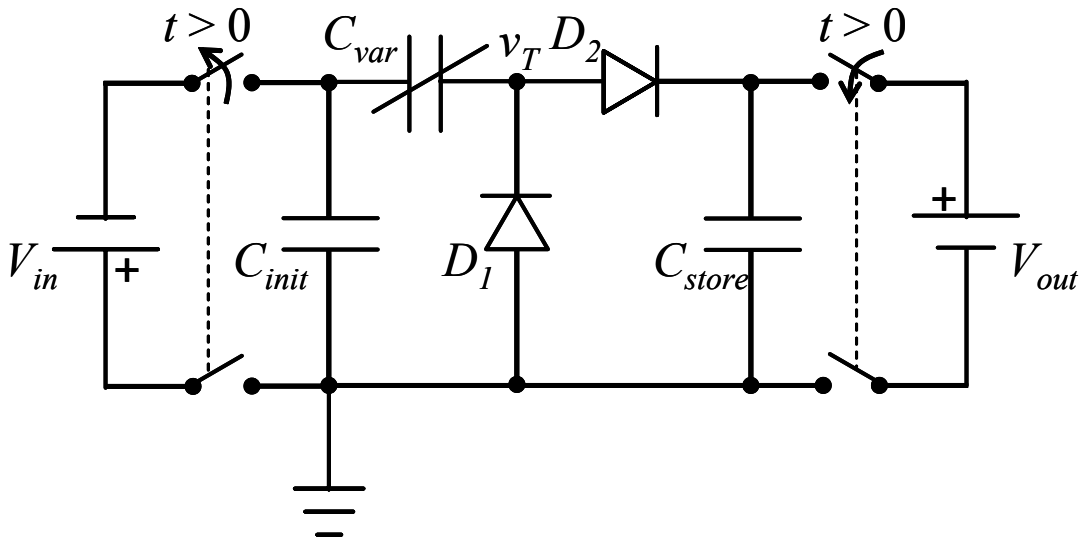

Figure 5.21 A schematic of the output voltage conversion circuit implemented in the transpiration based energy harvesting devices in this work. Similar circuits have been used in electrostatic vibration scavenging devices. The initial capacitor, C_{init}, and the variable capacitor, $C_{var} = C_{max}$, are pre charged to $-V_{in}$. The power supply is then disconnected at t = 0 s. This circuit follows the constant charge model. Thus, as C_{var} goes to C_{min} from C_{max}, the potential at v_T is increased and then D_2 conducts. That voltage is then stored on C_{store} and measured at V_{out}. Each negative ΔC_{var} results in a positive ΔV_{out}. D_1 prevents any positive ΔC_{var} changes from reducing the potential at v_T to below ground.

ground. Other well-known energy conversion circuits developed for electrostatic energy harvesting devices have been optimized for periodic signals from high frequency vibrations [93] and thus, include clocks for timing references. As previously shown in Figure 5.1, many environmental conditions affect the rate of evaporation, ranging from changes in temperature, relative humidity, atmospheric pressure, air flow, air volume, and others. As a result, periodic changes in capacitance are not be possible with a transpiration based energy harvesting mechanism.

A schematic of the voltage output circuit used in this work is shown in Figure 5.21. This circuit utilizes the constant charge model that was discussed in Section 5.1.2. The main advantage of this circuit is that it does not require a periodic signal. Instead, two diodes act to conduct and block based on potential changes at a T-node, v_T, caused by ΔC_{var}. There are three main modes of operation for the voltage output conversion circuit:

- Initial condition, $C_{var} = C_{max}$

- Voltage accumulation from $-\Delta C_{var}$ as C_{var} goes from C_{max} to C_{min} due to leading bubble edge
- No accumulation from $+\Delta C_{var}$ as C_{var} goes from C_{min} to C_{max} due to trailing bubble edge

Each of the conditions above are described in detail below.

5.6.6.1 At Initial Condition:

In the initial condition shown in Figure 5.22, the value of the variable capacitor is set to $C_{var} = C_{max}$ and both C_{var} and the initial capacitor, C_{init}, are charged to a negative initial voltage. The total energy in the system is given by (5.22) and (5.23) as the sum of the energy in each capacitor. The energy stored on a capacitor at any time is a function of the voltage across that capacitor at that time.

$$E_{Total} = E_{init} + E_{var} + E_{store} \tag{5.22}$$

$$E_{Total} = \frac{1}{2}C_{init}V_{in}^2 + \frac{1}{2}C_{var}V_{in}^2 + \frac{1}{2}C_{store}0^2 \tag{5.23}$$

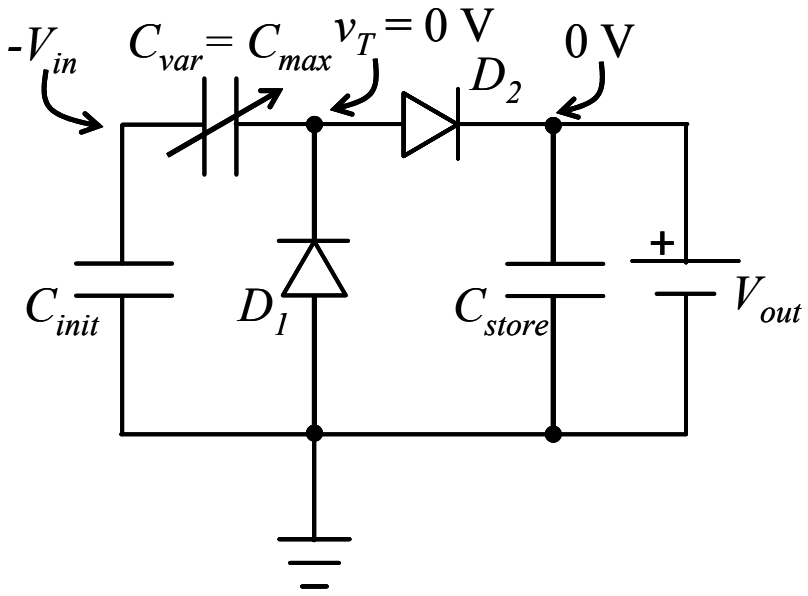

Figure 5.22 A schematic of the initial condition on the voltage output circuit after C_{init} and $C_{var} = C_{max}$ are pre charged to a negative voltage V_{in}. V_{out} starts at 0 V.

5.6.6.2 ΔC_{var} due to Leading Edge of Bubble ($\Delta C_{var} = C_{max}$ to C_{min})

When a bubble enters between the electrode plates of C_{var} and changes its value from C_{max} to C_{min}, then ΔC_{var} results in an increase of V_{out} on C_{store}. This effect is summarized in (5.24) to (5.26).

$$\frac{dC_{var}}{dt} < 0 \tag{5.24}$$

$$\frac{dv_T}{dt} > 0 \tag{5.25}$$

$$\Delta V_{out} > 0 \tag{5.26}$$

When dv_T/dt is greater than 0, then D_2 conducts current to C_{store} and D_1 blocks current. More fundamentally, the current caused by the change in variable capacitor, i, in Figure 5.23, is greater than 0 A, and electrons move towards the node between C_{init} and C_{var}, temporarily making it more negative.

If $i_{Cv}(t)$ is the current due to dC_{var}/dt, we can see that the variable capacitor acts like a variable current source that provides a positive current when the change in capacitance is negative and a negative current when the change in capacitance is positive. This relationship is expressed in equation (5.27), where V_{in} is the negative initial voltage on C_{var}.

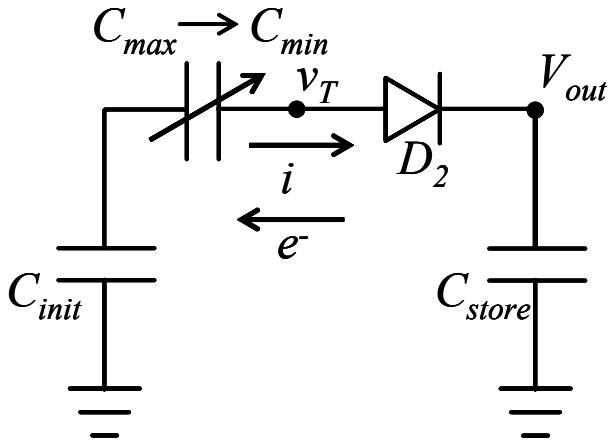

Figure 5.23 A schematic of the energy conversion step in which C_{max} goes to C_{min} and D_2 conducts the positive value of v_T to V_{out}. ΔV_{out} indicates the voltage harvested from the ΔC_{var}.

$$i_{Cv}(t) = V_{in}\left(\frac{dC_{var}}{dt}\right) \tag{5.27}$$

The positive current due to a decrease in the capacitance of C_{var} results in a positive charge that is conducted by D_2 to C_{store}. This charge is given by integrating the current over the time as shown in equation (5.28). The relationship between $i_{D2}(t)$ and $i_{Cv}(t)$ is discussed in detail in Section 5.6.6.4.

$$dq = \int i_{D2}(t)dt \tag{5.28}$$

The change in the output voltage on the storage capacitor, dv_s is given by equation (5.29). By substituting (5.27) in (5.29), the change in the output voltage is found to be a function of the current conducted by D_2 and the size of C_{store}, as given by equation (5.30)

$$dv_s = \frac{dq}{C_{store}} \tag{5.29}$$

$$dv_s(t) = \frac{\int i_{D2}(t)dt}{C_{store}} \tag{5.30}$$

5.6.6.3 ΔC_{var} due to Trailing Edge of Bubble ($\Delta C_{var} = C_{min}$ to C_{max})

When a bubble exits from the electrode plates of C_{var} and changes its value from C_{min} to C_{max}, there is no voltage accumulation on V_{out}. However, at this point, a full energy conversion cycle has occurred and the system has a net positive energy gain, ΔE_{cycle}, as summarized by equations (5.31) through (5.34).

$$\frac{dC}{dt} > 0 \tag{5.31}$$

$$\frac{dv_T}{dt} < 0 \tag{5.32}$$

$$E_{Total} = \frac{1}{2}C_{init}V_{in}^2 + \frac{1}{2}C_{var}V_{in}^2 + \frac{1}{2}C_{store}V_{out}^{\ 2} \quad \textbf{(5.33)}$$

$$\Delta E_{cycle} = \frac{1}{2}C_{store}V_{out}^{\ 2} \quad \textbf{(5.34)}$$

When dv_T/dt is less than 0, then D_1 conducts current to C_{store} and D_2 blocks current. More fundamentally, the current, i, in Figure 5.24, is less than 0 A, and electrons move towards v_T while the node between C_{init} and C_{var} returns to its original value of $-V_{in}$.

5.6.6.4 Current Through Charging Diode

In order to calculate dq in equation 5.28, we need to know the current through the charging diode, D_2. Using the basic equation for current through a diode, the current through D_2, i_{D2}, is given by equation (5.35), where I_S is the diode's saturation current, v_{D2} is the voltage across the diode as shown in Figure 5.25, V_T is the thermal voltage, and n is the emission coefficient. V_T is approximately 26 mV at room temperature, and n typically equals 1.

$$i_{D2}(t) = I_S \cdot e^{\frac{v_{D2}(t)}{nV_T}} \quad \textbf{(5.35)}$$

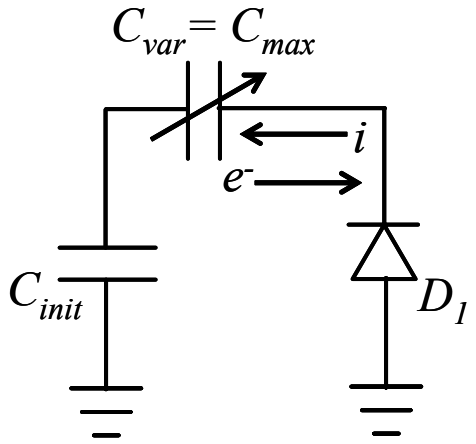

Figure 5.24 A schematic of the energy conversion step for the trailing bubble edge during which C_{var} goes to C_{max}.

The voltage across D_2 is given by equation (5.36), where $v_T(t)$ is the voltage on the T-node as show in Figure 5.22. From equations (5.35) and (5.36), one can easily see that as the voltage on the storage capacitor, $v_s(t)$ increases, then $i_{D2}(t)$ will decrease.

$$v_{D2}(t) = v_T(t) - v_s(t) \tag{5.36}$$

The excess current from the change in C_{var} ends up going through a parasitic resistor to ground, R_{p1}, as shown the schematic in Figure 5.25. This is easily seen by monitoring the voltage on the T-node, v_T, as given by equation (5.37), where i_{Rp1} is the current through the parasitic resistor, R_{p1}.

$$v_T(t) = [i_{Cv}(t) - i_{D2}(t)]R_{p1} = i_{Rp1}(t)R_{p1} \tag{5.37}$$

From equations (5.35) - (5.37), one can see that if the voltage on the storage capacitor, $v_s(t)$, is small then $i_{D2}(t) = i_{Cv}(t)$, meaning that all of the charge, dq, from dC_{var}/dt is conducted to C_{store}. In an energy harvesting system that uses multiple ΔC_{var} instances, the current through D_2, $i_{D2}(t)$, caused by the first ΔC_{var} is approximately equal to $i_{Cv}(t)$. After many ΔC_{var} instances, or many energy harvesting cycles, where enough charge has built up on C_{store} and $v_s(t)$ is high, then $i_{D2}(t)$ is expected to approach 0 A, and $i_{Cv}(t) = i_{Rp1}(t)$. This simply shows that as charge builds up on C_{store}, D_2 will decrease the amount of dq that it transfers with each ΔC_{var}, and thus, d$v_s(t)$ decreases with each ΔC_{var}. The amount of time that it takes to charge up C_{store} enough to decrease $i_{D2}(t)$ depends on the size of C_{store}. An illustrated example of the V_{out} and i_{D2} versus time is given for a small capacitor and a big capacitor in Figure 5.26(a) and (b), respectively.

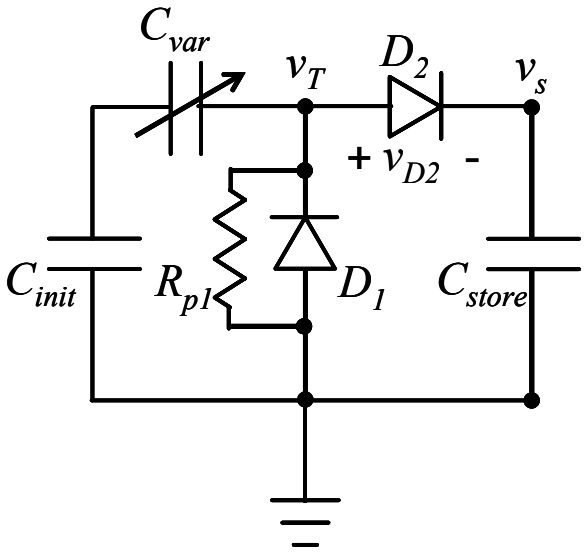

Figure 5.25 **A schematic of the voltage output circuit giving a closer look at charging diode, D_2, and includes parasitic resistance R_{p1}.**

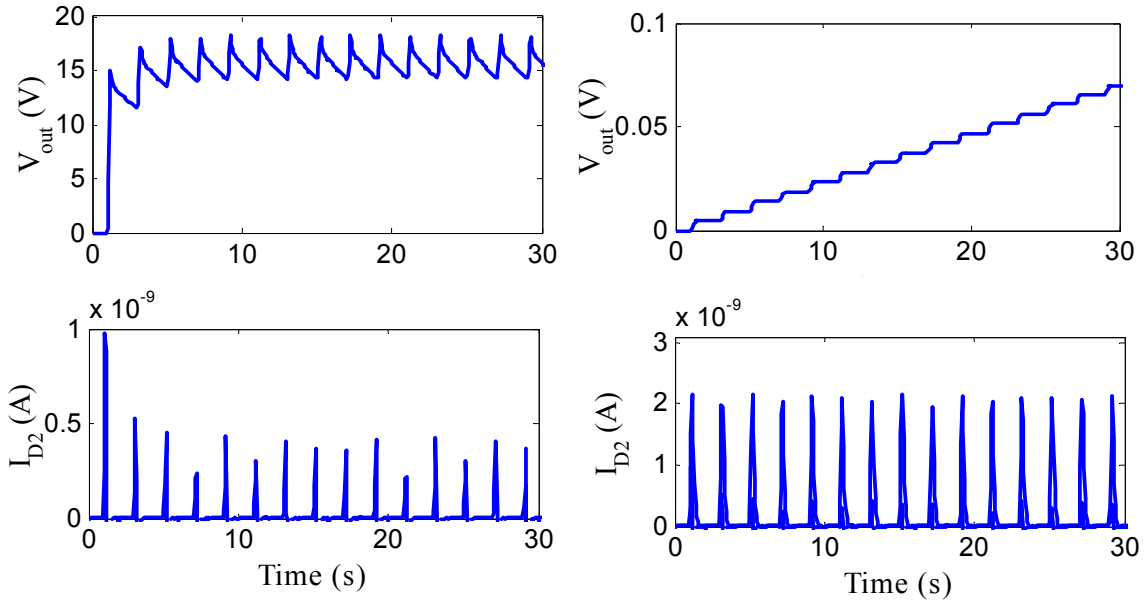

Figure 5.26 **V_{out} and D_2 current versus time for two C_{store} values for multiple ΔC_{var} instances (a) Small C_{store} (b) Large C_{store}. Note the difference in scale on the V_{out} versus Time plots. The smaller capacitor charges up much more quickly than the larger capacitor and thus D_2 conducts less current over time for the smaller capacitor. However, the smaller capacitor discharges much more quickly (note the decrease of V_{out} in between ΔC_{var} instances).**

5.6.6.5 Determining the Proper Size of C_{store}

As illustrated by the graphs in Figure 5.26 and the discussion in Section 5.6.6.4, the size of C_{store} will affect the output voltage versus time. The first thing that is important to note is that any size C_{store}, given sufficient ΔC_{var} instances, will charge up to a V_{max} determined by the ratio of C_{max} to C_{min} times the initial voltage, V_{in}. However, different sizes of C_{store} take different times to charge up to V_{max}, and similarly to discharge, based the time constant, $\tau = RC$. The time it takes for a voltage across a capacitor to discharge based on a scalar multiple of τ is shown in Figure 5.27.

The selection of the proper size for C_{store} is dependent upon the application. From the discussion in Section 5.6.6.4, we know that as the size of C_{store} decreases, *dv(t)* also decreases as V_{out} approaches V_{max}. Further, the refresh rate of ΔC_{var}, or the number of ΔC_{var} instances, has to go up to counter the effect of the faster discharge. For the purposes of the measurements presented in this work, it was imperative that the capacitor not discharge quickly. Therefore, a large C_{store} was selected.

Recall from the discussion in Section 5.6.6.1 that the energy is dependent upon the size of the capacitor. Therefore, once the voltage across C_{store} is at V_{max}, the energy of the larger capacitor will be larger than that of the smaller capacitor, as shown by (5.38).

$$\left[E_{BigCstore} = \frac{1}{2} C_{Large} V_{max}^{\ 2}\right] \gg \left[E_{SmallCstore} = \frac{1}{2} C_{Small} V_{max}^{\ 2}\right] \tag{5.38}$$

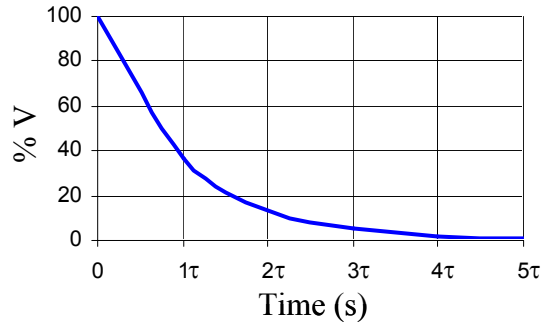

Figure 5.27 Percent of *V* on a capacitor versus the time it takes to discharge as a scalar multiple of the *RC* time constant, τ.

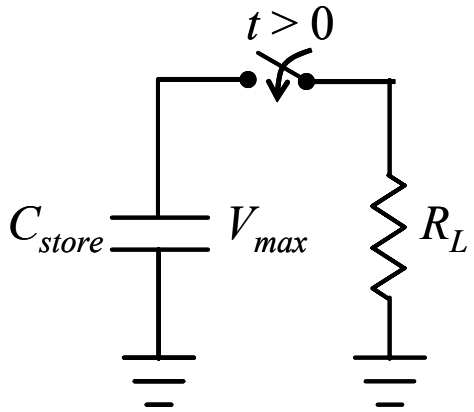

Figure 5.28 A schematic of a load, R_L, from a sensor to be powered by the maximum voltage, V_{max}, on C_{store}. The load is connected when the device "wakes up" and requires power. This event usually happens periodically as opposed to continuously for many of the devices that seek energy harvesting mechanisms for power.

5.6.6.6 Instantaneous Power from a Fully Charged Device

The goal of any energy harvesting mechanism is to be used to power another device, like a remote sensor. In many low power applications, these sensors do not require power continuously, but rather require power during a brief "wake-up" time used for periodic data collection. This "wake-up" time is application driven and thus, the power delivered by the energy harvesting mechanism will vary by application.

In addition to the time, another application driven variable is the parallel load, R_L, on the output, as shown in Figure 5.28, where the switch indicates when the sensor is connected to the energy harvesting device for power. In this example, it is assumed that the period of time between "wake-up" is greater than that to charge up C_{store} to V_{max}. The instantaneous power, P_{inst}, is then given by the expression in (5.39), where V_L is the voltage across the load as a function of V_{max} and $R_L C_{Store}$. From these equations, and as expected, P_{inst} increases with C_{store} for a given load, R_L. This also presents another factor to consider when selecting a proper size for C_{store}.

$$P_{inst} = \frac{V_L^2}{R_L} = \frac{V_{max}^2 e^{-\frac{2t}{R_L C_{store}}}}{R_L} \tag{5.39}$$

5.6.6.7 Additional Voltage Output Circuit Information

There are several important notes to make with the circuit discussed in the sections above. First, diodes are inherently leaky. Second, there is also a finite resistance between any capacitor and ground. Third, there are additional ohmic losses due to interconnect and the impedance of the test equipment. These three factors lead to the decay of the pre-charge voltage, $-V_{in}$, on C_{init} and of the harvested voltage, V_{out}.

Proper diode selection is paramount to success of this extraction circuit. Low leakage diodes have reverse leakage currents ranging from 0.5 nA to 200 nA. The best way to compensate for the effect of the reverse leakage current, and other contributions to circuit leakage, is to increase the bubble refresh rate such that the recharge occurs faster than leakage. Empirical results show that this is possible and will be shown in Section 5.6.8.

5.6.7 Conversion Circuit Simulation

The conversion circuit was modeled using a SPICE simulator. The model and the results are discussed below for a large and a small C_{store}. The diode model used in the simulation for D_1 and D_2 is the BAS116 diode model. This is the same diode used in the circuit that was tested and measured.

5.6.7.1 Simulation Model

As discussed in Section 5.6.6.2 and given by equation (5.27), the variable capacitor, C_{var}, can be modeled as a variable current source, $i_{Cv}(t)$. An illustration of how dC_{var}/dt results in an $i_{Cv}(t)$ is shown in Figure 5.29. The voltage output conversion circuit was simulated using the measured velocity value for a syringe pump delivering a volumetric flow rate of 100 μL/min. This velocity set the slope of the fall and rise time for the change in capacitance.

5.6.7.2 Conversion Circuit Simulation for a Small C_{store}

The value of the voltage on C_{init} is shown in Figure 5.30(a). This node remains at the value of V_{in} which was set to -5 V, and as such is labeled, V_{in}. The current, $i_{Cv}(t)$ caused by $dC_{var}/$

dt is shown in Figure 5.30(b) for the time duration of the simulation. The current through the charging diode, D_2, is shown in Figure 5.30(c). Note that as V_{out} increases, the magnitude of the peak current through D_2 decreases. The storage capacitor size used in this simulation was 100 pF. Recall that a small C_{store} will charge up to V_{max} relatively quickly as demonstrated by the output voltage, V_{out}, in Figure 5.30(d). The amount of ΔV_{out} for each leading bubble edge decreases as V_{out} increases. The maximum voltage that can be seen on V_{out} based on the change in C_{var} is 17 V. The predicted energy, E_{store}, is 0.14 nJ once $V_{out} = V_{max}$. The instantaneous power was calculated using equation (5.39) for a load resistance, R_L, of 100 kΩ. The Instantaneous power, P_{inst}, versus time for C_{store} = 100 pF is shown in Figure 5.32(b). The maximum instantaneous power that can be generated by this circuit is 3 mW.

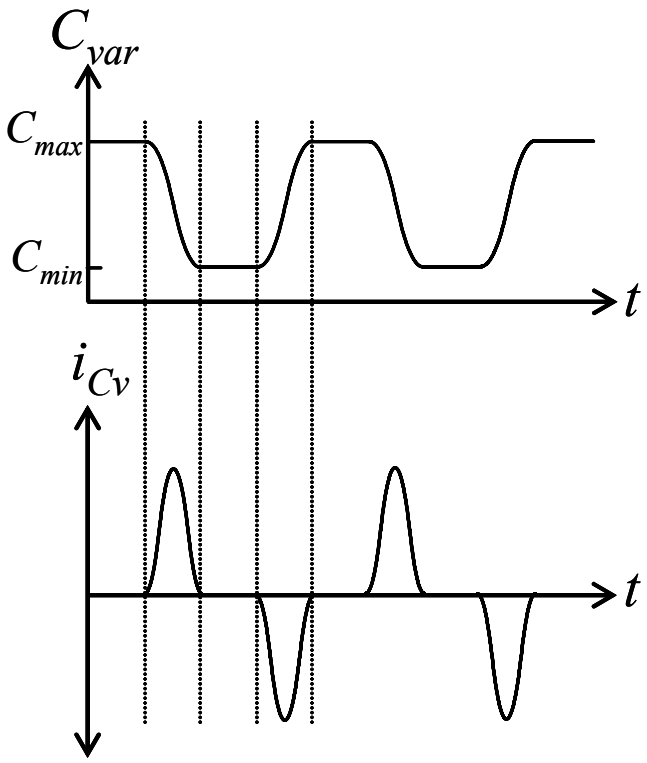

Figure 5.29 Illustration of the simulation model where C_{var} is modeled as a variable current source. As C_{var} goes from C_{max} to C_{min}, a current is generated to supply to the charging diode, D_2.

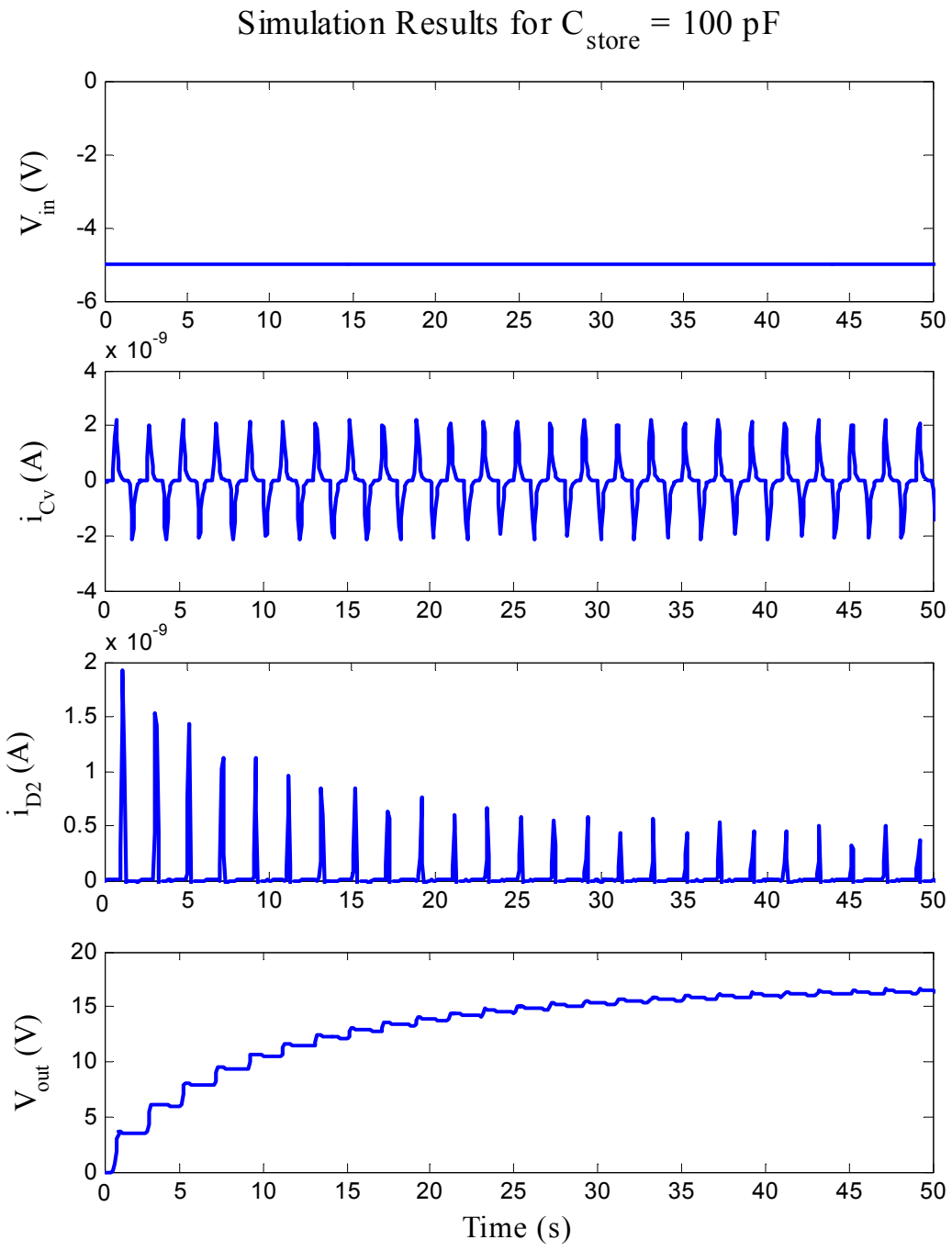

Figure 5.30 **Simulation results for voltage output conversion circuit for a small C_{store} of 100 pF. The fall and rise times were set by using measured velocities for syringe pump delivered volumetric flow rate of 100 µL/min. (a) Initial voltage at the node between C_{init} and C_{var}, (b) i_{Cv} versus time, (c) current through diode D_2, i_{D2}, conducts as C_{var} decreases, or at each simulated water to air interface (d) V_{out} versus time. V_{max} = 17 V. The energy, E_{store}, on C_{store} once $V_{out} = V_{max}$ is 0.14 nJ.**

5.6.7.3 Conversion Circuit Simulation for a Large C_{store}

The storage capacitor size used as a large capacitor value is 100 μF. The value of the voltage on C_{init} is shown in Figure 5.31(a). This node remains at the value of V_{in} which was set to -5 V, and as such is labeled, V_{in}. The current, $i_{Cv}(t)$ caused by dC_{var}/dt is shown in Figure 5.32(b) for the time duration of the simulation. The current through the charging diode D_2, $i_{D2}(t)$, is shown in Figure 5.32(c). As C_{var} decreases, the current through D_2 increases, as shown, so that it conducts to C_{store}. Recall that a large C_{store} will take a long time to charge up to V_{max}. As shown in (d), the output voltage, V_{out}, increases in small step sizes (note the scale on the *y*-axis in Figure 5.32 and compare to that in Figure 5.31). Each leading bubble edge increases V_{out} by approximately 4.7 μV. The maximum voltage, V_{max}, that can be seen on C_{store} = 100 μF is the same as that from C_{store} = 100 pF, where V_{max} = 17 V. However, because C_{store} is so large in this example, each ΔV_{out} is very small. Nonetheless, the predicted energy on C_{store} is 14.4 mJ once $V_{out} = V_{max}$.

The instantaneous power was calculated using equation (5.39) for a load resistance, R_L, of 100 kΩ. The Instantaneous power, P_{inst}, versus time for C_{store} = 100 μF is shown in Figure 5.32(a). The maximum instantaneous power that can be generated by this circuit is 3 mW. Note that because a larger C_{store} has more energy when charged to V_{max}, the time it takes to dissipate that energy (i.e. power) is longer.

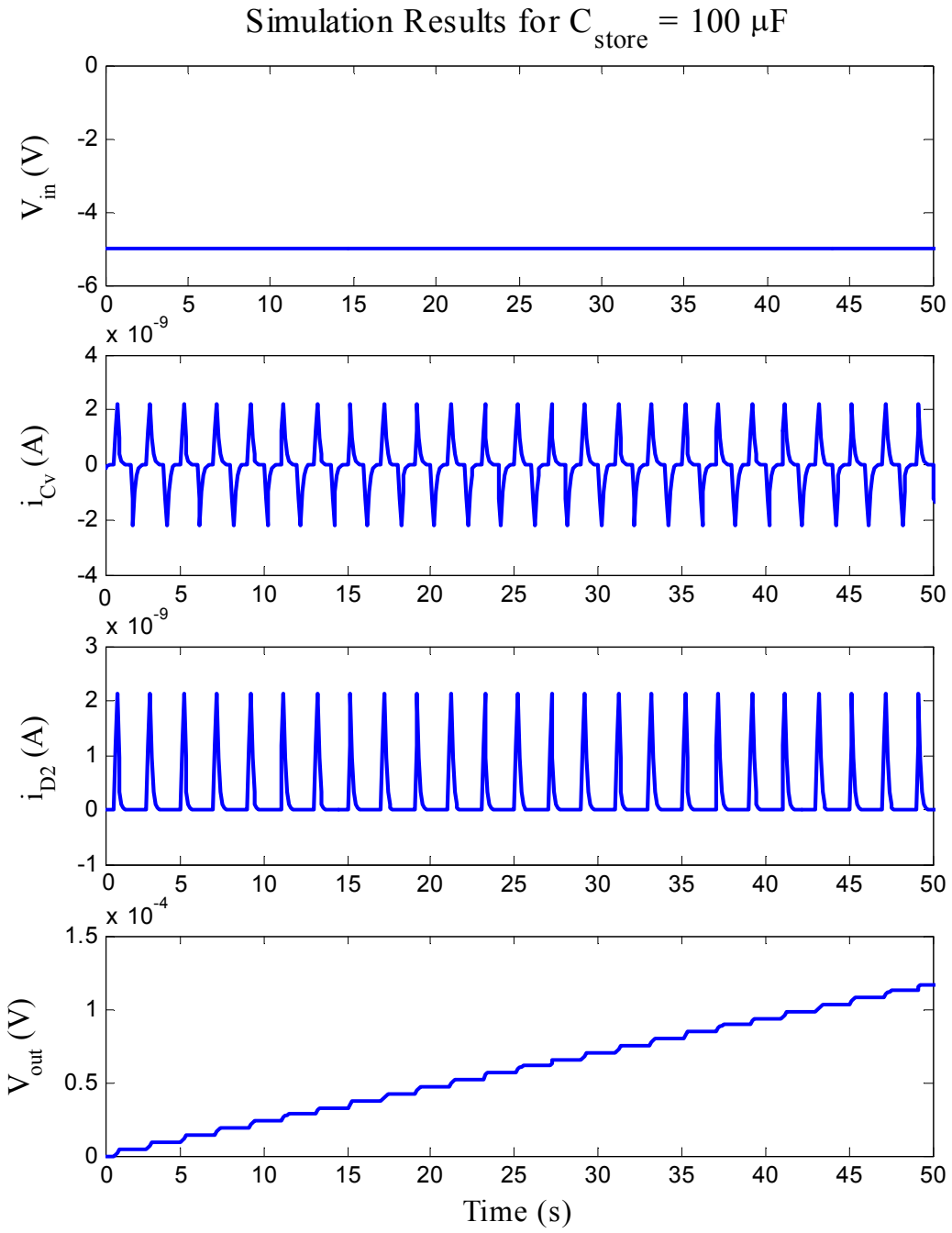

Figure 5.31 **Simulation results for voltage output conversion circuit for a large C_{store} of 100 µF. The fall and rise times were set by using measured velocities for syringe pump delivered volumetric flow rate of 100 µL/min. (a) Initial voltage at the node between C_{init} and C_{var}, (b) i_{Cv} versus time, (c) current through diode D_2, i_{D2}, conducts as C_{var} decreases, or at each simulated water to air interface (d) V_{out} versus time. V_{max} = 17 V for small C_{store}. Therefore, the energy, E_{store}, on C_{store} once $V_{out} = V_{max}$ is 14.4 mJ. However, V_{out} does not reach V_{max} in the transient time frame of the simulation. V_{out} at t = 50 s is 0.12 mV. E_{store} at t = 50 s is 7×10^{-13} J. The ΔV_{out} for each $-\Delta C_{var}$ is approximately 4.7 µV.**

(a)

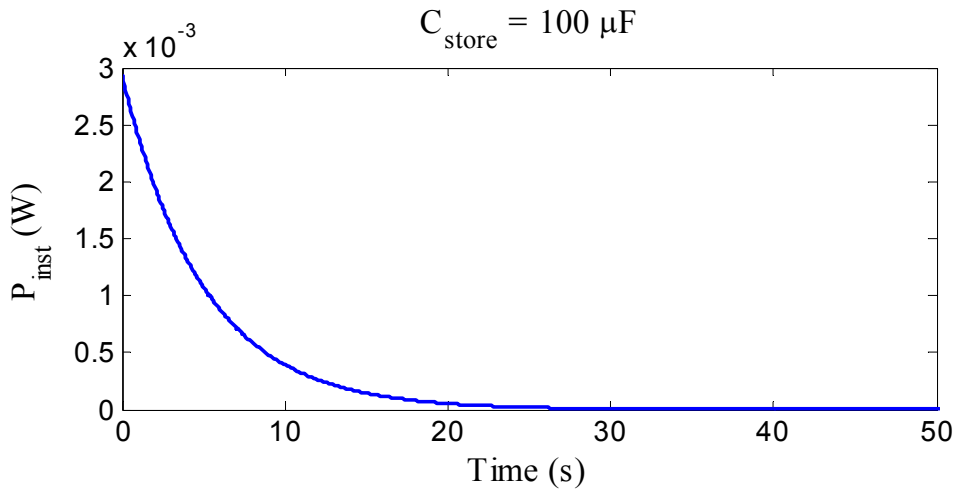

(b)

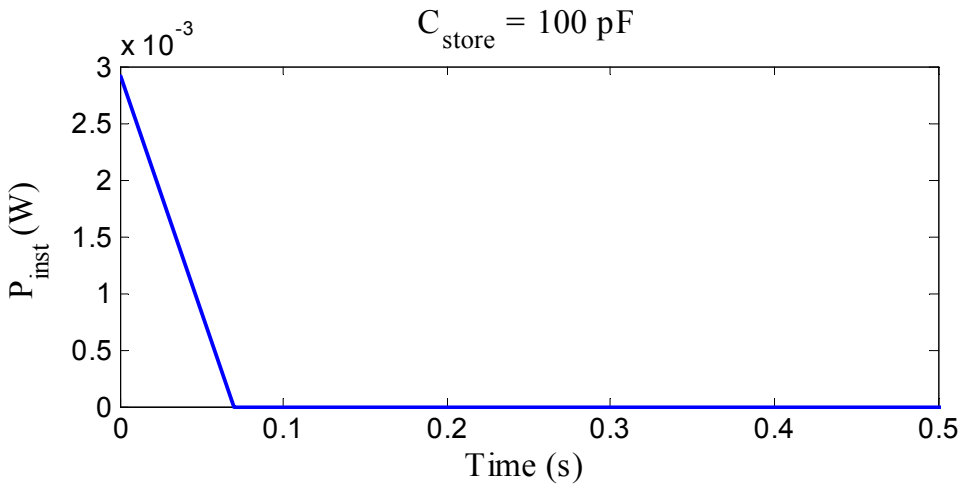

Figure 5.32 Simulation results for the instantaneous power, P_{inst}, for one large and one small C_{store} value. (a) P_{inst} versus time for C_{store} = 100 µF. (b) P_{inst} versus time for C_{store} = 100 pF. The power was calculated for a load resistance of 100 kΩ. From these simulations, it is clear that a small C_{store} will discharge very quickly, and as such, the selection of C_{store} is dependent upon the interval of time during which power is needed for the load.

5.6.7.4 Discussion of Simulation Results

Based on these simulation results, and given sufficiently low parasitic losses, the transpiration based energy conversion mechanism should be able to provide a measurable output for each leading bubble edge. Note however, that the velocities used in this simulation were those expected from a syringe pump providing a volumetric flow rate of 100 μL/min. This volumetric flow rate was used because *dC/dt* will be sufficiently high enough to provide an output voltage that is measurable. Based on measured results, we know that the volumetric flow rate set by the syringe pump results in a flow velocity that is approximately 20X that of the evaporator with 6 μm pore diameters. Thus, we can expect that the output of the evaporation driven flow would be 20X less than that of the syringe pump.

Further, a large C_{store} was selected for use during testing because of its long discharge time. Since the device was going to be tested "*in vivo*", that is, a multimeter was going to be continuously measuring the output voltage on C_{store}, it was imperative that the discharge time be significantly longer than the sample rate of the multimeter.

5.6.8 Voltage Output Conversion Circuit Results

During testing, polytetrafluoroethylene, or PTFE tubing was loaded with alternating sections of water and air bubbles to provide a large number of dielectric interfaces. The tubing was connected to s syringe that was loaded into a syringe pump to deliver a volumetric flow rate of 100 μL/min. The circuit in Figure 5.21 was pre charged to a voltage of -5 V when only water is between the variable capacitor electrodes (i.e. $C_{var} = C_{max}$) and then the voltage source was disconnected. The output voltage on C_{store} was then measured using an Agilent 34401A digital multi meter and recorded using a GPIB cable and LabVIEW interface. The resolution of the multimeter is 100 nV as reported by the manufacturer. A photograph of the test set-up is shown in Figure 5.33. A microscope and camera were used to record video of the bubbles traversing between the capacitor plates and synchronize them with the measured output voltage.

The measured output voltage, V_{out}, on C_{store} is shown in Figure 5.34. The output voltage is first measured for a few seconds with only water in between the variable capac-

itor plates ($C_{var} = C_{max}$ and $dC_{var}/dt = 0$). Note that the output voltage starts at a nominal voltage of approximately 0.95 V, ideally, this should be 0 V. The output voltage then decays slowly as a result of the impedance of the measurement instrument. When the syringe pump is switched on at around $t = 30$ s, bubbles begin to traverse between the variable capacitor electrodes causing C_{var} to change from C_{max} to C_{min} and back to C_{max}. Each leading bubble edge results in an increase in output voltage of approximately 2 - 5 μV. This is very close to the predicted voltage output from the simulation results shown in Figure 5.32(a) where $\Delta V_{out} = 4.7$ μV. The cause of the measurement variability could be due to two things: (1) the sample rate of the multimeter not synchronized with leading bubble edges, and (2) the flow rate was not always consistent due air, a compressible fluid, in the tubing. After the train of bubbles ended ($t = 110$ s), water was in between the variable capacitor electrodes and the output voltage was still recorded. The decay from the leakage in the circuit shows that within tens of seconds, the accumulated output voltage can be reduced. These data take into account: (1) the bubble refresh rate, which is affected by bubble size and was controlled by the syringe pump, (2) the leakage of diodes, and (3) the leakage and decay from capacitors, interconnect and parasitic resistance.

In Figure 5.35, the output voltage measured by the multi meter is normalized to start at $V_{out} = 0$ V and $t = 0$ s. This is to show what the output would look like if bubbles started

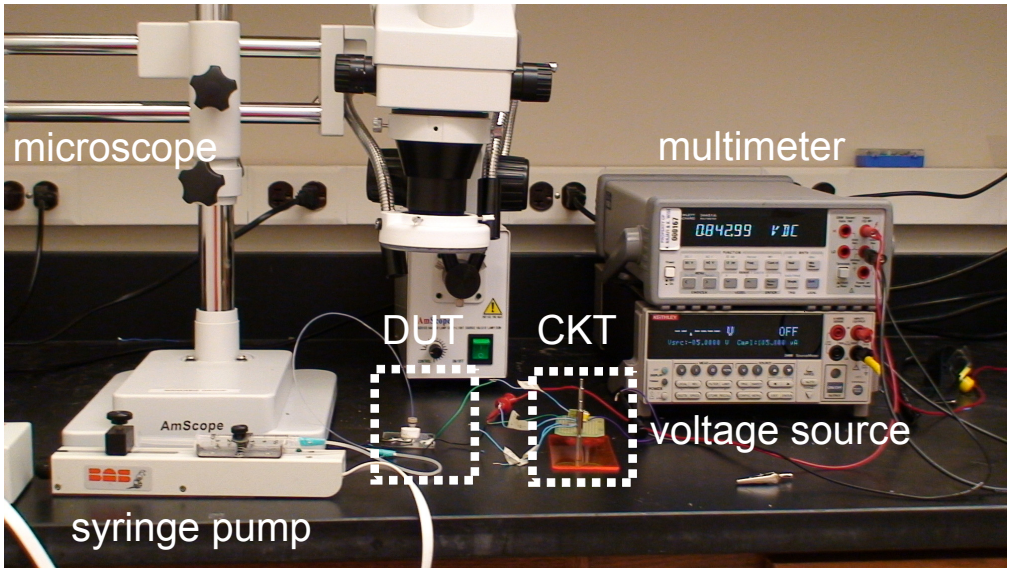

Figure 5.33 Output voltage conversion circuit measurement test set-up.

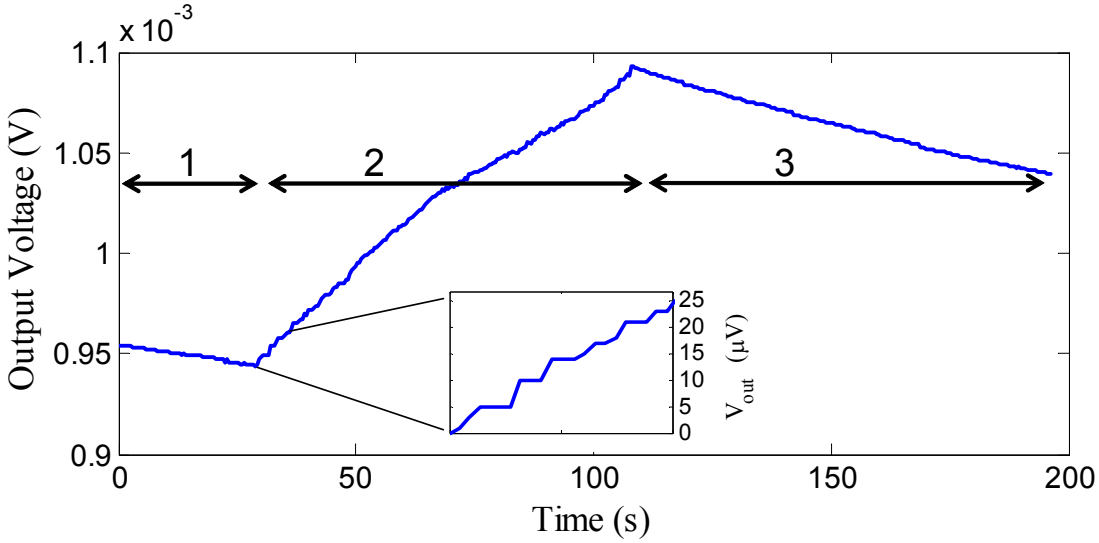

Figure 5.34 The measured output voltage (V_{out} on C_{store}) using Agilent 34401A digital multi meter. This plot has three regions. In region 1, $C_{var} = C_{max}$. In region 2, the syringe pump is switched on and many bubbles are going between the electrodes. C_{var} is changing from C_{max} to C_{min} at a rate set by a syringe pump at 100 µL/min. In region 3, only water is in the electrodes and $C_{var} = C_{max}$ and shows natural decay at the output in this region. The close up inset shows the steps due to individual bubbles. This data takes into account: (1) the refresh rate, which is affected by bubble size, (2) the leakage of diodes, and (3) leakage and decay from capacitors and interconnect.

---

going between the variable capacitor electrodes as soon as measurement began. These measured data still take into account the leakage in the circuit and shows that voltage accumulation can occur with the presented mechanism for mechanical to electrical energy conversion.

The output voltage is also directly compared with the simulation results. Good agreement is seen between simulation and measured results. However, at $t > 30$ s, the measured change in output voltage, ΔV_{out}, appears to decrease. This is due to the fact that the bubble size at $t > 30$ s was larger than the bubble size at $t < 30$ s, thereby reducing the refresh rate since there were fewer leading bubble edges causing fewer changes in C_{var}.

The measured energy as compared to the simulated results is shown in Figure 5.36. The actual measured value for ΔE_{store} for each leading bubble edge is approximately 1.3×10^{-15} J, depending on the ΔV_{out} for each leading bubble edge. After 50 seconds, the total energy on C_{store}, $E_{store}(50)$ is measured to be approximately 5.3×10^{-13} J.

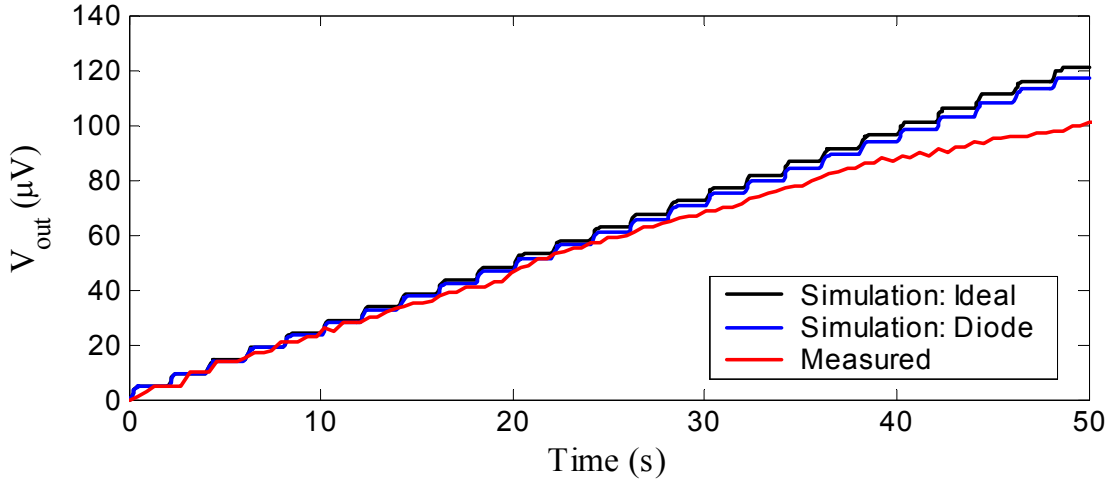

Figure 5.35 **The measured voltage output, V_{out}, plotted such that V_{out} = 0 V at t = 0 s. This measurement is compared to the simulation results for both ideal and the actual diode. These data show that voltage accumulation can occur even with inherent leakage in the system. The bubble length of the bubbles going between the electrodes was longer at t > 30 s than at t < 30 s reducing the refresh rate was slower. The slow refresh rate caused the measurements to vary from the simulation results after t = 30 s. However, good agreement between simulation and measurements is seen for t < 30 s.**

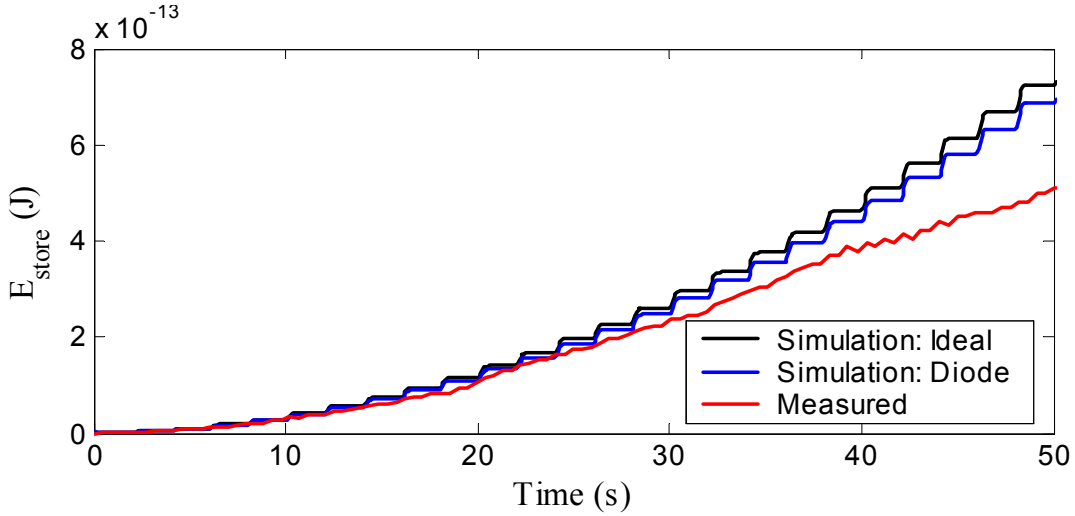

Figure 5.36 **The measured energy, E_{store}, on the storage capacitor, C_{store}, compared to the simulation results both ideal and the actual diode. Energy is calculated as E_{store} = 1/2 C_{store} V_{out}^2. The maximum energy that can be harvested onto C_{store} using the flow rate 100 µL/min is 14.4 mJ.**

The maximum instantaneous power for this circuit, given the good agreement between simulation and measurement, is expected to be 3 mW once $V_{out} = V_{max}$, and was given in Figure 5.32(a). Additional volumetric flow rates were tested and the ΔV_{out}/second

Table 5.3 The output voltage per second as a function volumetric flow rate.

Volumetric Flow Rate (μL/min)	ΔV_{out}/second (V/s)
100	2.0×10^{-6}- 5.0×10^{-6}
20	0
5	-1.00×10^{-6}, baseline leakage
0	-1.00×10^{-6}, baseline leakage

was measured and is shown in Table 5.3. At low volumetric flow rates at or less than 20 μL/min, the change in voltage is negligible or even negative due to the fact that the leakage is greater than the accumulated voltage.

5.7 Theoretical Limit of Transpiration Based Energy Harvesting

The theoretical limit of this technology depends on the size of the leading bubble edge interface. As shown in Figure 5.37, the minimum variable capacitor length to allow for a change in capacitance from C_{max} to C_{min} by a leading bubble edge is 150 μm. Therefore, the minimum area, A_{min}, required for each variable capacitor is determined by equation (5.40), where w = 500 μm and l = 150 μm for a minimum area of $A_{min} = 7.5\times10^{-8}$ m^2.

$$A_{min} = wl \tag{5.40}$$

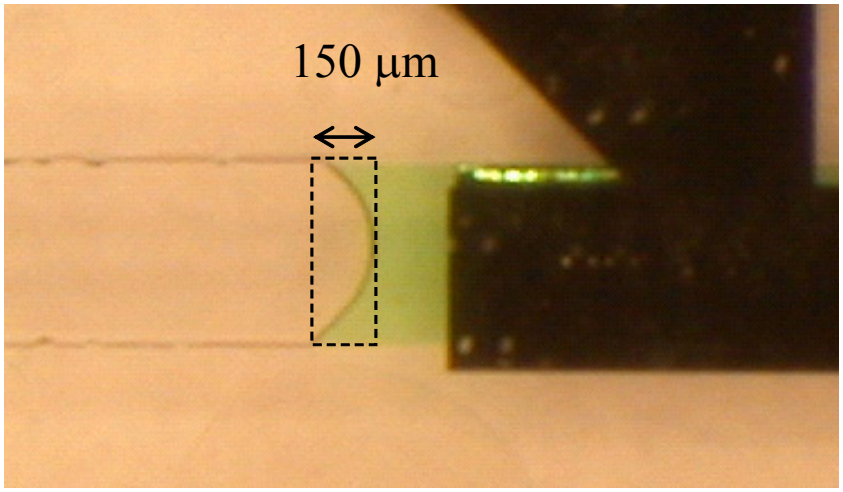

Figure 5.37 Micrograph showing the leading edge of a bubble. The meniscus radius gives an idea of the minimum variable capacitor length that can be used in a transpiration based energy harvesting system.

Table 5.4 The average power scavenged by fully charged device calculated by taking the energy on C_{store} at V_{max} = 17 V and dividing it by the time to reach V_{max}. The maximum power density as a function of area is calculated by dividing the power from a single device by the interface area.

C_{store}, F	Time to Reach V_{max}, s	$E_{store}(V_{max})$, J	P_{single}, W	$P_{density}$, W/cm^2
10×10^{-12}	3	1.4×10^{-9}	0.5×10^{-9}	0.6×10^{-6}
100×10^{-12}	50	14×10^{-9}	0.3×10^{-9}	0.4×10^{-6}

This device will be operated in charge and discharge cycles. Therefore, to calculate the average power, one can divide the energy on the storage capacitor, C_{store}, when it is charged to V_{max}, over the time that it will take to accumulate a voltage of V_{max}. Energy on C_{store}, E_{store}, at V_{max} is given by equation (5.41).

$$E_{store} = \frac{1}{2} C_{store} V_{max}^{\ 2} \tag{5.41}$$

As discussed in previous sections, the time that it takes to reach V_{max} is dependent upon the size of C_{store}. Thus, an estimate of the theoretical upper bound of power density from this technology is calculated as a function of the size of C_{store}. As shown in Figure 5.30, the time that it takes to reach within 5% of V_{max} = 17 V for C_{store} = 100 pF is approximately 50 seconds. Additional simulations were run for C_{store} values of 10 pF, 100 nF, 1 μF, and 100 μF. However, due to memory limitations of the simulation software package, the time required to accumulate V_{max} on C_{store} was not determined for C_{store} > 100 pF. Table 5.4 lists the time that it takes to charge up to C_{store} to V_{max}, the energy on E_{store}, the average power from a single device, P_{single}, and the power density, $P_{density}$, calculated as a function of area for C_{store} = 10 pF and 100 pF. From Table 5.4 it is clear that the smaller C_{store} provides a higher power density. Device performance could be improved by reducing the channel height to increase ΔC_{var}.

5.8 Energy Efficiency

If the transpiration-based energy conversion mechanism presented in this chapter is to be used as a stand alone energy harvesting device, the energy efficiency must be greater than 0%. That means that for every Joule of energy input to charge the initial capacitor, C_{init}, a greater number of Joules are output or stored on the storage capacitor, C_{store}.

From [57], two modes of operation for an energy harvesting device can be defined when it is used to power an electronic device. The first is when the power consumption of electronic device is less than the power provided by the energy harvester. The second is when power consumption of the electronic device is larger than the power provided by the energy harvester. The second case is the more likely case if the transpiration-based energy harvesting device were implemented. Thus, the operation of the electronic device that is suitable is a discontinuous one. For example, a sensor that takes a measurement once a day or once an hour. Based on the discussion in [57], for discontinuous modes of operation it is more useful to describe the energy generated rather than the power generated because the energy sets the time limit between device operation. Figure 5.38 illustrates the power and energy generated and spent versus time for the discontinuous operation example described above. In the case of discontinuous operation, the electronic device shuts down until sufficient energy levels are stored on C_{store}.

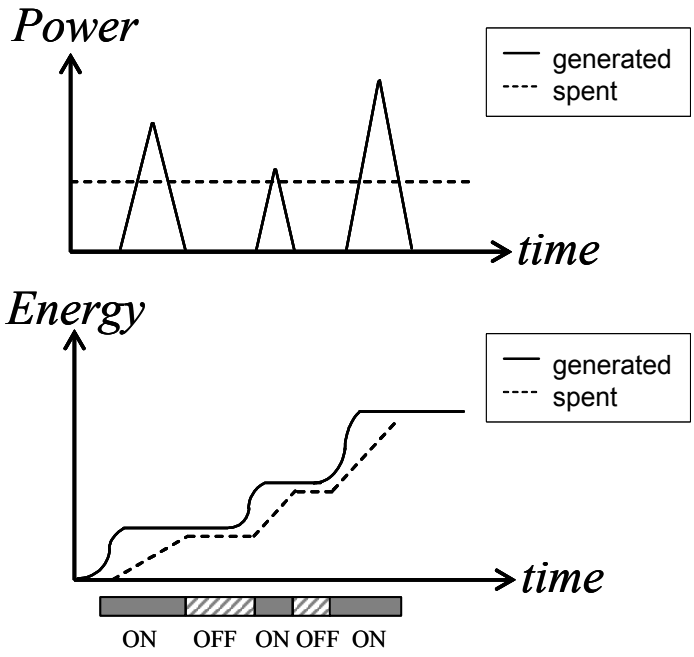

Figure 5.38 Power and energy versus time in the case of discontinuous operation. For this case, the device must be OFF until enough energy is collected in the storage element. Caption and figure adapted from Figure 4(b) in [57].

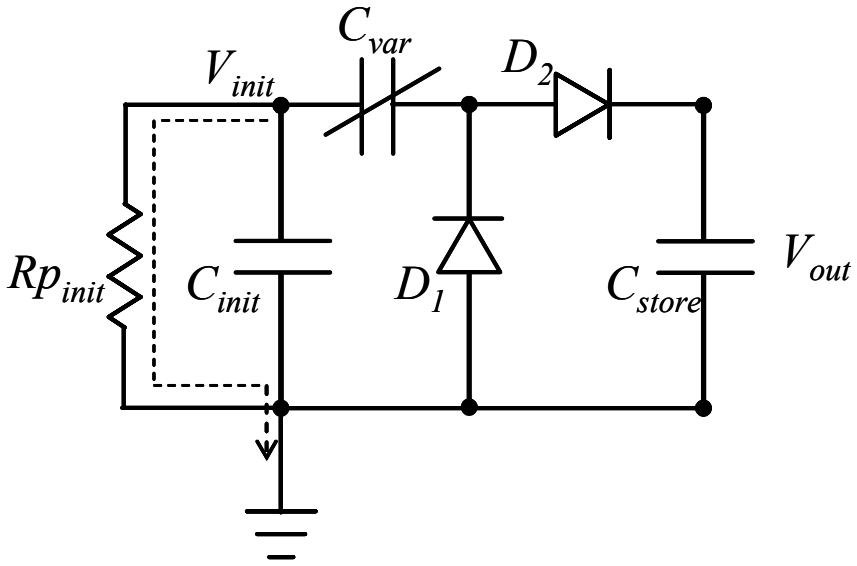

Figure 5.39 Energy conversion circuit showing finite resistor, Rp_{init}, that provides a resistive path to ground to drain V_{init} from C_{init}. The magnitude or Rp_{init} will determine how quickly C_{init} will lose its charge.

The limiting component for energy efficiency is the initial capacitor. This capacitor has a finite resistive path to ground, as shown in Figure 5.39. The magnitude of that parallel resistance, Rp_{init}, will determine how quickly the initial capacitor will lose charge and require a refresh from another power supply, battery, or capacitor. For the devices in this work, the initial capacitor had a manufacturer specified parallel resistance of 10 GΩ. This large parallel resistance results in low leakage and thus, due to memory limitations of simulation software, could not be used to show how long it would take to drain all of V_{init} from C_{init}. Therefore, an exaggerated leakage caused by a small Rp_{init} is used to discuss the energy efficiency requirements of the transpiration-based energy conversion device should it be used as a stand alone energy harvester. With a small Rp_{init} value of 10 MΩ, we expect that the charge on the initial capacitor will drain quickly. An example of the loss of V_{init} on C_{init} is given in Figure 5.40(a) which will then yield in an output voltage, V_{out}, on C_{store} as shown in Figure 5.40(b). Even if the variable capacitor is still changing (i.e. bubbles are still traversing between the variable capacitor electrodes), no output voltage can be accumulated if $V_{init} = 0$ V. As the absolute value of V_{init} approaches 0 V, the current caused by the change in capacitance also decreases as is obvious from equation (5.27). Obviously, a

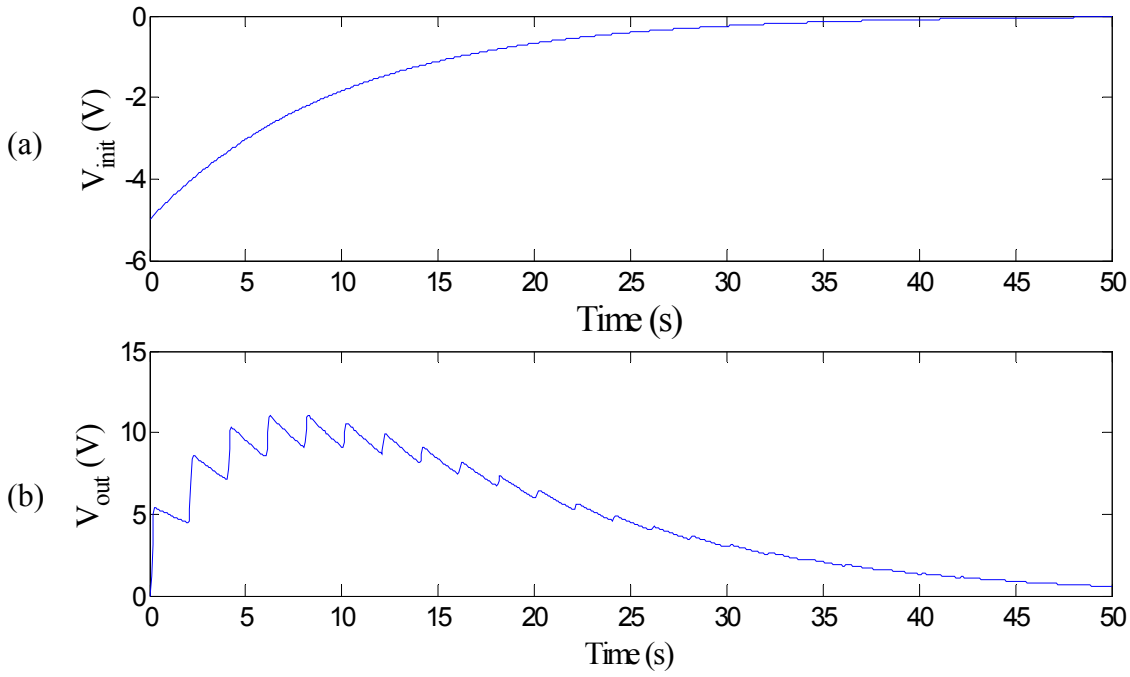

Figure 5.40 The initial voltage, V_{init}, and output voltage, V_{out}, on C_{init} and C_{store}, respectively, due to a high leakage from a small parallel resistance on C_{init}. This example uses an exaggerated leakage resistance to illustrate the refresh requirement concept. In this case, there is not refresh of the initial voltage and it slowly drains to 0 V.

capacitor with a 10 GΩ parasitic resistance will discharge 1000 times slower, or in approximately 30 s × 1000 = 8.3 hours.

Some overhead electronics will be included in order to regulate a refresh circuit in an actual implementation of this technology as a stand alone energy harvesting device. An example of the proposed refresh circuit is shown in Figure 5.41. Many researchers have studied the control electronics for this purpose and it is a topic of ongoing investigation [93],[99],[100]. The overhead electronics will utilize a switch or a diode to recharge the initial capacitor to V_{init} when the magnitude of the potential across C_{init} drops below a certain level. An example of simulation results of the recharge on V_{init} is given in Figure 5.42(a) yielding an output voltage, V_{out}, shown in Figure 5.42(b). Based on these simulations, the percent efficiency of this technology as a stand alone energy harvesting device can be calculated using equation (5.42), where the final energy of the system, E_{final}, is given by equation (5.43), the initial energy in the system, $E_{initial}$, is given by equation (5.44), and $E_{overhead}$ is the energy requirement of the overhead electronics to refresh the initial voltage on C_{init}. Note that V_{init} is the starting initial voltage, which in these examples is -5 V.

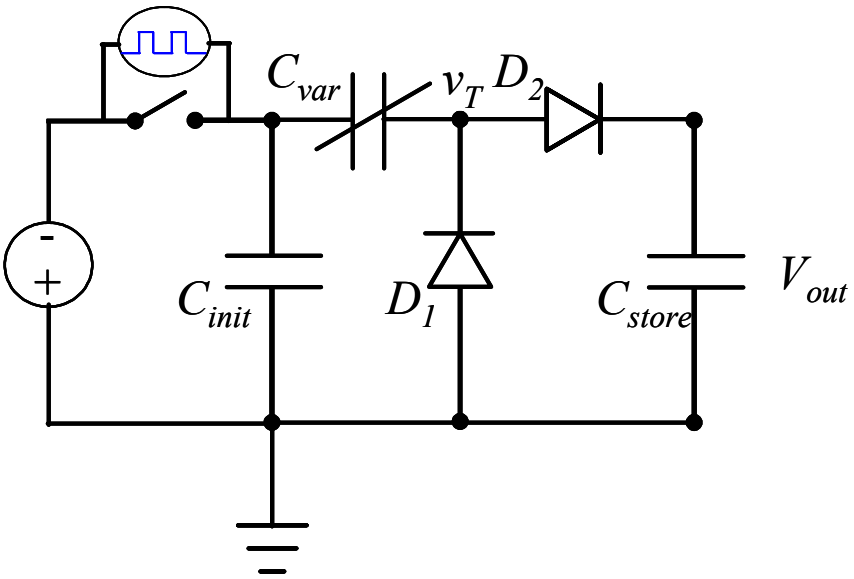

Figure 5.41 Proposed circuit to refresh the V_{init} on C_{init} using a switch and power supply.

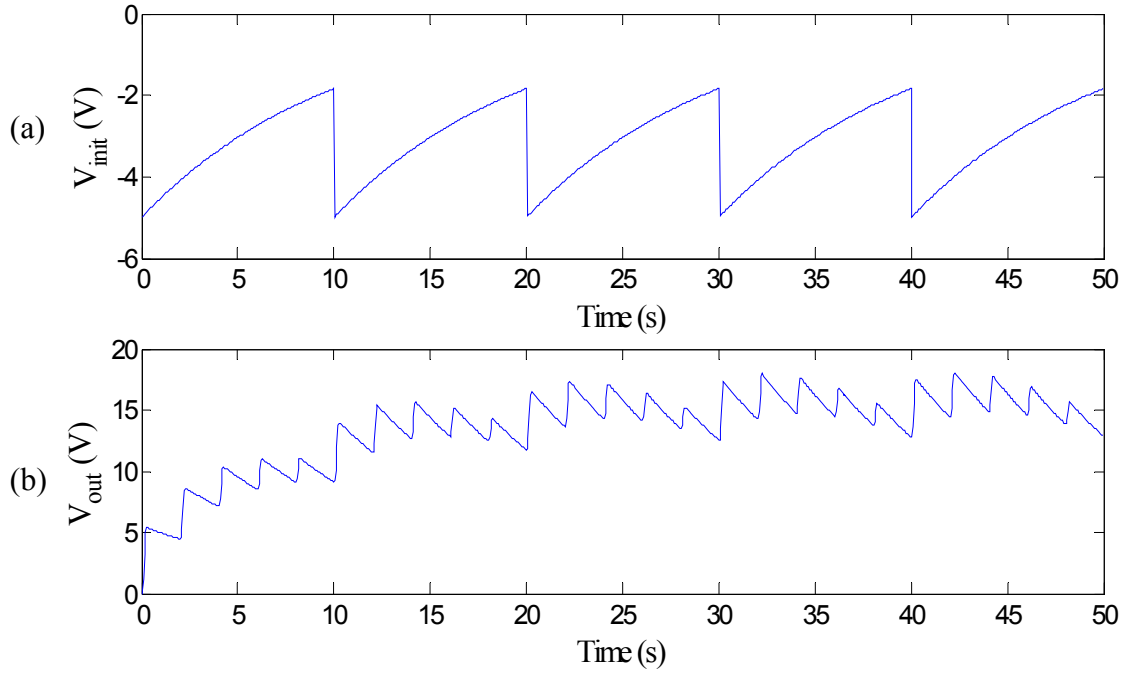

Figure 5.42 The initial voltage, V_{init}, and output voltage, V_{out}, on C_{init} and C_{store}, respectively, using a refresh circuit to recharge the voltage, V_{init}, on C_{init}. This example uses an exaggerated leakage resistance to illustrate the refresh requirement concept and the initial voltage is refreshed every 10 s using the circuit in Figure 5.41.

$$Efficiency = \left(\frac{E_{final}}{E_{initial} + E_{overhead}} - 1 \right) \times 100 \tag{5.42}$$

$$E_{final} = \frac{1}{2} C_{init} \left(\frac{V_{init}}{2} \right)^2 + \frac{1}{2} C_{var} \left(\frac{V_{init}}{2} \right)^2 + \frac{1}{2} C_{store} V_{out}^{\ 2} \tag{5.43}$$

$$E_{initial} = \frac{1}{2} C_{init} V_{init}^{\ 2} + \frac{1}{2} C_{var} V_{init}^{\ 2} + \frac{1}{2} C_{store} V_{out}^{\ 2} \tag{5.44}$$

Using equations (5.42) - (5.44), a bound can be set for the maximum energy consumption of the overhead electronics, $E_{overhead}$, in order to achieve a percent efficiency great than 0%. Simulation results for the percent efficiency as a function of the energy consumption of overhead electronics is given in Figure 5.43. At small C_{store} values such as 1 nF, the energy harvesting mechanism would achieve negative efficiency, meaning that

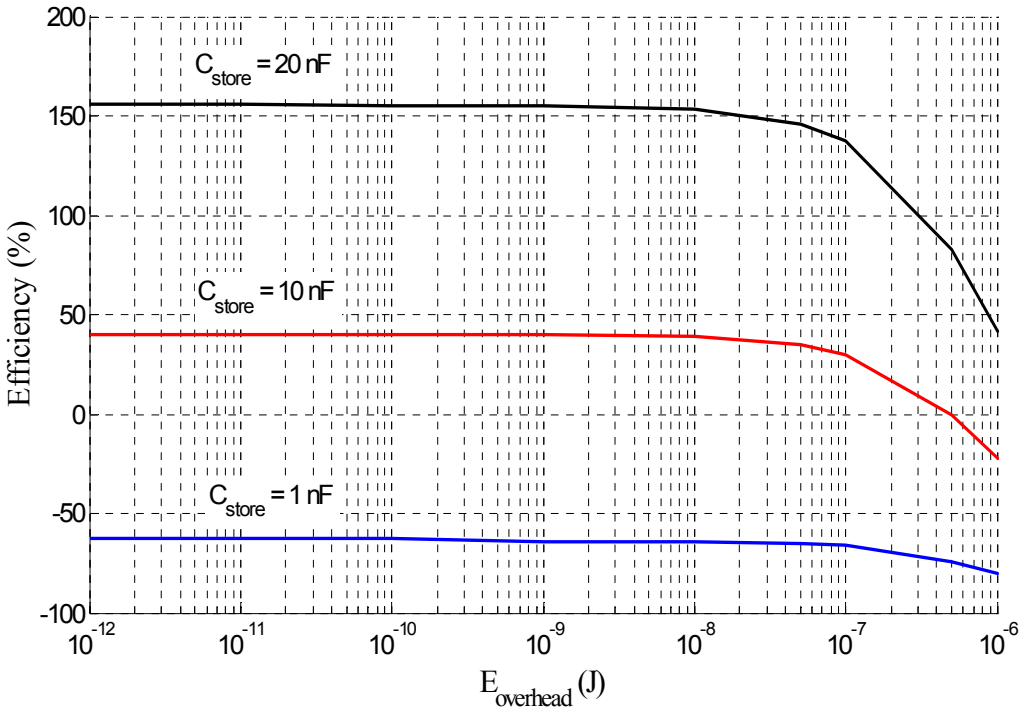

Figure 5.43 Percent efficiency versus energy requirements of overhead electronics. The efficiency is dependent upon the size of C_{store} and C_{init}. For all of the simulation results above, C_{init} = 100 nF and C_{store} was varied from 1 nF to 20 nF. Best efficiency is achieved with a large C_{store}. At small C_{store} values of 1 nF, the energy harvesting mechanism would achieve negative efficiency where more energy is input into the system than is being harvested. The energy consumption of the overhead electronics should be less than 1 µJ per refresh cycle in order to achieve a percent efficiency greater than 0% for a C_{store} = 20 nF.

more energy is input into the system than is being harvested out. The energy consumption of the overhead electronics should be less than 1 μJ per refresh cycle in order to achieve a percent efficiency greater than 0% for a C_{store} = 20 nF. For comparison, a single 0.25 μm MOSFET running at 5 V would have an energy consumption of approximately $0.5 \times C_{gate} V^2 = 1/2 \times 5$ fF $\times 5^2 = 62.5$ fJ.

The ultimate efficiency of the use of the transpiration based mechanism as a stand alone energy harvesting device will be determined by the requirements of the overhead electronics and the requirements of the electronic device that will be powered by the energy harvester. Further exploration of this topic is necessary in any future research of transpiration based energy harvesting mechanisms.

5.9 Summary of Chapter Contributions

A transpiration based energy conversion device was presented in this chapter. The device introduced a novel mechanism for electrostatic electrical energy harvesting from evaporation-driven motion. The device was inspired by microvasculature in plants to maximize hydraulic conductance during transpiration. The microfluidic nature of the design was characterized and enhanced using porous material as evaporators. Subsequently, the electrical aspects of the design were characterized including measured changes in capacitance, current flow due to charge redistribution, charge, voltage output from a conversion circuit, energy, and power. All results accounted for leakage inherent in the circuits which included the leakage contribution of diodes, interconnect, and instrumentation. Devices were also coupled to show that the outputs can be added using the same circuit and that multiple devices can either increase the refresh rate or increase the magnitude of the output current, showing how multiple devices can help the refresh rate. Both simulation and measured results are included for all electrical parameters. The theoretical upper bound on the scavenged power density, as a function of the size of the storage capacitor in the device, was determined. Lastly, a discussion of the maximum energy requirements of overhead electronics to maintain positive efficiency was presented.

CHAPTER VI

CONCLUSION

The technical contributions and achievements of this work are described within this chapter.

6.1 Summary of Thesis Contributions

This thesis has described the use of transpiration as mechanism for energy conversion. Two technologies were developed, modeled, and tested. Both transpiration based technologies were inspired by plants. The transpiration based actuators were inspired by the fern sporangium mechanism for spore dispersal. The transpiration based electrical energy conversion technology was inspired by the passive pumping mechanism in plants. The technology related achievements and contributions of this work are as follows:

6.1.1 Development and Analysis of Transpiration Actuation

The surface tension of water is coupled with evaporation at room temperature to result in a distributed actuation mechanism. An analytical model based on the principle of virtual work was developed to study this mechanism. Micro scale devices were fabricated through a single mask process using a silicone polymer. They present the basis for a way to create bottom up self-assembly by using the transient water-driven deflections of multiple devices. The microactuators exhibited large tip deflections of 3.5 mm, angular rotations of 330^{o}, and forces per unit length of 5.75 mN/m to 67.75 mN/m depending on geometric design parameters. Empirical and theoretical results both conclude that scaling into the nano-regime would also yield large actuation deflections. During the exploration of nano

scale actuators, a fabrication process was developed to make suspended PMMA actuators with feature sizes as small as 80 nm.

The transpiration driven actuators developed here provide the basis of a robust method for using surface tension, evaporation, and geometrically programmed deformation profiles as a way to make common materials transpiration based actuating sheets.

6.1.2 Transpiration for Electrical Energy Harvesting

A novel device consisting of a biomimetic leaf like microchannel network was embedded with alternating dielectrics of water and air bubbles. As each water to air interface passed between capacitor electrodes, energy can be harvested electrostatically. The main contributions of this portion of the thesis is that it provides a compelling proof of concept for the use of transpiration as an energy conversion mechanism that could be used in energy harvesting applications. The study of this mechanism includes the following:

- Fluidic analysis and characterization of the flow rates of bubbles in microchannels via evaporation-driven flow were carried out to optimize the hydraulic resistance of channels using Murray's Law.

- Enhancement of evaporation-driven flow by porous materials as evaporators led to a several order of magnitude increase in volumetric flow rate.

- Modeling and measurement of pressures in the full system that affect the flow rate including that due to a non-zero voltage on the capacitive electrodes.

- Theoretical and empirical measurements of current and charge generated by each change in capacitance from water to air with various fluidic flow rates using a charge redistribution circuit. Further, empirical measurements show that individual devices can be placed in parallel to generate more current.

- A thorough analysis of the theory governing a voltage output conversion circuit was presented including simulation results. This analysis was used to compare the effect of various discrete component properties on the output voltage (i.e. storage capacitor and diodes).
- Perhaps the most significant contribution of this work is the demonstration that evaporation driven flows can be used to charge pump a storage capacitor for use as an energy source. An energy conversion circuit was theoretically analyzed, modeled, and tested to exhibit an accumulated voltage on a storage capacitor due to the flow of bubbles and water between electrodes in microchannel. An accumulation in voltage of 2 - 5 μV was measured for each leading bubble edge. A discussion using the theoretical analysis and simulation describes how to modify the conversion circuit, and subsequently, dV_{out}/dt, to suit an energy harvesting application.
- Most importantly, this work has demonstrated that evaporation driven flows can be used to charge pump a storage capacitor for use as an energy source. Further, this thesis presents a thorough analysis of the conversion circuit to enable optimization of its use in this, and other electrostatic energy harvesting technologies.

6.2 Future Research Topics

Although the prototypes developed in this work were successful proofs-of-concept of transpiration as a mechanism for energy conversion, there are certainly many performance metrics and design aspects that can be improved to suit additional applications in sensing and energy harvesting.

6.2.1 The Future of Transpiration Actuation

One interesting topic that warrants further investigation is the use of transpiration actuation as a mechanism to geometrically program deformation profiles in sheets of material. An

early proof of concept was demonstrated in Section 2.10, however, this technology would be very interesting to explore at the nanoscale where sheets of material could be designed to deform with changes in humidity and temperature. Further, they can be used as sensors based on the environmental conditions that cause evaporation and condensation.

6.2.2 Transpiration for Electrical Energy Harvesting

The use of transpiration for electrical energy harvesting presents many interesting topics that warrant further investigation.

- In this thesis, the device utilized alternating flow of bubbles and water in straight main channels. Obviously the introduction of a bubble into the system requires energy. However, an air bubble can be replaced by a dielectric bead such as a polystyrene bead. The air bubbles are used for the development and characterization of the presented energy conversion mechanism. A future modification would be to embed a bubble, or another dielectric like a polymer with a low dielectric constant, in a circulating track where the same bubble or polymer bead acts like a dynamo as it passes through the capacitor plates. Use of a polystyrene bead is suggested for future research on the explored mechanism of transpiration for energy conversion.
- In this work, porous evaporators were used to enhance the evaporation driven flow. An interesting future direction would be to embed these porous evaporators into the microfabricated channels and to couple the bifurcating networks that obey Murray's Law with the small cylindrical networks in porous materials to yield an optimized flow rate via evaporation.
- Another significant topic that warrants further investigation is the use of a different substrate material. A glass substrate was used in this work for testing purposes so as to be able to visually observe when bubble motion though the channel. Glass, however, is not an ideal fabrication material for this work because it usually requires isotro-

pic wet etching, which provides poor aspect ratios. A better material would be silicon, where dry etching can achieve excellent aspect ratios.

- Another benefit to using silicon is that the capacitor electrodes could be made out of doped silicon and then an ultra-thin, but excellent and pinhole free dielectric insulator of silicon dioxide would be thermally grown. The devices in this work utilized approximately 1 μm of parylene C to insulate one of the capacitor electrodes. The thickness of this material greatly limits the change in capacitance from water to air. However, the 1 μm thickness was necessary to achieve a pinhole free layer using parylene. A much larger ΔC_{var} would be obtained as the dielectric thickness is reduced. The silicon dioxide would also have the added benefit of being hydrophilic.

- Another important subject that should be explored in the future development of a stand alone energy harvesting device is the package in which that device will be housed. A package contains the connections from the device to the outside world and can add up to the majority of the cost of an electronic device. Like energy harvesting applications, no one package meets the needs of all electronic components because each device will operate in a specific environment. The devices in this work will operate by either using condensation or another water supply as a source at the inlet and by using evaporation at the outlet to drive the flow of water. Therefore, the package that can be used for this device must have an opening to the outside world. However, the charge pump circuit of the full system must be isolated from moisture in the environment to prevent electrical shorting due to water.

- For these devices to be used as stand alone energy scavengers, a reliable source of water is necessary. The devices developed in this work can be used in two areas: 1) Applications where water is available,

one example would be on fire hydrants, and 2) applications where moisture could be collected from the environment via condensation. Researchers are using biomimicry to develop such techniques for water harvesting [15] which can be used as a water source for the technology in this thesis. This technology would require that the package be open to the environment in order to collect water. The former application, where water is available, would require the package to have an inlet and outlet for the water.

- Lastly, further studies of the energy requirements of overhead electronics like those discussed in Section 5.8 must be carried out to determine the energy efficiency of a transpiration based method of energy harvesting including refresh electronics.

6.3 Concluding Remarks

This thesis presented the use transpiration as a mechanism for energy conversion. Two transpiration based energy conversion micro devices were developed successfully. The first use of transpiration is to drive a microactuator that uses evaporation as an energy source. The second use of transpiration is as an electrical energy conversion mechanism that could be used as an energy harvester. Devices were developed, modeled, and characterized. Topics that warrant further investigation were presented in the previous section. It is the authors aim that the transpiration based energy conversion mechanism introduced and developed in this thesis to be refined to a point where it can be used as an energy harvesting technology to replace batteries for low power sensor electronics.

BIBLIOGRAPHY

[1] B. Warneke, M. Last, B. Liebowitz, and K. S. J. Pister, "Smart Dust: communicating with a cubic-millimeter computer," *Computer*, vol. 34, pp. 44, 2001.

[2] S. Roundy, "On the effectiveness of vibration-based energy harvesting," *Journal of Intelligent Material Systems and Structures*, vol. 16, pp. 809, 2005.

[3] M. A. Qidwai, J. P. Thomas, J. C. Kellogg, and J. Baucom, "Energy harvesting concepts for small electric unmanned systems," *Proceedings of SPIE - The International Society for Optical Engineering*, San Diego, CA, United States, 2004.

[4] M. Stordeur and I. Stark, "Low power thermoelectric generator-self-sufficient energy supply for micro systems," *Proceedings of the XVI International Conference on Thermoelectrics ICT '97'*, 1997.

[5] K. Sunghwan, W. W. Clark, and W. Qing-Ming, "Piezoelectric energy harvesting with a clamped circular plate: analysis," *Journal of Intelligent Material Systems and Structures*, vol. 16, pp. 847, 2005.

[6] J. A. Paradiso and T. Starner, "Energy Scavenging for Mobile and Wireless Electronics," *IEEE Pervasive Computing*, pp. 18, 2005.

[7] S. P. Beeby, M. J. Tudor, and N. M. White, "Energy harvesting vibration sources for microsystems applications," *Measurement Science and Technology*, pp. R175, 2006.

[8] A. P. Chandrakasan, S. Sheng, and R. W. Brodersen, "Low-power CMOS digital design," *IEEE Journal of Solid-State Circuits*, vol. 27, pp. 473, 1992.

[9] C. D. E. Lakeman, P. F. Fleig, J. L. DeGreeff, and J. T. Trainor, "Hybrid power for wireless sensors," *Proceedings of SPIE*, vol. 6231, 2006.

[10] S. Roundy, "Energy scavenging for wireless sensor nodes with a focus on vibration to electricity conversion," Ph.D. Dissertation, University of California-Berkeley, 2003

[11] Y. Bar-Cohen, "Biomimetics - using nature to inspire human innovation," *Bioinspiration & Biomimetics*, vol. 1, pp. 1, 2006.

[12] O. H. Schmitt, "Some interesting and useful biomimetic transforms," *Proceedings of the 3rd International Biophysics Congress*, Boston, MA, 1969.

[13] R. Bhardwaj, R. L. Pan, and E. L. Gross, "Solar energy conversion by chloroplast photoelectrochemical cells," *Nature*, vol. 289, pp. 396, 1981.

[14] D. Henderson and S. Ragona, "Nanometer precision robot for active photonics alignment using INCHWORM motors," *Proceedings of SPIE*, San Jose, CA, USA, 2001.

[15] A. R. Parker and C. R. Lawrence, "Water capture by a desert beetle," *Nature*, vol. 414, pp. 33, 2001.

[16] G. W. Taylor, J. R. Burns, S. A. Kammann, W. B. Powers, and T. R. Welsh, "The Energy Harvesting Eel: a small subsurface ocean/river power generator," *IEEE Journal of Oceanic Engineering*, vol. 26, pp. 539, 2001.

[17] V. Namasivayam, R. G. Larson, D. T. Burke, and M. A. Burns, "Transpiration-based micropump for delivering continuous ultra-low flow rates," *Journal of Micromechanics and Microengineering*, vol. 13, pp. 261, 2003.

[18] T. Vestad, D. W. M. Marr, and J. Oakey, "Flow control for capillary-pumped microfluidic systems," *Journal of Micromechanics and Microengineering*, vol. 14, pp. 1503, 2004.

[19] G. M. Walker and D. J. Beebe, "An evaporation-based microfluidic sample concentration method," *Lab on a Chip*, vol. 2, pp. 57-61, 2002.

[20] N. Goedecke, J. Eijkel, and A. Manz, "Evaporation driven pumping for chromatography application," *Lab on a Chip*, vol. 2, pp. 219-223, 2002.

[21] R. O. Slatyer, "Movement of water in the vascular system," in *Plant-Water Relationships*. New York: Academic Press, 1967, pp. 211-215.

[22] J. Sutcliffe, "Mechanisms of water movement," in *Plants and Water*, vol. 14, The Institute of Biology's Studies in Biology. London: Edward Arnold (Publishers) Ltd, 1968, pp. 72-76.

[23] D. H. Trevena, *Cavitation and Tension in Liquids*. Philadelphia: Adam Hilger, 1987.

[24] M. T. Tyree and M. H. Zimmerman, *Xylem Structure and the Ascent of Sap*. New York: Springer, 2002.

[25] D. H. Gracias, V. Kavthekar, J. C. Love, K. E. Paul, and G. M. Whitesides, "Fabrication of micrometer-scale, patterned polyhedra by self-assembly," *Advanced Materials*, vol. 14, pp. 235, 2002.

[26] P. W. Green, R. R. A. Syms, and E. M. Yeatman, "Demonstration of three-dimensional microstructure self-assembly," *Journal of Microelectromechanical Systems*, vol. 4, pp. 170, 1995.

[27] R. R. A. Syms, E. M. Yeatman, V. M. Bright, and G. M. Whitesides, "Surface tension-powered self-assembly of microstructures - The state-of-the-art," *Journal of Microelectromechanical Systems*, vol. 12, pp. 387, 2003.

[28] K. F. Bohringer, U. Srinivasan, and R. T. Howe, "Modeling of capillary forces and binding sites for fluidic self-assembly," *Technical Digest of the 14th IEEE International Conference on Micro Electro Mechanical Systems, MEMS 2001*, Interlaken, Switzerland, 2001.

[29] C. J. Morris, S. A. Stauth, and B. A. Parviz, "Self-assembly for microscale and nanoscale packaging: steps toward self-packaging," *IEEE Transactions on Components, Packaging and Manufacturing Technology, Part B: Advanced Packaging*, vol. 28, pp. 600, 2005.

[30] U. Srinivasan, D. Liepmann, and R. T. Howe, "Microstructure to substrate self-assembly using capillary forces," *Journal of Microelectromechanical Systems*, vol. 10, pp. 17, 2001.

[31] X. Xiaorong, L. Sheng-Hsiung, and K. F. Bohringer, "Geometric binding site design for surface-tension driven self-assembly," *Proceedings of the IEEE International Conference on Robotics and Automation*, New Orleans, LA, USA, 2004.

[32] C.-J. Kim, "The use of surface tension for the design of MEMS actuators," in Nanotribology: critical assessment and research needs, S. M. H. a. Z. C. Ying, Ed. Boston: Kluwer, 2003.

[33] B. C. Regan, S. Aloni, K. Jensen, and A. Zettl, "Surface-tension-driven nanoelectromechanical relaxation oscillator," *Applied Physics Letters*, vol. 86, pp. 119-123, 2005.

[34] M. Boncheva and G. M. Whitesides, "Templated self-assembly: Formation of folded structures by relaxation of pre-stressed, planar tapes," *Advanced Materials*, vol. 17, pp. 553, 2005.

[35] D. H. Gracias, J. Tien, T. L. Breen, C. Hsu, and G. M. Whitesides, "Forming electrical networks in three dimensions by self-assembly," *Science*, vol. 289, pp. 1170, 2000

[36] M. P. Stoykovich, H. B. Cao, K. Yoshimoto, L. E. Ocola, and P. F. Nealey, "Deformation of nanoscopic polymer structures in response to well-defined capillary forces," *Advanced Materials*, vol. 15, pp. 1180, 2003.

[37] http://www.gpmatthews.nildram.co.uk/microplants/fernspores001.jpg. [Accessed October 30, 2007].

[38] http://www.biology.iastate.edu/Courses/201L/Pteroph/FernIndx. [Accessed March 29, 2004].

[39] A. Ursprung, "Über die Kohäsion des Wasser in Farnannulus," *Berichte der Deutsch Botanischen Gesellschaft*, vol. 33, pp. 152-62, 1915.

[40] V. Raghavan, Developmental biology of fern gametophytes. New York: Cambridge University Press, 1989.

[41] K. Haider, "Zur Morpholegie und Physciologie der Sporangien leptosporangiater Farne," *Planta*, vol. 44, pp. 370-411, 1954.

[42] E. Steudle, "Acquisition of water by plant roots," *Annual Review of Plant Physiology: Plant Molecular Biology*, vol. 52, 2001.

[43] E. Chanliaud, K. Burrows, G. Jeronimidis, and M. Gidley, "Mechanical properties of primary plant cell wall analogues," *Planta*, vol. 215, pp. 989, 2002.

[44] S. D. Senturia, *Microsystem Design*. Boston: Kluwer, 2000, pp. 240-244.

[45] J. W. Weaver, S. P. Timoshenko, and D. H. Young, *Vibration Problems in Engineering*, 5th ed. New York: Wiley, 1990, pp. 518-520.

[46] D. L. Bower, *An Introduction to Polymer Physics*. New York: Cambridge University Press, 2002, pp. 164-176.

[47] C. E. Maneschy, M. Massoudi, and V. R. Velloso, "Dynamic elastic solutions in neo-Hookean and Mooney-Rivlin materials," *International Journal of Non-Linear Mechanics*, vol. 28, pp. 531, 1993.

[48] D. L. Bower, "Elastic properties of isotropic polymers at small strains," in *An Introduction to Polymer Physics*. New York: Cambridge University Press, 2002, pp. 164-176.

[49] J. M. Gere, "Bending stresses in beams," in *The Engineering Handbook*, R. C. Dorf, Ed. Boca Raton, FL: CRC Press, Inc., 1996, pp. 52-59.

[50] S. Goyal, N. C. Perkins, and C. L. Lee, "Nonlinear dynamics and loop formation in Kirchoff rods with implications to the mechanics of DNA and cables," *Journal of Computational Physics*, vol. 209, pp. 371-389, 2005.

[51] D. Armani, C. Liu, and N. Aluru, "Re-configurable fluid circuits by PDMS elastomer micromachining," *Technical Digest of the Twelfth IEEE International Conference on Micro Electro Mechanical Systems, MEMS '99*, Orlando, FL, USA, 1999.

[52] F. Carillo, S. Gupta, M. Balooch, S. J. Marshall, G. W. Marshall, L. Pruitt, and C. M. Puttlitz, "Nanoindentation of polydimethylsiloxane elastomers: Effect of crosslinking, work of adhesion, and fluid environment on elastic modulus," *Journal of Materials Research*, vol. 20, pp. 2820, 2005.

[53] H. Ishihara, F. Arai, T. Fukuda, "Micro mechantronics and micro actuators," *IEEE Transactions on Mechatronics*, vol. 1, no. 1, pp. 68-79, 1996.

[54] R. Maboudian and R. T. Howe, "Critical review: adhesion in surface micromechanical structures," *Journal of Vacuum Science & Technology B: Microelectronics Processing and Phenomena*, vol. 15, pp. 1, 1997.

[55] Y. H. C. Ishiyama, "Effects of humidity on Young's modulus in poly(methyl methacrylate)," *Journal of Polymer Science Part B: Polymer Physics*, vol. 40, pp. 460-465, 2002.

[56] S. Roundy, E. S. Leland, J. Baker, E. Carleton, E. Reilly, E. Lai, B. Otis, J. M. Rabaey, P. K. Wright, and V. Sundararajan, "Improving power output for vibration-based energy scavengers," *IEEE Pervasive Computing*, vol. 4, pp. 28, 2005.

[57] L. Mateu and F. Moll, "Review of energy harvesting techniques and applications for microelectronics," *Proceedings of the SPIE Microtechnologies for the New Millenium*, Sevilla, Spain, pp. 359-373, 2005.

[58] R. Tashiro, N. Kabei, K. Katayama, E. Tsuboi, and K. Tsuchiya, "Development of an electrostatic generator for a cardiac pacemaker that harnesses the ventricular wall motion," *Journal of Artificial Organs*, vol. V5, pp. 239, 2002.

[59] S. Roundy, P. Wright, and K. Pister, "Micro-electrostatic vibration-to-electricity converters," *American Society of Mechanical Engineers International Mechanical Engineering Congress and Exposition*, New Orleans, 2002.

[60] R. T. Borno, J. D. Steinmeyer, and M. M. Maharbiz, "Energy scavenging from transpiration," *Proceedings of the Eleventh International Conference on Miniaturized Systems for Chemistry and Life Sciences (MicroTAS)*, Paris, France, pp. 566-568, 2007.

[61] R. Duggirala, H. Li, A. M. Pappu, Z. Fu, A. Aspel, and A. Lal, "Radioisotope micropower generator for CMOS self-powered sensor microsystems," *Proceedings of the 4th International Workshop on Micro and Nantechnology for Power Generation and Energy Conversion Applications PowerMEMS 2004*, Kyoto, Japan, 2004.

[62] S. Roundy, P. K. Wright, and J. Rabaey, "A study of low level vibrations as a power source for wireless sensor nodes," *Computer Communications*, vol. 26, pp. 1131, 2003.

[63] H. A. Sodano, G. Park, and D. J. Inman, "Estimation of Electric Charge Output for Piezoelectric Energy Harvesting," *Strain*, vol. 40, pp. 49, 2004.

[64] J. Kymissis, C. Kendall, J. Paradiso, and N. Gershenfeld, “Parasitic power harvesting in shoes,” *Digest of Papers of the Second International Symposium on Wearable Computers*, 1998.

[65] N. S. Shenck and J. A. Paradiso, “Energy scavenging with shoe-mounted piezoelectrics,” *IEEE Micro*, vol. 21, pp. 30, 2001.

[66] C. B. Williams, C. Shearwood, M. A. Harradine, P. H. Mellor, T. S. Birch, and R. B. Yates, “Development of an electromagnetic micro-generator,” *IEE Proceedings - Circuits, Devices and Systems*, vol. 148, pp. 337, 2001.

[67] H. Kulah and K. Najafi, “An electromagnetic micro power generator for low-frequency environmental vibrations,” *Technical Digest of the 17th IEEE International Conference on Micro Electro Mechanical Systems, MEMS 2004,* Maastricht, NL, 2004.

[68] www.perpetuum.co.uk.

[69] G. Despesse, T. Jager, J. Chaillout, J. Leger, A. Vassilev, S. Basrour, and B. Chalot, “Fabrication and characterisation of high damping electrostatic micro devices for vibration energy scavenging,” *Proceedings of the Design, Test, Integration and Packaging of MEMS and MOEMS*, Montreux, Switzerland, 2005.

[70] P. Mitcheson, B. Stark, P. Miao, E. Yeatman, A. Holmes, and T. Green, “Analysis and optimisation of MEMS on-chip power supply for self powering of slow moving sensors,” *Eurosensors XVII*, Guimaraes, Portugal, 2003.

[71] M. Mizuno and D. G. Chetwynd, “Investigation of a resonance microgenerator,” *Journal of Micromechanics and Microengineering*, vol. 13, pp. 209, 2003.

[72] S. Scherrer, D. G. Plumlee, and A. J. Moll, “Energy scavenging device in LTCC materials,” *IEEE Workshop on Microelectronics and Electron Devices, WMED '05*, Boise, Idaho, 2005.

[73] A. Bayrashev, W. P. Robbins, and B. Ziaie, “Low frequency wireless powering of microsystems using piezoelectric-magnetostrictive laminate composites,” *Sensors and Actuators A: Physical*, vol. 114, pp. 244, 2004.

[74] N. N. H. Ching, H. Y. Wong, W. J. L. P. H. W. Leong, and Z. Wen, “A laser-micromachined vibrational to electrical power transducer for wireless sensing systems,” *Sensors and Actuators A*, vol. 97-98, pp. 685-690, 2002.

[75] B. S. Marzencki M, Charlot B, Grasso A, Colin M and Valbin L, “Design and fabrication of piezoelectric micro power generators for autonomous microsystems,” *Proceedings of the Design, Test, Integration and Packaging of MEMS and MOEMS*, Montreux, Switzerland, 2005.

[76] A Perez-Rodriguez, C. Serre, N. Fondevilla, C. Cereceda, J. R. Morante, J. Esteve, and J. Montserrat, “Design of electromagnetic inertial generators for energy scavenging applications,” *Eurosensors XIX*, Barcelona, Spain, 2005.

[77] P. Glynne-Jones, S. P. Beeby, and N. M. White, “Towards a piezoelectric vibration-powered microgenerator,” *IEE Proceedings - Science, Measurement and Technology*, vol. 148, pp. 68, 2001.

[78] Y. B. Jeon, R. Sood, J. h. Jeong, and S. G. Kim, “MEMS power generator with transverse mode thin film PZT,” *Sensors and Actuators A: Physical*, vol. 122, pp. 16, 2005.

[79] P. Glynne-Jones, M. J. Tudor, S. P. Beeby, and N. M. White, “An electromagnetic, vibration-powered generator for intelligent sensor systems,” *Sensors and Actuators A: Physical*, vol. 110, pp. 344, 2004.

[80] H. W. Kim, A. Batra, S. Priya, K. Uchino, D. Markley, R. E. Newnham, and H. F. Hofmann, “Energy Harvesting Using a Piezoelectric “Cymbal” Transducer in Dynamic Environment,” *Japanese Journal of Applied Physics*, vol. 43, pp. 6178-6183, 2004.

[81] M. El-hami, P. Glynne-Jones, N. M. White, M. Hill, S. Beeby, E. James, A. D. Brown, and J. N. Ross, “Design and fabrication of a new vibration-based electromechanical power generator,” *Sensors and Actuators A: Physical*, vol. 92, pp. 335, 2001.

[82] W. J. Li, Z. Wen, P. K. Wong, G. M. H. Chan, and P. H. W. Leong, “A micromachined vibration-induced power generator for low power sensors of robotic systems,” presented at World Automation Congress: 8th Int. Symp. on Robotics with Applications, Hawaii, 2000.

[83] J. Boland, C. Yuan-Heng, Y. Suzuki, and Y. C. Tai, “Micro electret power generator,” *Technical Digest of the 16th IEEE International Conference on Micro Electro Mechanical Systems, MEMS 2003,* Kyoto, 2003.

[84] Y. Arakawa, Y. Suzuki, and N. Kasagi, “Micro seismic power generator using electret polymer film,” presented at Power MEMS Conference, Kyoto, Japan, 2004.

[85] T. Sterken, P. Fiorini, K. Baert, G. Borghs, and R. Puers, “Novel design and fabrication of a MEMS electrostatic vibration scavenger,” presented at Power MEMS Conference, Kyoto, Japan, 2004.

[86] J. S. Sperry, “Evolution of water transport and xylem structure,” International Journal of Plant Science, vol. 163, pp. S115-S127, 2003.

[87] M. J. Canny, “The transpiration stream in the leaf apoplast: water and solutes,” Philosophical Transactions: Biological Sciences, vol. 341, pp. 87-100, 1993.

[88] K. A. McCulloh, J. S. Sperry, and F. R. Adler, “Water transport in plants obeys Murray's Law,” Nature, vol. 27, pp. 939-942, 2003.

[89] A. N. Chatterjee and N. R. Aluru, “Combined Circuit/Device Modeling and Simulation of Integrated Microfluidic Systems,” Journal of Microelectromechanical Systems, vol. 14, no. 1, Feb. 2005, pp. 81-95.

[90] T. F. Sherman, “On Connecting Large Vessels to Small: The Meaning of Murray's Law,” The Journal of General Physiology, vol. 78, pp. 431-453, 1981.

[91] J. S. Sperry, U. G. Hacke, R. Oren, and J. P. Comstock, “Water deficits and hydraulic limits to leaf water supply,” Plant, Cell & Environment, vol. 25, pp. 251-263, 2002.

[92] P. Gravesen, J. Branebjerg, and O. S. Jensen, “Microfluidics-a review,” Journal of Micromechanics and Microengineering, vol. 3, pp. 168, 1993.

[93] S. Meninger, J. Mur-Miranda, J. Lang, A. Chandrakasan, A. Slocum, M. Schmidt, and R. Amirtharajah, “Vibration to electric energy conversion,” *IEEE Transactions Very Large Scale Integration (VLSI) Systems*, vol. 9, pp. 64-76, 2001.

[94] K. Yasuoka, M. Matsumoto, and Y. Kataoka, “Evaporation and condensation at a liquid surface. I. Argon,” Journal of Chemical Physics. vol. 101, no. 9, pp. 7904 - 7911, 1994.

[95] C. A. Ward and G. Fang, “Expression for predicting liquid evaporation flux: Statistical rate theory approach,” Physical Review E, vol. 59, no. 1, pp. 429-440, 1999.

[96] K. Hisatake, M. Fukuda, J. Kimura, M. Maeda, and Y. Fukuda, “Experimental and theoretical study of evaporation of water in a vessel,” Journal of Applied Physics, vol. 77, no. 12, pp. 6664 - 6674, 1995.

[97] J. C. T. Eijkel and A. v. d. Berg, “Water in micro- and nanofluidics systems described using the water potential,” *Lab on a Chip*, vol. 5, pp. 1202-1209, 2005.

[98] S. Mutlu, “Microfluidic Biochemical Analysis System With Electro-Osmotic Pump and Thermally Responsive Polymer Valve,” Ph.D. Dissertation, University of Michigan-Ann Arbor, 2004.

[99] A. Host-Madsen and J. Zhang, “Capacity bounds and power allocation for wireless relay channels,” *IEEE Transactions on Information Theory*, vol. 51, pp. 2020-2040, 2005.

[100] X. Cheng, B. Narahari, R. Simha, M. X. Cheng, D. Liu, “Strong Minimum Energy Topology in Wireless Sensor Networks: NP-Completeness and Heuristics,” *IEEE Transactions on Mobile Computing*, vol. 2, no. 3, pp. 248-256, 2003.